



## **Extinction theorem analysis of diffraction anomalies in overcoated-gratings.**

Item Type	text; Dissertation-Reproduction (electronic)
Authors	DeSandre, Lewis Francis.
Publisher	The University of Arizona.
Rights	Copyright © is held by the author. Digital access to this material is made possible by the University Libraries, University of Arizona. Further transmission, reproduction or presentation (such as public display or performance) of protected items is prohibited except with permission of the author.
Download date	04/08/2022 18:31:16
Link to Item	<a href="http://hdl.handle.net/10150/184853">http://hdl.handle.net/10150/184853</a>

## INFORMATION TO USERS

The most advanced technology has been used to photograph and reproduce this manuscript from the microfilm master. UMI films the text directly from the original or copy submitted. Thus, some thesis and dissertation copies are in typewriter face, while others may be from any type of computer printer.

The quality of this reproduction is dependent upon the quality of the copy submitted. Broken or indistinct print, colored or poor quality illustrations and photographs, print bleedthrough, substandard margins, and improper alignment can adversely affect reproduction.

In the unlikely event that the author did not send UMI a complete manuscript and there are missing pages, these will be noted. Also, if unauthorized copyright material had to be removed, a note will indicate the deletion.

Oversize materials (e.g., maps, drawings, charts) are reproduced by sectioning the original, beginning at the upper left-hand corner and continuing from left to right in equal sections with small overlaps. Each original is also photographed in one exposure and is included in reduced form at the back of the book. These are also available as one exposure on a standard 35mm slide or as a 17" x 23" black and white photographic print for an additional charge.

Photographs included in the original manuscript have been reproduced xerographically in this copy. Higher quality 6" x 9" black and white photographic prints are available for any photographs or illustrations appearing in this copy for an additional charge. Contact UMI directly to order.

# U·M·I

University Microfilms International  
A Bell & Howell Information Company  
300 North Zeeb Road, Ann Arbor, MI 48106-1346 USA  
313/761-4700 800/521-0600



**Order Number 9010474**

**Extinction theorem analysis of diffraction anomalies in  
overcoated gratings**

**DeSandre, Lewis Francis, Ph.D.**

**The University of Arizona, 1989**

**Copyright ©1989 by DeSandre, Lewis Francis. All rights reserved.**

**U·M·I**  
300 N. Zeeb Rd.  
Ann Arbor, MI 48106



**EXTINCTION THEOREM ANALYSIS OF DIFFRACTION  
ANOMALIES IN OVERCOATED GRATINGS**

**b y**

**Lewis Francis DeSandre**

---

**Copyright © Lewis Francis DeSandre 1989**

**A Dissertation Submitted to the Faculty of the  
COMMITTEE ON OPTICAL SCIENCES (GRADUATE)**

**In Partial Fulfillment of the Requirements  
For the Degree of**

**DOCTOR OF PHILOSOPHY**

**In the Graduate College**

**THE UNIVERSITY OF ARIZONA**

**1989**

THE UNIVERSITY OF ARIZONA  
GRADUATE COLLEGE

As members of the Final Examination Committee, we certify that we have read  
the dissertation prepared by Lewis Francis DeSandre

entitled Extinction Theorem Analysis of Diffraction Anomalies in  
Overcoated Gratings

and recommend that it be accepted as fulfilling the dissertation requirement  
for the Degree of Doctor of Philosophy.

J. Mark Egan

3 MAY 89  
Date

H. A. Mairson

3 May 1989  
Date

G. J. Burke

3 May 1989  
Date

Date

Date

Final approval and acceptance of this dissertation is contingent upon the  
candidate's submission of the final copy of the dissertation to the Graduate  
College.

I hereby certify that I have read this dissertation prepared under my  
direction and recommend that it be accepted as fulfilling the dissertation  
requirement.

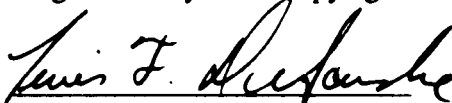
J. Mark Egan H. A. Mairson  
Dissertation Director

3 May 1989  
Date

## STATEMENT BY AUTHOR

This dissertation has been submitted in partial fulfillment of requirements for an advanced degree at The University of Arizona and is deposited in the University Library to be made available to borrowers under rules of the Library.

Brief quotations from this dissertation are allowable without special permission, provided that accurate acknowledgment of source is made. Requests for permission for extended quotation from or reproduction of this manuscript in whole or in part may be granted by the copyright holder.

SIGNED:   
Lewis Francis DeSandre



#### ACKNOWLEDGMENTS

First and foremost, I would like to express gratitude to my dissertation advisor, Dr. J. M. Elson, for many long hours of discussion and assistance.

I extend my special thanks to Professor H. Angus Macleod for his advice and confidence while working on this dissertation.

I am especially indebted to Dr. J. L. Stanford and the Naval Weapons Center for their continual support and encouragement. Also, I am extremely grateful to Mr. J. R. Albertine, Naval Warfare Systems Command, PMW-145, for his support and interest in this research effort.

Finally, I would like to thank Sharon Chesnut and Beverly Reymore for their superior typing and editorial assistance.

**DEDICATION**

**To my daughter, Heather Lynn.**

## TABLE OF CONTENTS

List of Illustrations . . . . .	8
List of Tables . . . . .	12
Abstract . . . . .	13
Chapter 1. Dissertation Outline . . . . .	15
Chapter 2. Historical Survey of Anomalous Effects From	
Uncoated and Coated Diffraction Gratings . . . . .	19
Introduction . . . . .	19
Uncoated Metallic Gratings . . . . .	21
Wood's Anomalies and Rayleigh's Theory . . . . .	21
Failure of the Rayleigh Theory . . . . .	23
Rigorous Theory of Grating Diffraction . . . . .	27
Plasmon Excitation . . . . .	29
Overcoated Gratings . . . . .	32
Chapter Summary . . . . .	36
Chapter 3. Graphical Method for the Determination of Waveguide	
Mode in Multilayer-Overcoated Diffraction Gratings . . . . .	39
Introduction . . . . .	39
Characteristic Matrix Approach . . . . .	43
Waveguide Modes . . . . .	47
Bound Modes . . . . .	51
Lossy Waves . . . . .	52
Guided-Wave Calculations . . . . .	53
Conclusions . . . . .	54
Chapter 4. Extinction Theorem: Single Surface . . . . .	56
Field Equations . . . . .	56
Boundary Conditions . . . . .	60
Reflection Coefficient Matrix . . . . .	72
TE Polarization . . . . .	74
Chapter 5. Extinction Theorem Analysis for Multilayer Structures . . . . .	75
Introduction . . . . .	75
Extinction Theorem: $j$ th Layer . . . . .	78
Characteristic Matrix Propagation . . . . .	81
Extinction Theorem: Substrate Initialization . . . . .	83
Extinction Theorem: Incident Medium . . . . .	83
Extinction Theorem: R-Matrix Propagation . . . . .	84
Conclusions . . . . .	87

## TABLE OF CONTENTS (CONTD)

<b>Chapter 6. Numerical Results</b> .....	<b>90</b>
<b>Introduction</b> .....	<b>90</b>
<b>Single-Dielectric Layer Upon a Dielectric Substrate:</b>	
<b>TE Polarization</b> .....	<b>93</b>
<b>Single-Dielectric Layer Upon a Metallic Substrate:</b>	
<b>TE Polarization</b> .....	<b>97</b>
<b>Multilayer Dielectric Upon a Metal Substrate: TE Polarization</b> .....	<b>98</b>
<b>Multilayer Dielectric Upon a Metal Substrate: TM Polarization</b> .....	<b>100</b>
 <b>Chapter 7. Experimental Verification</b> .....	 <b>101</b>
 <b>Chapter 8. Conclusion</b> .....	 <b>103</b>
<b>Summary</b> .....	<b>103</b>
<b>Suggestions For Future Work</b> .....	<b>106</b>
 <b>Appendices</b>	
<b>A. Derivation of the Extinction Theorem From Green's Identity</b> .....	<b>109</b>
<b>B. Calculation of Matrix Elements for Arbitrary Groove Profile.</b> .....	<b>117</b>
<b>C. Calculation of Matrix Elements for Sinusoidal Groove Profile.</b> .....	<b>120</b>
<b>D. Extinction Theorem Computer Program</b> .....	<b>122</b>
 <b>References</b> .....	 <b>167</b>

## LIST OF ILLUSTRATIONS

1. Schematic of a Single-Layer Coated Grating With Identical Trapezoidal Profiles at Each Interface . . . . .	140
2. Illustration of the Phase Condition $\phi_1 + \phi_2 + 2\delta = 2\pi m$ for a Single-Layer Planar Waveguide Where the Phase Thickness $\delta = 2\pi/\lambda_0 n_h \cos \theta_{gw}$ . . . . .	140
3. Schematic of a Multilayer Assembly Divided at the Surface Boundary and Showing Phase $\phi$ and Admittance $Y$ of the Ingoing and Outgoing Waves . . . . .	141
4. Schematic of a Grating Surface of Period $D$ and With Profile Function $f(x)$ . . . . .	141
5. Schematic Representation of a Multilayer-Coated Sinusoidal Grating . . . . .	142
6(a). Diffraction Efficiency of the Zeroth Reflected Order of the Sinusoidal Grating, as Shown in Figure 2(b) in Reference 64 . .	143
6(b). Comparison of Extinction Method Calculation Used in This Paper for a Dielectric Waveguide Shown in Figure 6(a) . . . . .	144
7(a). The Trapezoidal Profile Used in the Numerical Analysis . . . . .	145
7(b). Rounded Trapezoidal Profile Used in the Numerical Analysis . . . . .	145
8(a). Phase Plot . . . with wave vector $\omega/c n_1 \sin \theta_{gw}$ : single-dielectric layer ( $\epsilon_1 = 5.11, 0.0$ ), thickness $0.25 \mu m$ , upon a dielectric substrate ( $\epsilon_S = 2.25, 0.0$ ) . . . . .	146
8(b). Phase Plot . . . with wave vector $\omega/c n_1 \sin \theta_{gw}$ : single-dielectric layer ( $\epsilon_1 = 5.11, 0.0$ ), thickness $0.30 \mu m$ , upon a metallic substrate ( $\epsilon_S = 16.4, 0.52$ ) . . . . .	147
8(c). Phase Plot . . . with wave vector $\omega/c n_1 \sin \theta_{gw}$ : multilayer-dielectric of design HL ( $\epsilon_H = 5.11, 0.0$ ; $\epsilon_L = 2.25, 0.0$ ), quarter-wave optical thickness at $45^\circ$ angle of incidence, metallic substrate ( $\epsilon_S = -16.4, 0.52$ ) . . . . .	148
8(d). Phase Plot . . . with wave vector $\omega/c n_1 \sin \theta_{gw}$ : multilayer-dielectric of design $(HL)^2$ ( $\epsilon_H = 5.11, 0.0$ ; $\epsilon_L = 2.25, 0.0$ ), quarter-wave optical thickness at $45^\circ$ angle of incidence, metallic substrate ( $\epsilon_S = -16.4, 0.52$ ) . . . . .	149
8(e). Phase Plot . . . with wave vector $\omega/c n_1 \sin \theta_{gw}$ : multilayer-dielectric of design $(HL)^4$ ( $\epsilon_H = 5.11, 0.0$ ; $\epsilon_L = 2.25, 0.0$ ), quarter-wave optical thickness at $45^\circ$ angle of incidence, metallic substrate ( $\epsilon_S = -16.4, 0.52$ ) . . . . .	150
8(f). Phase Plot . . . with wave vector $\omega/c n_1 \sin \theta_{gw}$ : multilayer-dielectric of design HL ( $\epsilon_H = 5.11, 0.0$ ; $\epsilon_L = 2.25, 0.0$ ), quarter-wave optical thickness at $45^\circ$ angle of incidence, metallic substrate ( $\epsilon_S = -16.4, 0.52$ ) . . . . .	151

## LIST OF ILLUSTRATIONS (CONTD)

9. Intensity Versus Angle of Incidence for (a) 0 and (b) -1 Order Reflected Beams and (c) +1 Order Coupling to the $j = 0$ Guided-Wave Mode (H/L: Trapezoid; $h = 0.01 \mu\text{m}$ ; s-Polarized) . . . . .	152
10. Intensity Versus Angle of Incidence for (a) 0 and (b) -1 Order Reflected Beams and (c) +1 Order Coupling to the $j = 0$ Guided-Wave Mode (H/L: Replicated Trapezoid; $h = 0.1 \mu\text{m}$ ; s-Polarized) . . . . .	152
11. Intensity Versus Angle of Incidence for (a) 0 and (b) -1 Order Reflected Beams and (c) +1 Order Coupling to the $j = 0$ Guided-Wave Mode (H/L: Replicated Trapezoid; $h = 0.001 \mu\text{m}$ ; s-Polarized) . . . . .	153
12. Intensity Versus Angle of Incidence for (a) and (b) -1 Order Reflected Beams and (c) +1 Order Coupling to the $j = 0$ Guided-Wave Mode (H/L: Rectangle; $h = 0.01 \mu\text{m}$ ; 40% Duty Cycle; s-Polarized) . . . . .	153
13. Intensity Versus Angle of Incidence for (a) 0 and (b) -1 Order Reflected Beams and (c) +1 Order Coupling to the $j = 0$ Guided-Wave Mode (H/L: Rectangle; $h = 0.01 \mu\text{m}$ ; 50% Duty Cycle; s-Polarized) . . . . .	154
14. Intensity Versus Angle of Incidence for (a) 0 and (b) -1 Order Reflected Beams and (c) +1 Order Coupling to the $j = 0$ Guided-Wave Mode (H/L: Rectangle; $h = 0.01 \mu\text{m}$ ; 80% Duty Cycle; s-Polarized) . . . . .	155
15. Intensity Versus Angle of Incidence for (a) 0 and (b) -1 Order Reflected Beams and (c) +1 Order Coupling to the $j = 0$ Guided-Wave Mode (H/L: Rectangle; $h = 0.01 \mu\text{m}$ ; 90% Duty Cycle; s-Polarized) . . . . .	156
16. Intensity Versus Angle of Incidence for (a) 0 and (b) -1 Order Reflected Beams and (c) +1 Order Coupling to the $j = 0$ Guided-Wave Mode (H/L: Triangle; $h = 0.01 \mu\text{m}$ ; s-Polarized) . . . . .	156
17. Intensity Versus Angle of Incidence for (a) 0 and (b) -1 Order Reflected Beams and (c) +1 Order Coupling to the $j = 0$ Guided-Wave Mode (H/L: Replicating Sinusoidal; $h = 0.01 \mu\text{m}$ ; s-Polarized) . . . . .	157
18. Intensity Versus Angle of Incidence for (a) 0 and (b) -1 Order Reflected Beams and (c) +1 Order Coupling to the $j = 0$ Guided-Wave Mode (H/L: Nonreplicating Trapezoid; $h = 0$ , $h = 0.01 \mu\text{m}$ ; s-Polarized) . . . . .	157
19. Intensity Versus Angle of Incidence for (a) 0 and (b) -1 Order Reflected Beams and (c) +1 Order Coupling to the $j = 0$ Guided-Wave Mode (H/L: Nonreplicating Trapezoid; $h = 0.01$ , $h = 0 \mu\text{m}$ ; s-Polarized) . . . . .	158

## LIST OF ILLUSTRATIONS (CONTD)

20. Intensity Versus Angle of Incidence for (a) 0 and (b) -1 Order Reflected Beams and (c) +1 Order Coupling to the $j = 0$ Guided-Wave Mode (HL/Ag: Replicating Trapezoid; $h = 0.01 \mu\text{m}$ ; s-Polarized) . . . . .	158
21. Intensity Versus Angle of Incidence for (a) 0 and (b) -1 Order Reflected Beams and (c) +1 Order Coupling to the $j = 0$ Guided-Wave Mode (H/Ag: Nonreplicating Trapezoid; $h = 0, h = 0.01$ ; s-Polarized) . . . . .	159
22. Intensity Versus Angle of Incidence for (a) 0 and (b) -1 Order Reflected Beams and (c) +1 Order Coupling to the $j = 0$ Guided-Wave Mode (H/Ag: Nonreplicating Trapezoid; $h = 0.01, h = 0 \mu\text{m}$ ; s-Polarized) . . . . .	159
23. Intensity Versus Angle of Incidence for (a) 0 and (b) -1 Order Reflected Beams and (c) +1 Order Coupling to the $j = 0$ Guided-Wave Mode (HL/Ag: Replicating Trapezoid; $h = 0.01 \mu\text{m}$ ; s-Polarized) . . . . .	160
24. Intensity Versus Angle of Incidence for (a) 0 and (b) -1 Order Reflected Beams and (c) +1 Order Coupling to the $j = 0$ Guided-Wave Mode $[(HL)^2/Ag$ : Replicating Trapezoid; $h = 0.01 \mu\text{m}$ ; s-Polarized] . . . . .	160
25. Intensity Versus Angle of Incidence for (a) 0 and (b) -1 Order Reflected Beams and (c) +1 Order Coupling to the $j = 0$ Guided-Wave Mode $[(HL)^4/Ag$ : Replicating Trapezoid; $h = 0.01 \mu\text{m}$ ; s-Polarized] . . . . .	161
26. Intensity Versus Angle of Incidence for (a) 0 and (b) -1 Order Reflected Beams and (c) +1 Order Coupling to the $j = 0$ Guided-Wave Mode $[(HL)^4/Ag$ : Trapezoid on Surface; $h = 0.001 \mu\text{m}$ ; s-Polarized] . . . . .	162
27. Intensity Versus Angle of Incidence for (a) 0 and (b) -1 Order Reflected Beams and (c) +1 Order Coupling to the $j = 0$ Guided-Wave Mode $[(HL)^4/Ag$ : Trapezoid on Substrate; $h = 0.01 \mu\text{m}$ ; s-Polarized] . . . . .	162
28. Intensity Versus Angle of Incidence for (a) 0 and (b) -1 Order Reflected Beams and (c) +1 Order Coupling to the $j = 0$ Guided-Wave Mode $[(HL)^4/Ag$ : Rounded Trapezoid; $h = 0.01 \mu\text{m}$ ; s-Polarized] . . . . .	163
29. Intensity Versus Angle of Incidence for (a) 0 and (b) -1 Order Reflected Beams and (c) +1 Order Coupling to the $j = 0$ Guided-Wave Mode $[HL^4/Ag$ : Rounded Trapezoid; $h = 0.01, 0.009, 0.008, 0.007, 0.006, 0.005, 0.004, 0.003, 0.002 \mu\text{m}$ ; s-Polarized] . . . . .	163
30. Intensity Versus Angle of Incidence for (a) 0 and (b) -1 Order Reflected Beams and (c) +1 Order Coupling to the $j = 0$ Guided-Wave Mode $[(HL)^2/Ag$ : Replicated Trapezoid; $h = 0.01 \mu\text{m}$ ; p-Polarized] . . . . .	164

## LIST OF ILLUSTRATIONS (CONTD)

31. Intensity Versus Angle of Incidence for (a) 0 and (b) -1 Order Reflected Beams and (c) +1 Order Coupling to the $j = 0$ Guided-Wave Mode $[(HL)^2/Ag$ : Rounded Trapezoid; $h = 0.006, 0.007, 0.008, 0.009, 0.01 \mu\text{m}$ ; p-Polarized] . . . . .	164
32. Efficiency Calculations in the 0, -1, and +1 Diffracted Order for a Single-Layer Coated Grating . . . . .	165
33. Experimental Arrangement Used for Making Coupling Efficiency Measurements . . . . .	166
34. Contour of Integration $C = P_1 + P_2 + P_3 + P_3$ Enclosing Volumn V Used to Evaluate Surface Integral Appearing in Green's Theorem Equation A-1 . . . . .	166
35. Geometry Considered for Calculation of Matrix Elements: Point-to-Point Integration Method . . . . .	167



## LIST OF TABLES

1. Normalized Guided-Wave Numbers $k_{gw}$ and Mode Coupling Angles $\theta_0$ ( $k_{gw} = n_1 \sin \theta$ ; $n_1 = 2.26$ ) . . . . .	93
2. Numerical and Experimental Results for the Sapphire-Coated Grating ( $\lambda = 3.8 \mu\text{m}$ , TM Polarization, $m = 1$ Coupling Into the 0th Guided-Wave Mode) . . . . .	102
3(a). Sample Input Files . . . . .	123
3(b). Sample Output Files . . . . .	125

### ABSTRACT

A rigorous analysis based upon the extinction theorem is presented to study anomalous resonance effects from single- and multilayer-overcoated, low-efficiency diffraction gratings. Anomalously high diffraction efficiency at resonance results from the coupling of the incident beam into guided waves that can be propagated within the composite structure. Both the traditional characteristic matrix technique and a recursive or R-matrix propagation technique are presented. The R-matrix propagation algorithm was found to be stable numerically, and computational results agree favorably with both experimental and other theoretical work. Numerical results are presented in order to investigate the influence of certain parameters (i.e., groove depth and shape and the number of high- and low-index overlayers) on the diffraction efficiency at resonance. In this analysis, a wavelength of  $0.6328\text{ }\mu\text{m}$  and grating period of  $0.7\text{ }\mu\text{m}$  were chosen so that only a -1 diffracted order other than the specular is reflected from the gratings. Perfect transfer of the grating relief to the film boundaries does not occur in all instances; it depends on the grating and film characteristics together with the conditions during deposition. Investigated in this work is the effect of nonreplication of the grating profile at film interfaces on anomalous diffraction; a transition from trapezoidal profile at the grating substrate to a rounded relief at the top surface of the multilayer structure is assumed. For the cases studied, it was found that nonreplication has the effect of reducing the strength of the resonance outcoupling.

Finally, experimental results on anomalous resonance effects for multilayer-coated gratings are presented. Good agreement with computational results was attained.

## Chapter 1

### DISSERTATION OUTLINE

In this dissertation, anomalous resonance effects in multilayer-overcoated diffraction gratings are studied theoretically, numerically, and experimentally. The term "grating anomaly" is used to describe observed abrupt variations of intensity in the diffracted order with a change in either the wavelength or angle of incidence. In this work, grating anomaly is to be distinguished from anomalous behavior associated with ruling imperfections known as Rowland or Lyman ghost lines.

Much has been written on anomalous behavior of uncoated and coated diffraction gratings. Phenomena associated with Rayleigh anomalies and surface plasmon excitation are extensively reported in the literature. Guided-wave excitation and anomalous diffraction efficiencies for multilayer-overcoated gratings, however, have received less attention. Much of the work in this area has concentrated on high-efficiency gratings with sinusoidal profiles; consequently, a degradation of diffraction efficiency was reported. Although the extinction theorem technique is exact in that small groove-depth-to-wavelength ratio is not assumed, the purpose of this work is to concentrate on diffraction anomalies from low-efficiency gratings, where the groove-depth-to-wavelength ratio is a few percent. In order to place the results of this dissertation in context, an historical review

that summarizes the more relevant observations and explanations of grating anomalies is presented in Chapter 2.

Anomalous resonance effects in multilayer-overcoated gratings result from the coupling of the incident light into guided waves supported by the multilayer structure. In order to determine the incident angles for which resonance effects are expected, it is important to determine the allowed guided-wave modes. Presented in Chapter 3 is a simple graphical method that utilizes the characteristic matrix technique to determine waveguide modes in multilayer assemblies. This method is approximate, since the substrate and interfaces of the overlayers are assumed to be planar. The advantage of this technique is that an estimate of incident coupling angles can be found readily without recourse to a rigorous calculation.

The first theoretical approach to the problem of anomalous diffraction was that of Lord Rayleigh,<sup>1</sup> who assumed that the diffracted wave could everywhere be represented as a sum of outgoing plane waves. Subsequently, more rigorous theories have been formulated, limited at first to the study of diffraction from single surfaces. The effort to calculate diffraction efficiencies from high-power beamsplitter mirrors led to an integral equation formalism with the ability to predict the behavior of multilayered, highly modulated structures. The theoretical analysis developed in this dissertation is based on the extinction theorem, which is also an integral method, applied originally by Toigo *et al.*<sup>2</sup> to a single rough surface. Since this method avoids the Rayleigh plane-wave hypothesis, it provides an exact formulation of the boundary problem and description of the diffracted field. The extinction method has been used extensively in the analysis of

diffraction and plasmon excitation for a single-modulated interface. To the author's knowledge, it has not been used in the analysis of resonance effects in multilayer structures. Beginning with a mathematical description of the extinction method as it applies to a single grating surface (Chapter 4), this formalism is extended in Chapter 5 to the analysis of multilayer-coated gratings. The analysis accommodates any groove shape with grooves perpendicular to the plane of incidence. Both transverse electric (TE) and transverse magnetic (TM) polarizations are considered.

Numerical analysis of resonance effects in single- and multilayer-coated gratings is presented in Chapter 6. In the same chapter, the influence of groove shape and depth and the number of high- and low-index multilayers on diffraction efficiency are investigated.

An additional factor that may influence diffraction efficiency is the degree of replication of the grating profile at each interface of the multilayer coating. Previously, resonance effects were studied assuming perfect replication of the substrate grating profile at each film interface.<sup>3</sup> However, perfect transfer of the grating relief to the film boundaries does not occur in all instances; it depends on the grating and film characteristics together with the conditions during deposition. Also in Chapter 6, the effect of nonreplication of the grating profile at film interfaces on anomalous diffraction is investigated; a transition from trapezoidal profile at the grating substrate to a rounded relief at the top surface of the multilayer structure is assumed. It seems likely, however, that the effect of nonreplication would be to broaden the resonance and reduce the coupling strength while simultaneously increasing absorption. This has been

confirmed by preliminary experimental and analytical work.<sup>4</sup> Numerical calculations reported herein indicate that a small degree of nonreplication has only a minimal impact on the guided-wave resonance phenomena.

A comparison between theory and experiment for a single-layer-overcoated grating is made in Chapter 7. Chapter 8 presents a summary of results as well as suggestions for future work.

## Chapter 2

### HISTORICAL SURVEY OF ANOMALOUS EFFECTS FROM UNCOATED AND COATED DIFFRACTION GRATINGS

#### INTRODUCTION

It might be expected that the efficiency of a grating in a diffracted order (the ratio of the energy in a diffracted order to the incident energy) would be a smooth function of wavelength. However, such is not the case. Anomalous effects from diffraction gratings were first observed by Wood<sup>5</sup>; when using a white light source, he found abrupt changes in the spectral intensities over a small wavelength range. Much of the subsequent experimental and theoretical investigations of anomalous effects from gratings were made in order to explain the anomalies observed by Wood. The efforts by Rayleigh<sup>1</sup> and others successfully predicted some of the features of the diffraction intensity profiles. However, Rayleigh's explanation of the Wood anomalies as due to the appearance of a new spectral order was not sufficient to account for all the intensity variation observed. New insight into the anomalous behavior of gratings was provided by Hessel and Oliner<sup>6</sup> by theorizing that two distinct types of anomalies exist. The first is a nonresonance feature associated with Rayleigh's explanation of a redistribution of energy when a diffracted order disappears or emerges from the grating surface. The second is a resonant anomaly connected with surface plasmon excitation or guided-wave propagation. Nonresonant and



resonant anomalies may occur separately, as for overcoated gratings as well as for bare gratings with deep grooves—or they may coincide, as is observed for uncoated gratings with shallow groove profiles. Many observations reported in the literature<sup>7-9</sup> concern the mergence or reluctance to merge of these anomalies under various conditions.

There are a number of good historical surveys of anomalous effects from diffraction gratings.<sup>6,7,10-12</sup> Phenomena associated with Rayleigh anomalies and surface plasmon excitation on bare metallic gratings have been studied extensively. When thin films are deposited on a grating surface to protect the metallic grating or to enhance performance, the film boundaries are modulated; this replicates the grating profile to various degrees. Diffraction anomalies from modulated layer structures of this sort have features that differ from those of uncoated gratings. These differences are important in that an increase in anomalous diffraction may occur under certain conditions.

In this chapter, anomalous effects from uncoated gratings are reviewed first. Observations of anomalous effects by Wood and the theory of Rayleigh that attempted to explain these observations are described. The Rayleigh theory, however, failed to account for a number of significant observations. The reasons for the failure and the attempts to improve upon Rayleigh's theory are discussed. An exact formulation of the diffraction problem was made using rigorous analytical techniques based upon integral equation methods. Also reviewed are theoretical and experimental investigations of plasmon oscillations that led to further understanding of grating anomalies. Finally, we look at more recent research of anomalous effects from coated

gratings where excitation of guided waves plays a critical role in diffraction efficiency.

## UNCOATED METALLIC GRATINGS

### WOOD'S ANOMALIES AND RAYLEIGH'S THEORY

Anomalous diffraction effects from gratings are not new discoveries. As early as 1902, using a white light source, Wood<sup>5</sup> observed rapid variations in the intensity of diffracted spectral orders from reflection gratings. Instead of observing a smooth continuous spectrum for fixed angle of incidence, dark and bright bands appeared over a narrow wavelength range. He noticed that light missing from dark bands in the zero-order reflected beam corresponded to bright lines in the diffracted beam, and, conversely, that light missing from dark bands in diffracted beam was to be found in the bright lines of the zero-order. Furthermore, Wood observed these anomalies for TM polarization only when the ruling lines were perpendicular to the plane of incidence—never for TE polarization. The electric field parallel to plane of incidence is called transverse magnetic (TM), and the electric field perpendicular to the incident plane is termed transverse electric (TE).

The effects observed by Wood were called anomalies because they could not be explained by the grating theory of the time. The scalar diffraction theory of Fresnel-Kirchhoff<sup>13</sup> described the efficiency of a grating in terms of the Fourier transform of the groove profile. The Huygens and Kirchhoff assumptions are implicit in the Fourier optics theory. This theory assumes

that light propagates across the grating surface, is then reflected, and interferes constructively or destructively with other reflected beams to produce the diffracted wave front. Because the theory does not impose any boundary conditions that couple together the various diffraction orders, it was inadequate to predict anomalous efficiencies. In fact, it was not until the early 1970s that rigorous theories were developed that could predict, with the aid of high-speed computers, the observed efficiencies of a grating from the groove profile.

The first theoretical treatment of Wood's anomalies was given by Rayleigh<sup>1</sup> in 1907 in a paper called "On the Dynamic Theory of Gratings." His theory was based upon an expansion of the diffracted field in terms of outgoing plane waves and allowed coupling between the diffracted orders by means of surface boundary conditions. In his paper, he considered a plane wave incident on a sinusoidal profile surface and postulated the reflected field to be a discrete sum of outgoing planes or evanescent waves above the surface and within the selvage region of the grating.

Having assumed that the diffracted field could be expanded in terms of outgoing wave functions, Rayleigh suggested that the anomalies resulted from the redistribution of light when a diffracted order 'passes off' over the horizon. In other words, a singularity in the scattered field occurs when a spectral order is diffracted from the grating at grazing angle ( $\pm 90^\circ$ ). With the disappearance or emergence of an order, a rearrangement of energy in the diffracted orders is assumed to take place and can be expressed as a sum of plane waves whose amplitudes are determined from electromagnetic boundary conditions.

The wavelengths that correspond to Wood's anomalies have become known as Rayleigh wavelengths ( $\lambda_R$ ) and can be determined from the grating equation:

$$\sin \theta_d = \sin \theta_o + m \frac{\lambda_R}{D} = \pm 1, \quad (1)$$

where

$D$  = groove spacing

$\theta_o$  = incident angle

$\theta_d$  = diffracted angle at  $+90^\circ$  for positive grazing orders and  $-90^\circ$  for negative grazing

$m$  = positive or negative integer corresponding to the diffracted order.

As the angle of incidence decreases,  $\lambda_R$  for positive order becomes larger; for negative order, it moves to smaller wavelengths.

#### FAILURE OF THE RAYLEIGH THEORY

Even though the Rayleigh theory predicted anomalies for TM-polarized light at just those wavelengths found by Wood and that they should be absent for TE orientation, it failed to explain the dark bands observed by Wood and to correctly predict the intensity distribution in the diffracted orders.

Anomalous effects in metallic gratings were further investigated by Wood,<sup>14,15</sup> where the dark bands in the diffraction spectra were hypothesized to be caused by destructive interference of surface waves along the grating. Observing that the total light reflecting from the grating was

less than that reflecting from an unruled area, Wood attempted—unsuccessfully—to determine if the anomalies corresponded to increased absorption by the grating.

Attempts to overcome the limitations of Rayleigh's theory were made by Fano<sup>16</sup> and Artmann<sup>17</sup> by assuming the grating material to be a lossy, nonperfect conductor. Fano explained Wood's anomalies as the interaction of surface waves with the incident light. He assumed that a diffracted wave at grazing angles (which he called a superficial wave) travels along the grating surface. If the superficial wave travels to the adjacent groove so that it is in phase with the incident light, a resonance condition develops and anomalous behavior results in the diffracted waves. This condition can be described mathematically<sup>18</sup> by

$$\frac{D \sin \theta_0}{\lambda} + \frac{D}{\lambda_p} = m, \quad (2)$$

where  $\lambda$  and  $\lambda_p$  are the wavelengths of the incident and superficial waves, respectively. This may also be written as

$$\sin \theta_0 = \frac{c}{v} + m \frac{\lambda}{D}, \quad (3)$$

where  $c$  and  $v$  are the velocities of light and the surface wave, respectively. If  $v = c$  or equivalently  $\lambda_p = \lambda$ , these equations define the Rayleigh wavelength. Thus, for lossy metallic gratings, Fano predicted a displacement of the anomalies from the Rayleigh wavelengths toward longer wavelength.

Extensive observations by Hutley and Bird<sup>8,19</sup> revealed anomalies that occurred at wavelengths other than the Rayleigh wavelength. These resonant anomalies were shown to be associated with surface waves (plasmons) supported by the grating. The two types of anomalies—one associated with the redistribution of diffracted light at the Rayleigh wavelength and the other caused by the resonant effects—were observed to occur separately or at other times to coincide.

The theoretical investigations of McPhedran and Waterworth<sup>9</sup> demonstrated much of the properties of grating anomalies observed by Hutley. Although exact agreement was not achieved, discrepancies were probably caused by the assumption of a perfect conducting grating. They showed that the effect of increasing the groove depth of a sinusoidal grating was to increase the width of the anomalous region and increase the separation of the resonant peak from the Rayleigh wavelength. As the groove-depth-to-incident-wavelength ratio increases further, the Rayleigh wavelength occurs at an inflection point in the slope of the efficiency curve. These trends indicate the effects of increased damping of the resonance as a departure from the assumption of shallow surface profile is made.

Not only was the Rayleigh theory limited in predicting the shape of the diffracted intensity curves, but it also failed to account for anomalies caused by the TE-polarized light. The theoretical studies of Fano and Artmann agreed with Rayleigh's conclusion that failed to predict TE anomalies. There is a simple explanation in terms of Rayleigh's hypothesis that explains why anomalies could only occur for TM polarization.<sup>19</sup> For TM polarization, the electric vector lies in the plane of incidence and perpendicular to the groove

orientation. For a diffracted beam at grazing angle, the electric field would be modulated by the groove profile. For TE polarization, however, the electric field vector lies in the direction of the grooves and, for a perfect conductor, cannot be sustained. Thus, the field strength is much larger for TM than for TE polarization, and more energy is available for redistribution when a diffracted order passes off. Palmer,<sup>20,21</sup> however, confirmed the existence of anomalies for TE-polarized light when using gratings with grooves much deeper than the wavelength of the incident light. Furthermore, the TE anomalies were much fainter than the corresponding TM anomalies but occurred at exactly the same wavelengths.

The primary reason for the failure of the Rayleigh theory was the unrealistic assumption that the grooves were shallow compared to the wavelength of the incident light. The Rayleigh hypothesis, which assumes outgoing plane waves only, was questioned in 1953 by Lippmann.<sup>22</sup> Although the outgoing plane wave expansion is correct outside the groove region, it is not necessarily the complete solution within the selvage region. This choice of the scattered field is justified well away from the groove region where the radiation condition requires plane waves. A point within the groove region receives energy from the incident field as well as from the diffracted fields, which includes contributions from fields scattered off the sides of the groove in both the outgoing and incoming directions. This omission of incoming waves in the selvage region inherent in the Rayleigh hypothesis becomes more serious as the groove depth increases. Utilizing a multiple scattering technique and without assuming shallow grooves, Twersky<sup>23</sup> was able to predict TE as well as TM anomalies.

In the 1960s, the validity of the Rayleigh plane wave assumption was determined analytically. For a sinusoidal groove profile of the form  $z = b \cos(2\pi/D)$ , Petit and Cadilhac<sup>24</sup> demonstrated that the Rayleigh assumption is invalid when  $b/D > 0.0713$ . By locating singularities of solutions to the Helmholtz equation in the complex plane, Millar<sup>25,26</sup> demonstrated that the Rayleigh assumption is strictly valid only if  $0 < b/D < 0.0713$ . Furthermore, it has been shown that it is never valid for profile shapes (i.e., triangular or rectangular) that contain a singularity (sharp corner).<sup>27</sup> Nevertheless, it is possible to modify Rayleigh's method by developing a sequence of linear combinations of plane waves such that the sequence converges to the diffracted field.<sup>28</sup> Even when used outside of the domain of analytical validity, accurate numerical results can be obtained for shallow groove profiles five times larger than the theoretical limit.<sup>29,30</sup>

#### RIGOROUS THEORY OF GRATING DIFFRACTION

A rigorous analysis of the problem of diffraction by a grating, which considers the exact groove shape, is a difficult boundary value problem involving the integration of Maxwell's equations. Only with the assistance of high-speed computers can accurate computational results be achieved. Because integral methods entail an integration of the fields along the groove profile, the scattered field is everywhere properly accounted for. However, because of its simplicity over integral techniques, the Rayleigh hypothesis is still useful for analyzing diffraction from shallow groove gratings.

The first rigorous techniques used to analyze the problem of diffraction by a perfectly conducting grating were based upon integral methods that



take into account the effect of multiple scattering within the groove region. They were originally proposed by Petit and Cadilhac,<sup>31</sup> Wirgin,<sup>32</sup> and Uretski<sup>33</sup> for TE polarization only and for specific groove profiles. A more rigorous approach by Pavageau and Bousquet<sup>34</sup> was capable of calculating diffraction for both TE and TM polarization and for any infinitely conducting grating. Employing the integral formulation of Pavageau and Bousquet, McPhedran and Waterworth,<sup>9</sup> McPhedran and Maystre,<sup>35</sup> and Maystre and Petit<sup>36</sup> calculated anomalies for sinusoidal and blazed profile gratings.

The assumption of infinitely conducting gratings inherent in the early integral methods failed to account for two experimental observations. First, Strong<sup>37</sup> found in 1936 that the position of the anomalies for visible wavelengths was influenced by the type of metal used to coat the grating. Secondly, Hagglund and Sellberg<sup>38</sup> observed that significant absorption evidently occurred in the region of the anomaly. Thus, the theoretical formalism of an infinitely conducting grating that may be adequate for infrared wavelengths could not predict, successfully, anomalies at visible wavelengths.

An integral method was developed by Maystre<sup>39,40</sup> to analyze diffraction from nonperfect conducting or dielectric gratings. Another calculational technique used to explore the problem of the interaction of light with rough surfaces is based upon the extinction theorem. This technique is exact and does not require the Rayleigh-Fano hypothesis of plane waves near the grating surface. The extinction theorem was employed by Toigo *et al.*<sup>2</sup> to describe the scattering of light from a single rough surface of a material of finite permittivity. Waterman utilized an extinction theorem method to

analyze scattering from a single surface of periodic roughness.<sup>41</sup> The extinction theorem has been used also to obtain the dispersion relation for a surface wave across a metallic grating.<sup>42-44</sup> Details of the extinction theorem technique are given in Chapters 4 and 5.

### PLASMON EXCITATION

Another approach to understanding the grating anomalies was to investigate the influence of grating profile on surface plasmons, which are the collective wave-like oscillations of the free electrons on the surface of a metal. The existence of surface plasmons was postulated by Ritchie<sup>45</sup> in 1957, who showed that the plasmon wave vector  $k_p$  for a given oscillation frequency  $\omega$  was of the form

$$k_p = \frac{\omega}{c} \left( \frac{\epsilon_1(\omega)}{1 + \epsilon_1(\omega)} \right)^{1/2}, \quad (4)$$

where  $\epsilon_1(\omega)$  is the real part of the dielectric function given by

$$\epsilon_1(\omega) = n^2 - K^2,$$

where  $n$  and  $K$  are the real and imaginary parts, respectively, of the refractive index.

Coupling the incident light into a plasmon takes place only for TM polarization and only when the surface is rough. Since a grating surface can be considered as periodic roughness, coupling of incident TM light

occurs when the tangential component of the incident wave vector  $k_o$  plus the wave vector associated with the grating  $k_g$  match the wave vector of the surface plasmon. The condition for coupling is, therefore,

$$k_o + k_g = k_p \quad (5)$$

or

$$\frac{\omega}{c} \sin\theta_o + m \frac{2\pi}{D} = \frac{\omega}{c} \left( \frac{\epsilon_1(\omega)}{1 + \epsilon_1(\omega)} \right)^{1/2} . \quad (6)$$

For a free-electron-like metal where  $\epsilon_1(\omega)$  is large, the plasmon wave vector approximately equals  $\omega/c$  and this expression becomes identical to Equation (1), which describes the Rayleigh wavelength. Thus, for a low-profile metallic grating in the infrared, the Rayleigh and plasmon anomalies would coincide. Expression (6), however, is only an approximation, since it takes no account of the grating surface profile other than the period and assumes that the grating does not perturb the surface plasmon oscillations.

It must be mentioned that the description of anomalous effects in gratings in terms of (1) propagating and evanescent orders or (2) surface plasmons is equivalent in that both are based upon Maxwell's equations.

Fano<sup>16</sup> was probably the first to suggest that the excitation of surface (superficial) waves was responsible for Wood's anomalies. In 1968, Ritchie *et al.*<sup>46</sup> analyzed diffraction anomalies found in TM-polarized light in terms of resonant coupling between the incident electromagnetic wave and plasmon waves on the grating surface. This incident photon-diffracted photon surface process was interpreted from quantum-mechanical calculational

methods as a second-order effect whereby surface plasmons exist in an intermediate virtual state between the incident and diffracted photons.

Kroger and Kretschmann<sup>47</sup> studied theoretically the influence of surface roughness on plasmon dispersion by perturbatively solving an integral equation system. The dispersion of surface plasmons by a sinusoidal diffraction grating was studied also by Reinisch and Neviere<sup>48</sup> using a nonperturbative integral theory and Glass *et al.*<sup>49</sup> employing the extinction method. Although the mathematical details differ, these authors agree in the general conclusions. It was found that at first the plasmon wave amplitude increases with increasing groove depth ( $h$ ) and then decreases as  $h$  is further increased. Because of the plasmon excitation, the zero-order reflected beam exhibits a strong minimum. Due to grating-induced radiative damping, the plasmon and specular beam linewidth increases proportionally to  $h^2$ . This damping depresses the dispersion curve below the zero roughness dispersion curve. Finally, the plasmon peak shifts toward lower frequencies at constant incident coupling angle as  $h$  increases.

These theoretical predictions were supported in general by the experimental findings of Pockrand and Raether.<sup>50</sup> Further studies<sup>51,52</sup> show that the -1 diffracted order anomaly caused by the plasmon resonance also displays a minimum. However, the influence of higher harmonics of the surface profile (resulting from deviations of grating profile from an exact sinusoid) was found to deform the expected minimum into a maximum. Higher diffracted orders display very different resonant structures,<sup>53</sup> which appear as a maximum and minimum typical of harmonic oscillation. It was determined also that the form of the efficiency profile strongly depends on

the grating modulation height; to a small degree, it depends on the shape of the groove profile. However, for a low-profile grating whose period and configuration allow only one diffracted order in addition to the specular, the diffracted light is distributed between the -1 order and specular in proportion to the groove depth.

### OVERCOATED GRATINGS

Improved optical performance may be realized by overcoating metallic diffraction gratings with a dielectric layer or multilayer. For example, a single dielectric layer is commonly used to prevent the formation of an oxide layer on aluminum or silver gratings. Also, a dielectric stack of alternating high- and low-index material provides enhanced efficiency for gratings used as wavelength selectors in tunable lasers. Other areas of application include acousto-optics, integrated optics, holography, and spectral analysis.<sup>54</sup>

The presence of a dielectric layer cannot only disturb the shape of the bare grating efficiency curve, but it can influence the behavior of the anomalous diffraction region. A single dielectric layer or composite dielectric structure can support a wider class of guided waves than metallic surfaces. The guided waves may be of either TE or TM polarization, and more than one mode may be associated with each polarization depending upon the phase thickness of the layer. The influence of a dielectric layer on grating anomalies was first realized by researchers working with an uncoated grating. They observed that the shape and position of the anomalies depended upon the condition of the grating surface.

A thin oxidation layer over the grating surface was hypothesized by Ritchie *et al.*<sup>46</sup> to be responsible for deviations between the observed resonance and the theoretically determined plasmon dispersion curve. Soon after, Cowan and Arakawa<sup>55</sup> demonstrated that dielectric films alter the position of the bare grating anomalies. It was observed that dielectric layers only 50 Å thick shifted the resonant peaks to longer wavelengths. For thicker dielectric layers, additional anomalies were observed to occur.<sup>56</sup>

A dielectric multilayer is used also on high-power optical elements for use in the infrared. Beam sampling is necessary to monitor the phase and shape of the wave front; however, ordinary beamsplitters could not survive these intense power levels. To overcome this difficulty, a multilayer-overcoated, low-efficiency grating (where the grating amplitude is a few percent of the wavelength) is utilized that diffracts a small portion of the incident light for beam diagnostics while achieving enhanced specular reflection of the high-energy beam.

Diffraction of light by periodic structures has been analyzed by numerous methods that incorporate a wide range of assumptions. The importance of predicting diffraction efficiencies and absorption for multilayer-coated gratings for use as high-energy beamsplitters has led to the development of an improved integral method. The differential technique of Neviere<sup>57,58</sup> was capable of efficiency calculations for multilayer structures. However, numerical difficulties developed for calculations with low-conductivity metals in the visible and infrared wavelength region. In collaboration with the Air Force Weapons Laboratory, Albuquerque, NM, Maystre<sup>59-61</sup> modified his integral formalism to include the effect of

dielectric multilayer structures with low-modulation interface profiles. Utilizing this integral formalism, Maystre showed that the energy absorbed by a diffraction grating can be reduced drastically by overcoating with a multilayer high-reflection coating. On the other hand, he went on to show that a large increase in absorption can occur at a certain incident angle caused by the excitation of guided-wave modes in the dielectric films. However, in this study,<sup>59-61</sup> anomalies in the diffracted orders caused by the guided-wave excitation were not addressed. The problem of diffraction from a grating also has been analyzed utilizing a coupled-wave approach in which the grating region is divided into a number of horizontal slabs. The relative permittivity of the selvedge region is periodic and is expanded in a Fourier series. This technique has led to very stable numerical results for high grating-amplitude-to-wavelength ratios.

Observation of anomalies in the diffracted beam from a multilayer-overcoated grating was made by Mashev and Popov.<sup>62</sup> A strong anomalous *drop* in the first-order efficiency caused by the guided-wave excitation was reported. These authors drew the conclusion that, in general, guided-wave excitation reduces the efficiency of overcoated gratings. The reason that anomalous behavior was observed by these authors as a minimum in diffraction efficiency was caused probably by the particular grating profile. The grating was fabricated interferometrically in a photoresist, which usually results in a sinusoidal groove shape. It has been shown that, whereas a trapezoidal or laminar profile allows much of the guided-wave energy to outcouple into the outgoing diffracted orders, a sinusoidal or 50% duty cycle laminar profile suppresses such effects, resulting in increased absorption.<sup>3</sup>

Mashev and Popov<sup>63</sup> also have investigated the zero-order diffraction efficiency of a three-layer, dielectric-coated sinusoidal grating. In this case, the resonant anomaly was associated with an increase in the reflection of the specular beam. A theoretical study by these authors<sup>64</sup> predicts a modulation of the zero-order anomalous diffraction efficiency from 0 to 100% for a corrugated single-layer dielectric waveguide. Again, nonzero anomalous diffraction was not an issue.

High-diffraction efficiency has been observed in multilayer dielectric-overcoated, low-efficiency diffraction gratings designed for high reflection of an infrared beam.<sup>65</sup> For shallow-ruled gratings, the efficiency is influenced by the groove depth ( $h$ ) and period ( $D$ ), is influenced approximately by  $(h/D)^2$ , and is nearly constant over a large range of incidence angles.<sup>66</sup> However, at certain precise angles of incidence that depend on the characteristics of the grating and the dielectric overlayers, guided-wave coupling results in enhanced diffraction. For high-efficiency gratings, however, the smooth, bare, grating-efficiency curves are transformed into irregular curves; the increase in diffraction efficiency is not as dramatic because of the heavy damping of the guided wave.

A comparison of theory and experiment of anomalous resonance effects on a nine-layer-overcoated, low-efficiency grating was made.<sup>4</sup> The numerical analysis based on the Rayleigh-Fourier method compared closely with observed resonant angles and efficiencies. When the grating was irradiated with infrared wavelength light at certain precise angles of incidence, a dramatic increase in the -1 diffracted order intensity occurred. It was accompanied by a reduction of intensity in the specular beam.



Anomalous diffraction associated with coupling into the 0th, 1st, and 2nd guided-wave modes of the nine-layer structure was observed.<sup>65</sup> Numerical computation supported by experimental data shows a reduction in resonant width as well as a decrease in diffraction efficiency as the guided-wave coupling increased.

An important factor that influences diffraction efficiency is the degree of replication of the grating profile at each interface of a multilayer coating. Perfect replication of the substrate groove profile through the multilayer coating was assumed in the analysis reported in Reference 4. Thus, perfect phase correlation between interfaces was inherent in the calculated effects. However, perfect transfer of the substrate relief to the film boundaries does not occur in all instances. When thin films are deposited on modulated surfaces, the boundaries between film layers are also modulated.<sup>67</sup> The modulation period is usually the same; however, depending on the ruling amplitude and deposition conditions, the depth and shape of the profile may differ from that of the grating surface. For example, profilometry measurements on a nine-layer-coated grating with low-modulation relief displayed almost complete profile transfer; whereas, a similar coating design on a blazed grating resulted in a sinusoidal surface profile.<sup>68</sup> Diffraction by a three-layer modulated structure with slightly varying interface profiles has been considered analytically.<sup>69</sup> However, the solution was written as a power series expansion for small height-to-wavelength parameters, and resonant effects were not explicitly considered.

## CHAPTER SUMMARY

Diffraction anomalies are rapid variations over a narrow wavelength region (or over a narrow range of incidence angles at constant wavelength) in the intensity of light diffracted from gratings. Rayleigh was the first to theorize on the existence of Wood anomalies. He suggested that they result from the redistribution of light when a diffracted order grazes the surface of a grating. This occurs at a particular wavelength known as the Rayleigh wavelength. Subsequent investigations revealed the limitations of the Rayleigh theory. Not only did anomalous effects occur for TM grating orientation but TE as well, which were not predicted by Rayleigh. Also, it was evident that some anomalous features in the diffracted spectra occurred at wavelengths other than the Rayleigh wavelength. These anomalies were associated with resonant coupling of the incident light into plasmons supported by the grating and occur only for TM-polarized light. In addition to surface plasmons, composite dielectric structures can support a wider class of guided waves; they may be either TE- or TM-polarized and, within a given dielectric layer, may be evanescent or oscillatory. Phenomena associated with Rayleigh anomalies and plasmon excitation are reported extensively in the literature. Guided-wave excitation and anomalous diffraction efficiencies for multilayer-overcoated gratings, however, have received less attention. Much of the work in this area has concentrated on high-efficiency gratings with sinusoidal profiles. Furthermore, guided-wave excitation is usually not a focal point in these investigations. The influence of thin-film or grating-profile characteristics on anomalous diffraction efficiencies has not been investigated extensively.

The importance of groove profile on anomalous diffraction was widely recognized, but the difficulties of grating fabrication limited the data base from which to draw conclusions. Most observations of anomalous effects were made with sinusoidal or echelette (highly blazed) gratings. Anomalies from laminar (rectangular) and triangular profile gratings also have been investigated but to a lesser extent. Systematic studies involving theoretical analysis based on the formalism of Maystre and extensive experimental observations present efficiency data for echelette, blazed, sinusoidal, and laminar profile gratings.<sup>70</sup> However, the influence of these grating profiles on anomalous diffraction was not considered in detail.

### Chapter 3

#### GRAPHICAL METHOD FOR THE DETERMINATION OF WAVEGUIDE MODE IN MULTILAYER-OVERCOATED DIFFRACTION GRATINGS

##### INTRODUCTION

Light incident upon a periodic rough surface—or grating—is diffracted into specific directions: a specular (or 0th order) and a number of diffracted and transmitted orders. The diffraction angles  $\theta_d$  for light reflected back into the incident medium are given by the grating formula

$$\sqrt{\epsilon_0} \sin \theta_d = \sqrt{\epsilon_0} \sin \theta_o + m \frac{\lambda}{D}, \quad (7)$$

where  $\epsilon_0$  is the permittivity of the incident medium (the other symbols have been defined previously). The angles of the diffracted orders transmitted into medium 1 are given by the corresponding equation

$$\sqrt{\epsilon_1} \sin \theta_d = \sqrt{\epsilon_0} \sin \theta_o + m \frac{\lambda}{D}. \quad (8)$$

If air is the incident medium, then  $\epsilon_1 > \epsilon_0$ ; therefore, it is possible to have more diffracted orders in transmission than in reflection. This has

important consequences on the optical performance of coated gratings when guided-wave coupling occurs.

If medium 1 is a thin film, it may support a number of guided-wave modes. These may be characterized by propagation angles  $\theta_{gw}^m$  or wave vectors  $(\omega/c) n_1 \sin \theta_{gw}^m$ . If a transmitted diffracted order with angle  $\theta_d$  coincides with a guided-wave propagation angle, then it is possible to achieve coupling of the incident light into guided waves supported by the thin film (see Figure 1). The wave-vector equation may be written as

$$k_{gw}^m = k_o + m \frac{2\pi}{D}, \quad (9)$$

which is just Equation (8) multiplied by  $2\pi/\lambda$ . The above is actually a vector equation in which  $k_{gw}$  may be positive or negative. Thus,  $k_{gw} > 0$  and  $k_{gw} < 0$  indicate guided waves propagating in the  $+x$  and  $-x$  directions, respectively. A multilayer system may support a number of guided-wave modes, which are classified by mode number 0, 1, 2, ... and arranged such that the  $k_{gw}^{(0)} < k_{gw}^{(1)} < k_{gw}^{(2)}$ , etc. The parameter  $m$  indicates the number and direction of grating wave numbers  $2\pi/D$ .

The theory of guided modes in a single, dielectric, thin film is well known.<sup>71</sup> Waveguiding in a multilayer has been investigated utilizing the substrate-to-top-layer-transfer equation.<sup>72</sup> Also, an admittance approach has been used to determine allowable modes in a planar dielectric waveguide.<sup>73</sup> The admittance, which is the ratio of the magnitudes of the magnetic to the electric fields, is a powerful concept in analyzing reflection and transmission of a thin-film assembly. A similar method is used here.

Waveguide modes are determined by developing a phase expression in terms of the admittance of the multilayer. This technique has an advantage in that guided-wave modes can be analyzed in terms of a phase condition or in terms of the reflection coefficient. Bound waves are specified when the denominator of the reflection coefficient vanishes. Another advantage in using the characteristic matrix method is that shifts in the waveguide modes can be determined readily as conditions of the assembly (i.e., film thicknesses or indexes) are altered. This is particularly useful for design considerations when high diffraction efficiency is required for a specific incidence angle.

In this chapter, the characteristic matrix technique used in performance calculations of thin-film multilayer systems is reviewed. Utilizing this technique, it is shown how bound as well as lossy modes of a multilayer thin-film waveguide can be found by calculating the phase shifts of a negative- and a positive-traveling wave within the assembly. It is shown also that, under conditions of no loss within the multilayer stack, an equivalent simple expression involving the admittances of the negative and positive waves also define bound modes.

An analysis is made of guided-wave modes in overcoated diffraction gratings by the characteristic matrix method. As described in this chapter, the analysis assumes that the grating resonant condition can be separated into diffraction of the incident beam at the film interfaces and subsequent waveguiding of the diffracted light within the multilayer assembly. This postulates that the only effect of the grating profile is to couple the incident light into the multilayer stack at angles greater than allowed by simple

refraction at the film surface. Waves at large diffraction angles are trapped within the stack by internal reflection. The perturbation caused by a periodic surface contour on the solution to Maxwell's equations is neglected. A resonance condition is assumed to develop when the angle of the diffracted beam allows coupling into a guided-wave mode. Although the angles at which resonance occurs can be closely approximated by this method, the efficiency of the resonance cannot be determined. A rigorous analysis of resonant effects in multilayer-coated gratings is presented in Chapters 4 and 5.

If we consider guided waves from the point of view of ray optics, a simple phase condition can be arrived at intuitively. Figure 2 shows a single-layer waveguide and the phase fronts associated with a guided ray. The ray travels from point A to B and on to C. For constructive interference to occur, the total phase lag of the beam transversing the optical path A to C must be a multiple of  $2\pi$ . The phase change of the light beam traveling this distance is found from twice the phase thickness of the film  $2\delta$ , plus the phase change on reflection from the bottom surface  $\phi_1$  and top surface  $\phi_2$ . Thus, the condition for a single layer to support a guided wave can be written as

$$\phi_1 + \phi_2 + 2\delta = 2\pi m, \quad (10)$$

where  $m$  is an integer and  $\delta$  is the phase thickness given by

$$\delta = \frac{2\pi}{\lambda_0} nh \cos \theta_{gw} \quad (11)$$

A multilayer waveguide is simply a stack of thin films, and the phase relation [Equation (10)] still can be used to describe the waveguide conditions where the phase thickness of the multilayer must now be considered. In practice, it is convenient to calculate the phase terms by standard mathematical techniques used in the analysis of thin-film optical coatings.

### CHARACTERISTIC MATRIX APPROACH

The characteristic matrix formalism, which is extensively reported in the literature, is of prime importance in optical thin-film analysis and forms the basis of many calculations.<sup>74</sup> The elements of the matrix are solutions to the wave equation that satisfy the conditions of continuity of the tangential components of the electric and magnetic fields across a plane-film boundary. A brief review of the characteristic matrix method for determining admittance and phase through a thin-film multilayer follows.

Thin-film multilayer systems consist of a number of boundaries between homogeneous media. A multilayer assembly of  $J$  layers is shown in Figure 3. The coordinate system is chosen such that the plane of incidence is parallel to the  $x,z$  plane and the  $z$ -axis points down. The film layers are numbered 1 to  $J$  beginning at the superstrate. The refractive index of the  $j$ th layer is referred to as  $n_j$ , where  $n_j$  can be complex. The index of the incident medium is  $n_0$ , and that of the substrate is  $n_s$ . We assume a material discontinuity in the  $z$ -direction only.

We write the electric field  $E$  as

$$\vec{E} = \vec{E}_0 \exp \{ i[\omega t + k_0 n_j (\alpha_j x + \beta_j y + \gamma_j z)] \} \quad (12)$$



This represents plane waves traveling in a direction given by the direction cosines  $(\alpha, \beta, \gamma)$  with amplitude  $E_0$ . The wave vector  $k_0$  is  $2\pi/\lambda_0$ , where  $\lambda_0$  is the wavelength of light in vacuo and  $\omega$  is the angular frequency. For a wave propagating in the plane of incidence,

$$\begin{aligned}\alpha_j &= \cos \theta_j \\ \beta_j &= 0 \\ \gamma_j &= \sin \theta_j\end{aligned},$$

where  $\theta_j$  is the angle of propagation from the normal within the  $j$ th layer.

The ratio of the amplitudes of the magnetic  $H$  to the electric field  $E$  of the wave in the  $j$ th layer is called the optical admittance  $y_j$ ; for normal incidence, it is given by

$$y_j = \frac{H}{E} = y_0 n_j, \quad (13)$$

where  $y_0$  is the admittance of free space and is related to the permittivity  $\epsilon_0$  and permeability  $\mu_0$  of free space by

$$y_0 = \left( \frac{\epsilon_0}{\mu_0} \right)^{1/2} = \begin{cases} 1 & \text{in Gaussian units} \\ 1/377 & \text{Siemens in SI units} \end{cases}. \quad (14)$$

At optical frequencies,  $\mu_0$  is assumed to be unity and the admittance is numerically equal to the refractive index in Gaussian units.

At oblique incidence, the admittance is modified by the propagation angle of the wave in the medium in which it is traveling and has a different value for each of the two polarizations. The modified admittances  $Y_j$  for the two polarizations are

$$Y_j = y_j \cos \theta_j \quad , \quad \text{TE polarization} \quad (15)$$

$$Y_j = \frac{y_j}{\cos \theta_j} \quad , \quad \text{TM polarization} \quad (16)$$

The matrix

$$M_j = \begin{bmatrix} \cos \delta_j & \frac{i}{Y_j} \sin \delta_j \\ i Y_j \sin \delta_j & \cos \delta_j \end{bmatrix} \quad (17)$$

characterizes the  $j$ th layer of a thin film by containing constants relevant to one layer of the stack only and is called the characteristic matrix. In this matrix expression,  $\delta_j$  is the phase thickness of the  $j$ th layer and  $Y_j$  is the modified admittance given by Equations (15) and (16).

For a thin-film assembly of  $J$ -layers, the equivalent characteristic matrix of the assembly is the product of the individual matrices beginning at the substrate, i.e.,

$$M = \prod_{j=J}^1 M_j \quad (18)$$

Since there is only a positive-going wave in the substrate, the tangential components of  $E_0$  and  $H_0$  at the surface of the multilayer are related to the

tangential components of  $E_s$  and  $H_s$ , which are transmitted through the final interface into the substrate by

$$\begin{bmatrix} E_o \\ H_o \end{bmatrix} = \left\{ \prod_{j=J}^1 M_j \right\} \begin{bmatrix} E_s \\ H_s \end{bmatrix} . \quad (19)$$

By normalizing the electric and magnetic fields to the electric field at the substrate  $E_s$ , we arrive at

$$\begin{bmatrix} A \\ B \end{bmatrix} = \left\{ \prod_{j=J}^1 M_j \right\} \begin{bmatrix} 1 \\ Y_s \end{bmatrix} . \quad (20)$$

The equivalent admittance  $Y$  of the multilayer assembly is then

$$Y = \frac{B}{A} , \quad (21)$$

and the reflection coefficient  $\rho$  is

$$\rho = \frac{Y_o - Y}{Y_o + Y} , \quad (22)$$

where  $Y_o$  is the modified admittance of the incident medium.

## WAVEGUIDE MODES

In this section, the technique for determining allowed waveguide modes from the modified admittance of a multilayer assembly is discussed.

Bound as well as lossy modes occur within a thin-film stack when the phase condition of Equation (10) is satisfied. For bound modes, the wave is confined within the stack by total internal reflection; energy flow is in the direction parallel to the film interfaces. In an ideal system, total internal reflection occurs at the top surface and substrate interfaces; no power is lost from the system. In a lossy system, the field decays as the wave propagates down the multilayer. If absorption is neglected within the dielectric layers of a multilayer-overcoated diffraction grating, energy loss from the guided wave occurs by two methods: (1) diffraction into air of the beam at the top surface and (2) absorption in the metal substrate.

The technique used to determine guided-wave modes within a multilayer assembly involves the calculation of the phase-shift terms in Equation (10) for a wave traveling in the positive and negative  $z$ -directions. The situation is illustrated in Figure 3, which shows a multilayer waveguide assembly. For purposes of phase calculation, the multilayer may be divided at any convenient  $z$ -plane within the stack. The top surface is chosen here for illustration. The positive-traveling wave begins at the top surface, reflects off the substrate, and returns to the surface with total phase  $\phi_+$ . This phase term includes the phase shift resulting from twice the optical thickness of the multilayer and the phase shift on reflection from the substrate. The negative-traveling wave is allowed only a phase shift  $\phi_-$  on reflection from the surface boundary layer.

We assume that the negative-traveling wave is incident at the top surface beyond the critical angle and that total internal reflection occurs. For this wave, the medium above the surface of the stack becomes the effective substrate. The modified admittance of the air substrate is then

$$Y_o = y_o \cos \theta_o, \text{ for TE} \quad (23)$$

$$Y_o = \frac{y_o}{\cos \theta_o}, \text{ for TM} \quad (24)$$

where  $y_o = 1$ . Since total internal reflection has occurred,  $\cos \theta_o$  is imaginary. Using Snell's law,

$$y_o \sin \theta_o = y_1 \sin \theta_1 \quad (25)$$

and

$$\cos^2 \theta_o + \sin^2 \theta_o = 1. \quad (26)$$

Equations (23) and (24) can be written

$$Y_o = \begin{cases} -i\{y_1^2 \sin^2 \theta_1 - y_o^2\}^{1/2} & , \text{ for TE} \\ -i\left\{\frac{y_1^2}{y_o^4} \sin^2 \theta_1 - \frac{1}{y_o^2}\right\}^{-1/2} & , \text{ for TM} \end{cases} \quad (27)$$

In this case, since the modified admittance is imaginary, only evanescent waves are present in the air and no energy flow occurs. Furthermore, the negative-traveling wave is allowed a phase shift caused by the reflection only, and the equivalent admittance of this wave  $Y_-$  equals the modified admittance of the air substrate  $Y_0$ .

The reflection coefficient  $\rho_-$  for the negative-traveling wave is

$$\rho_- = \frac{Y_1 - Y_-}{Y_1 + Y_-} , \quad (28)$$

where the appropriate expressions for TE and TM polarization are to be substituted for  $Y_1$  and  $Y_-$ . Since in this case  $Y_-$  is purely imaginary, the phase on reflection  $\phi_-$  is

$$\phi_- = -2 \arctan \left( \frac{\text{Im}Y_-}{Y_1} \right) . \quad (29)$$

For the positive-traveling wave, we use the characteristic matrix expression [Equations (10) and (11)] to arrive at an equivalent admittance  $Y_+$  of the multilayer stack. The reflection coefficient for the wave  $\rho_+$  becomes

$$\rho_+ = \frac{Y_1 - \frac{B}{A}}{Y_1 + \frac{B}{A}} , \quad (30)$$

where  $B/A = Y_+$ . Again, the appropriate values for TE and TM polarization are to be substituted for  $Y_1$ ,  $A$ , and  $B$ .

Multiplying the above expression by  $\rho_+^*$  (where  $*$  signifies the complex conjugate) and separating real and imaginary terms, the phase  $\phi_+$  is found to be

$$\phi_+ = \arctan \left[ \frac{iY_1(BA^* - AB^*)}{Y_1^2 AA^* - BB^*} \right] \quad (31)$$

Substituting Equations (29) and (31) into the phase condition [Equation (10)] results in a general expression whose solutions define guided-wave modes within the multilayer assembly in terms of the mode propagation angle. Since this expression is transcendental, it cannot be solved analytically. Graphical or numerical solutions are required. A graphical technique to determine the solutions to the waveguide expression is discussed below.

There exists a discrete set of solutions in terms of the mode angle or wave vector that satisfies the waveguide expression. For convenience in experimentally identifying modes, the zero mode is assigned to the smallest propagation angle. Higher order mode solutions occur with greater propagation angle. At propagation angles below the critical angle at either the top or substrate interface, a radiation condition exists and the continuum of modes results. This is characterized by standing waves through the multilayer, and the thin-film assembly acts as a reflector of the incident light. In this case, the wave is said to be beyond cutoff.

## BOUND MODES

If the equivalent admittance of the multilayer in Equation (21) is purely imaginary, the phase shift of the positive-traveling wave  $\phi_+$  can be expressed in a manner similar to Equation (29) for the negative-traveling wave. The phase shift  $\phi_+$  becomes

$$\phi_+ = -2 \arctan \left( \frac{\text{Im} Y_+}{Y_1} \right) . \quad (32)$$

Substitution of Equations (29) and (32) into Equation (10) results in a simple expression specifying the waveguide condition in terms of the admittances,

$$Y_+ = -Y_- . \quad (33)$$

If we consider  $Y_-$  as the equivalent admittance of the incident medium and  $Y_+$  as the equivalent admittance of the multilayer assembly, the reflection coefficient can be written as

$$\rho = \frac{Y_- - Y_+}{Y_- + Y_+} . \quad (34)$$

When the admittance condition  $Y_+ = -Y_-$  is satisfied, bound modes are determined by the poles of the reflection coefficient.<sup>3,75</sup>

We have seen that bound modes of a multilayer stack exist if the equivalent admittance of the multilayer is purely imaginary. Equations (20) and (21) show that the admittance of the multilayer assembly becomes



imaginary if the modified admittance of the substrate is itself imaginary. A purely imaginary admittance value for the substrate results for (1) total internal reflection on a dielectric substrate or (2) a pure metal substrate whose index of refraction is purely imaginary.

In the case of total internal reflection from a dielectric substrate, the admittance of the substrate can be expressed similarly to the admittance of the negative-traveling wave at the surface interface, where

$$Y_s = \begin{cases} -i[(y_J \sin \theta_J)^2 - y_s^2]^{1/2} & , \text{ for TE} \\ -i\left[\left(\frac{y_J}{y_s} \sin \theta_1\right)^2 - \left(\frac{1}{y_s}\right)^2\right]^{-1/2} & , \text{ for TM} \end{cases} \quad (35)$$

and multiplication of  $Y_s$  with the characteristic matrix of the multilayer results in a real A and imaginary B value in Equation (21).

## LOSSY WAVES

The phase condition [Equation (10)] applies to leaky waves as well as bound waves, provided correct expressions for the phase of the positive- and negative-traveling waves are used. For a leaky system, the substrate is now absorbing and energy flows from the positive-traveling wave into the substrate.

We have seen that for a substrate whose admittance is imaginary, the expression  $Y_+ = -Y_-$  determines the condition for which bound modes exist within the multilayer stack. For a substrate with complex admittance,

however, the equivalent admittance of the multilayer is also complex. Thus, the total phase shift of the positive-traveling wave given by Equation (31) cannot be simplified in the manner of Equation (32). Furthermore, the admittance condition [Equation (33)] cannot be satisfied since  $Y_+$  is complex and  $Y_-$  is imaginary. In this case, the denominator of the reflection coefficient goes through a minimum (not necessarily zero).

### GUIDED-WAVE CALCULATIONS

Waveguide modes within a multilayer dielectric assembly with smooth interfaces can be found by solving the phase condition. For a metallic substrate, bound modes can be approximated by the admittance condition [Equation (33)], provided the real part of the refractive index of the metal is small compared to the imaginary part.

Guided-wave modes for the multilayer-coated grating designs considered in this work have been determined using the graphical method developed in this chapter [see Figures 8(a) through 8(f)]. The guided-wave modes are determined by the intersection points of the phase curves for the upward- and downward-traveling waves. Discrepancy between the guided-wave modes as determined by the method outlined in this chapter and those found by the rigorous solution (Chapter 6) results from the fact that the planar waveguide method is only an approximation when the perturbations due to groove shape are considered. The smaller the groove height, the better the approximation.

The exact integral equation formulation of the problem of diffraction from multilayer-coated gratings (Chapter 5) may be cast into the following simplified matrix expression:

$$I = MX, \quad (36)$$

where  $I$  is a column vector related to the incident field,  $X$  is a column vector whose elements are related to the unknown diffracted field, and  $M$  is a square matrix. The poles to this expression, specified when the determinant of  $M$  ( $\det M$ ) vanishes, indicate the allowed guided-wave modes. A simple method for finding guided-wave modes is to numerically scan over a wave number until a minimum in  $\det M$  is located. Once the approximate waveguide modes have been determined, the rigorous calculation is utilized to find exact guided-wave modes and to calculate diffraction efficiencies. This graphical method readily locates allowed guided-wave solutions by the intersections of phase curves. The planar waveguide method is advantageous in locating the approximate guided-wave modes and, hence, the approximate incidence angle for which coupling is expected.

### CONCLUSIONS

It has been shown that waveguide modes within a multilayer stack can be determined by calculating the phase or admittance of upward- and downward-traveling waves within the assembly. These calculations involve the characteristic matrix technique commonly employed in optical performance calculations of multilayer coatings. Utilizing the method

presented here, approximate guided-wave modes have been determined for the cases studied in Chapter 6.

## Chapter 4

### EXTINCTION THEOREM: SINGLE SURFACE

#### FIELD EQUATIONS

In this chapter, the extinction theorem relations for a single surface of periodic roughness are developed following the methodology of Toigo *et al.*<sup>2</sup> and Laks *et al.*<sup>44</sup> An excellent review of the extinction theorem as it relates to scattering theory is given by Wolf.<sup>76</sup>

The geometry considered is shown in Figure 4. A dielectric or metallic medium fills the lower space  $z > d_0 + h(x)$  (region  $s$ ) characterized by an isotropic frequency-independent dielectric constant  $\epsilon_s$ . The upper half-space  $z < d_0 + h(x)$  consists of the incident medium of dielectric constant  $\epsilon_0$ . The surface profile function  $h(x)$  is periodic in  $x$  with period  $D$ , and  $d_0$  is the mean reference level of the interface.

The extinction theorem is based on Green's identity.<sup>77</sup> The general form of this identity relates a volume and surface integral and is given by

$$\iiint_{v'} (G_j \nabla^2 U - U \nabla^2 G_j) dv' = \iint_{s'} \left( G_j \frac{\partial U}{\partial n} - U \frac{\partial G_j}{\partial n} \right) ds' , \quad (37)$$

where  $v'$  represents the volume of integration bounded by a closed surface  $s'$ . In this work, the scalar field  $U$  is taken to be a component of either the electric or magnetic field. For example, for TM-polarization,  $U$  is taken to be

the amplitude of the magnetic field vector. The function  $G_j$  is the three-dimensional Green's function associated with an arbitrary medium  $j$  of permittivity  $\epsilon_j$ . The Green's function satisfies the Helmholtz equation<sup>78</sup> in the form

$$\left( \nabla^2 + \epsilon_j \left( \frac{\omega}{c} \right)^2 \right) G_j(\vec{r} - \vec{r}') = -4\pi \delta(\vec{r} - \vec{r}') , \quad (38)$$

which is homogeneous everywhere except at the point  $\vec{r} = \vec{r}'$ . The vectors  $\vec{r} = (x, y, z)$  and  $\vec{r}' = (x', y', z')$  are the observation and source points, respectively. The Green's function in three dimensions may be written explicitly in integral form<sup>79</sup> as

$$G_j(\vec{r} - \vec{r}') = \frac{e^{iK|\vec{r} - \vec{r}'|}}{|\vec{r} - \vec{r}'|} = \frac{i}{2\pi} \int_{-\infty}^{\infty} \frac{e^{i[k(x-x') + \beta(y-y')] + iq_j|z-z'|}}{q_j} dk d\beta , \quad (39)$$

where

$$K = \frac{\omega}{c} \sqrt{\epsilon_j}$$

and

$$\beta^2 + k^2 + q_j^2 = \epsilon_j \left( \frac{\omega}{c} \right)^2 . \quad (40)$$

Green's identity [Equation (37)] is first used by considering a volume enclosing the region above the boundary (incident medium  $j = 0$ ). The

magnetic field anywhere within the volume of integration enclosing the incident medium satisfies the homogeneous Helmholtz equation,

$$\left(\nabla^2 + \epsilon_0 \left(\frac{\omega}{c}\right)^2\right) \vec{H} = 0 \quad (41)$$

where  $\vec{H}$  is the total magnetic field given by  $\vec{H} = \hat{y}H$ .

Green's identity is simplified by substituting  $\nabla^2 G_0$  and  $\nabla^2 H$  from Equations (38) (where  $j = 0$ ) and (41) into Equation (37), resulting in

$$4\pi \iiint_{v'} H \delta(x-x') \delta(y-y') \delta(z-z') dv' = \iint_{s'} \left( G_0 \frac{\partial H}{\partial n} - H \frac{\partial G_0}{\partial n} \right) ds' \quad (42)$$

The surface profile is given by  $z' = d_0 + h(x')$ , and the differential surface area  $ds'$  in Equation (42) may be written as

$$ds' = dy' \sqrt{(dx')^2 + (dz')^2} = dy' dx' \sqrt{1 + (h'(x'))^2} \quad (43)$$

Since the surface is uniform in the  $y$ -direction, integration of Green's function over  $dy'$  results in a Dirac delta function  $\delta(\beta)$ . Further integration over  $d\beta$  results in setting  $\beta = 0$ . This is seen easily by using Equations (39) and (41) in Equation (42). With this, the surface and volume integrals in Equation (42) reduce to one- and two-dimensional integrals, respectively. Thus, the problem in three dimensions can be reduced to an analysis in two dimensions only. The evaluation of the surface integral yields the incident plane wave  $H^{inc}$  plus an integration along the grating surface.

The second integral results in the total field  $H_o^{\text{total}}$  for observation points anywhere within the incident medium. If the points of observation are located outside the incident medium, the integral vanishes. After the procedures outlined above are carried out, Green's identity for the incident medium can be written in the form of the extinction theorem as

$$H_o^{\text{inc}} - \frac{1}{4\pi} \int_s \left( H_o \frac{\partial}{\partial n} G_o - G_o \frac{\partial}{\partial n} H_o \right) dx' \sqrt{1 + h'(x')^2}$$

$$= \begin{cases} H_o^{\text{total}} & z < d_o + h(x) \\ 0 & z > d_o + h(x) \end{cases}, \quad (44a)$$

$$(44b)$$

where  $G_o$  is the two-dimensional Green's function given in integral form by

$$G_o = i \int_{-\infty}^{\infty} \frac{dk}{q_o} e^{i[k(x-x') + q_o |z-z'|]} \quad (45)$$

and  $H_o$  is the magnetic field at the boundary within the incident medium, evaluated from above. Details of the analysis leading to this result are shown in Appendix A. Equation (44b) implies that the magnetic field and its normal derivative on the surface cancels or 'extinguishes' the incident field for all points of observation below the surface  $d_o + h(x)$  and outside the volume of integration. For points of observation above the surface as in Equation (44a), the incident field and the field contributions from the surface generate the total field.

The extinction theorem relations for the lower region are derived in a similar manner as that for the incident medium. In this case, the volume and



surface of integration in Green's theorem [Equation (37)] enclose the lower or substrate region ( $j = s$ ). The magnetic field within the lower region satisfies the homogeneous Helmholtz equation,

$$\left( \nabla^2 + \epsilon_s \left( \frac{\omega}{c} \right)^2 \right) \vec{H} = 0 \quad (46)$$

Substitution of Equations (38) (where  $j = s$ ) and (46) into (37) yields

$$\begin{aligned} & \frac{-1}{4\pi} \int_s \left( H_0 \frac{\partial}{\partial n} G_s - G_s \frac{\partial}{\partial n} H_0 \right) dx' \sqrt{1 + (h'(x'))^2} \\ & = \begin{cases} 0 & \text{for } z < d_0 + h(x) \\ H_s^{\text{trans}} & \text{for } z > d_0 + h(x) \end{cases} \end{aligned} \quad \begin{matrix} (47a) \\ (47b) \end{matrix}$$

where  $H_s^{\text{trans}}$  is the field transmitted into the substrate.  $H_0$  is the magnetic field evaluated on the boundary.

The extinction relation Equation (47a) asserts that the field radiated by induced surface currents must exactly cancel the incident wave when viewed from below the boundary. Equation (47b) states that the induced surface currents radiate into the substrate to form the transmitted magnetic field.

### BOUNDARY CONDITIONS

The extinction theorem relations (44) and (47) may be simplified by utilizing appropriate boundary conditions across the interface defined by  $z_0 = d_0 + h(x)$ . A normal vector,  $\vec{N}$ , to the interface is given by  $\vec{\nabla} z_0$  or

$$\vec{N} = \hat{z} - \hat{x}h'(x) , \quad (48a)$$

where  $h'(x) = \partial h(x)/\partial x$  and  $\hat{z}$ ,  $\hat{y}$ , and  $\hat{x}$  are unit vectors in  $z$ ,  $y$ , and  $x$  directions, respectively. The unit normal is

$$\frac{\vec{N}}{|\vec{N}|} = \hat{n} = (\hat{z} - \hat{x}h'(x))(1 + h'(x)^2)^{-1/2} \quad (48b)$$

The tangent vector  $\vec{T}$  to the surface in the plane of incidence is

$$\vec{T} = \vec{N} \times \hat{y} = -(\hat{x} + \hat{z} h'(x)) , \quad (49a)$$

and the unit tangent  $\hat{t}$  becomes

$$\hat{t} = \frac{\vec{T}}{|\vec{T}|} = -(\hat{x} + \hat{z} h'(x)) (1 + h'(x)^2)^{-1/2} \quad (49b)$$

For TM polarization, the magnetic field ( $\vec{H}$ ) is perpendicular to the plane of incidence. The boundary conditions to be satisfied are the continuity of the tangential components of the magnetic field  $\vec{H}$  and electric field  $E$  at the boundary interface. The electric field for region  $j$  is found from Maxwell's equation,<sup>80</sup>

$$\vec{\nabla} \times \vec{H} = -i \frac{\omega}{c} \epsilon_j \vec{E} \quad (50)$$

The tangential component of  $\vec{E}$  is

$$E_{\text{tan}} = \vec{E} \cdot \hat{t} = i \frac{(\vec{\nabla} \times \vec{H}) \cdot \hat{t}}{\epsilon_j \frac{\omega}{c}} = i \frac{(\vec{\nabla} H \times \hat{y}) \cdot \hat{t}}{\epsilon_j \frac{\omega}{c}}, \quad (51)$$

where  $\vec{H} = \hat{y}H$ . Also, using the vector identity

$$(\vec{B} \times \vec{C}) \cdot \vec{A} = (\vec{C} \times \vec{A}) \cdot \vec{B}, \quad (52)$$

$E_{\text{tan}}$  can be written as a normal derivative of the magnetic field, i.e.,

$$E_{\text{tan}} = i \frac{(\hat{y} \times \hat{t}) \cdot \vec{\nabla} H}{\epsilon_j \frac{\omega}{c}} = \frac{i}{\epsilon_j \frac{\omega}{c}} \frac{\partial H}{\partial n}. \quad (53)$$

In the case of TE polarization, the electric field vector is perpendicular to the plane of incidence and, hence, tangent to the y-x surface. The magnetic field in this case is found from Maxwell's equation

$$\vec{\nabla} \times \vec{E} = i \frac{\omega}{c} \vec{H}. \quad (54)$$

In a manner similar to the derivation of  $E_{\text{tan}}$ , the tangential component of the magnetic field  $H_{\text{tan}}$  is found to be

$$H_{\tan} = \frac{-i}{\frac{\omega}{c}} \frac{\partial E}{\partial n}, \quad (55)$$

where  $\vec{E} = \hat{y}E$ .

Therefore, the boundary conditions to be satisfied by  $H$  for TM polarization are

$$H_{j-1}(j) = H_j(j) \quad z = d_o + h(x) \quad (56)$$

$$\frac{1}{\epsilon_{j-1}} \frac{\partial}{\partial n^-} H_{j-1}(j) = \frac{1}{\epsilon_j} \frac{\partial}{\partial n^+} H_j(j) \quad z = d_o + h(x) ; \quad (57)$$

and for TE polarization,

$$E_{j-1}(j) = E_j(j) \quad z = d_o + h(x) \quad (58)$$

$$\frac{\partial}{\partial n^-} E_{j-1}(j) = \frac{\partial}{\partial n^+} E_j(j) \quad z = d_o + h(x) . \quad (59)$$

In these equations, the subscript on the fields specifies the medium and the index in parentheses designates the boundary. Also,  $\partial/\partial n^-$  and  $\partial/\partial n^+$  signify differentiation along the normal, directed upward and downward, respectively. The relation between the normal derivative is

$$\frac{\partial}{\partial n^-} = - \frac{\partial}{\partial n^+} , \quad (60)$$

where from Equation (48a),

$$\frac{\partial}{\partial n} = \left( \frac{\partial}{\partial z} - h'(x) \frac{\partial}{\partial x} \right) [1 + h'(x)^2]^{-1/2} \quad (61)$$

The analysis carried out in this work is developed for TM polarization, where the field equations involve the magnetic field and its derivative. For TE polarization, the electric field and its derivative are utilized in the extinction theorem equations and the form of the resulting equations are similar to the TM case.

Substitution of the boundary condition [Equations (56) and (57)] and the definition of  $\partial/\partial n$ . [Equation (61)] into the extinction theorem relations [Equations (44) and (47)] results in

$$H_o^{inc} - \frac{1}{4\pi} \int dx \left[ H_o(x', z') \left( \frac{\partial G_o(x-x', z-z')}{\partial z'} - h'(x) \frac{\partial G_o(x-x', z-z')}{\partial x'} \right) - G_o(x-x', z-z') L_o(x', z') \right]_{z'=d_o+h(x)} = \begin{cases} H_o^{total} & \text{for } z < d_o + h(x) \\ 0 & \text{for } z > d_o + h(x) \end{cases} \quad (62)$$

and

$$- \frac{1}{4\pi} \int dx \left[ H_o(x', z') \left( \frac{\partial}{\partial z'} G_s(x-x', z-z') - h'(x) \frac{\partial G_s(x-x', z-z')}{\partial x'} \right) - G_s(x-x', z-z') \frac{\epsilon_s}{\epsilon_o} L(x', z') \right]_{z'=d_o+h(x)} = \begin{cases} 0 & \text{for } z < d_o + h(x) \\ H_j^{trans} & \text{for } z > d_o + h(x) \end{cases} \quad (63)$$

In these expressions, the definition for  $L(x',z') = [1 + h'(x')^2]^{1/2} \partial/\partial n H(x',z')$  has been introduced.  $L_0(x',z')$  and  $G_0(x',z')$  are the fields on the surface evaluated from above, since the boundary conditions have been employed in Equation (63) to transition the surface from the substrate to the incident medium.

Explicit extinction theorem formulas are obtained by using the integral representation of the Green's function, Equation (45). Subtracting the incident field from both sides of Equation (62) and substituting the Fourier representation of the Green's function lead to

$$\frac{1}{4\pi} \int_{-\infty}^{\infty} \int_{-\infty}^{\infty} dx' dk \{ H_0(x',z') i[-q_0 \operatorname{sgn}(z-z') + kh'(x')] - L_0(x',z') \} \\ \times \frac{e^{iq_0|z-z'|} e^{ik(x-x')}}{q_0} = \begin{cases} -H_0^{\text{diff}} & \text{for } z < d_0 + h(x) \\ H_0^{\text{inc}} & \text{for } z > d_0 + h(x) \end{cases}, \quad (64)$$

where  $H_0^{\text{diff}}$  represents the diffracted field in the incident medium. Multiplying the above equation by

$$\int_{-\infty}^{\infty} dx e^{-ik_n x}, \quad (65)$$

where  $k_n = k_0 + n 2\pi/D$ , and carrying out the integration over  $dx$  results in

$$\frac{i}{2} \int_{-\infty}^{\infty} dx' \left\{ H_o(x', z') [q_{n,o} \operatorname{sgn}(z - z') - k_n h'(x')] - i L_o(x', z') \right\}$$

$$x \frac{e^{iq_{n,o}|z-z'|} e^{ik_n x'}}{q_{n,o}} = \begin{cases} - \int_{-\infty}^{\infty} dx H_o^{\text{diff}} e^{-ik_n x} & \text{for } z < d_o + h(x) \\ \int_{-\infty}^{\infty} dx H_o^{\text{inc}} e^{-ik_n x} & \text{for } z > d_o + h(x) \end{cases} \quad (66)$$

where the integral representation of the Dirac delta function,

$$\frac{1}{2\pi} \int_{-\infty}^{\infty} e^{i(k-k_n)x} dx = \delta(k-k_n), \quad (67)$$

has been used. Also,  $q_{n,o}$  is related to  $k_n$  by

$$q_{n,o}^2 + k_n^2 = \epsilon_o \left( \frac{\omega}{c} \right)^2. \quad (68)$$

Note that the integrand in Equation (66) is periodic in  $x$  and that the infinite limits on  $dx'$  are over an infinite number of periods. Thus, Equation (66) can be written as an integral over one period times an integer  $N$ , where  $N \rightarrow \infty$  and becomes

$$\begin{aligned} & \frac{i}{2} N \int_{-D/2}^{D/2} dx \{H(x, z') [q_{n,0} \text{sgn}(z-z') - k_n h'(x)] - iL(x, z')\} \\ & - \int_{-ND/2}^{ND/2} dx H_0^{\text{diff}} e^{-ik_n x} \quad \text{for } z < d_0 + h(x) \end{aligned} \quad (69a)$$

$$\frac{e^{iq_{n,0}|z-z'|}}{q_{n,0}} e^{-ik_n x} = \int_{-ND/2}^{ND/2} dx H_0^{\text{inc}} e^{-ik_n x} \quad \text{for } z > d_0 + h(x), \quad (69b)$$

where the prime on  $x$  has been dropped. Away from the grating surface where  $z < d_0 + h(x)$ , the diffracted field can be expanded as

$$H_0^{\text{diff}} = \sum_{p=-\infty}^{\infty} H_{p,0}^{\text{diff}} e^{iq_{p,0}z} e^{ik_p x} \quad (70)$$

Also, the incident plane wave can be written as

$$H_0^{\text{inc}} = |H_0^{\text{inc}}| e^{iq_{0,0}z} e^{ik_0 x}, \quad (71)$$

where  $|H_0^{\text{inc}}|$  represents the incident field amplitude. Substituting  $H_0^{\text{diff}}$  of Equation (70) into the right side of Equation (69a) gives

$$\begin{aligned} & - \int_{-ND/2}^{ND/2} dx \sum_{p=-\infty}^{\infty} H_{p,0}^{\text{diff}} e^{iq_{p,0}z} e^{ik_p x} e^{-ik_n x} \\ & = - \sum_{p=-\infty}^{\infty} H_{p,0}^{\text{diff}} e^{iq_{p,0}z} \frac{2 \sin(k_p - k_n) ND/2}{(k_p - k_n)} \end{aligned} \quad (72)$$



Since  $k_p - k_n = 2\pi(p-n)/D$ , only the  $p = n$  term survives and the right side of the above equation may be written as

$$- H_{n,0}^{\text{diff}} e^{iq_{n,0}z} ND .$$

Similarly, the right side of Equation (69b) is

$$| H_0^{\text{inc}} | e^{iq_0z} ND .$$

Since the surface profile function is periodic, the H and L fields must possess the Bloch property where

$$H_0(x + a, z') = e^{ika} H_0(x, z')$$

and

$$L_0(x + a, z') = e^{ika} L_0(x, z') .$$

$H_0(x, z')$  and  $L_0(x, z')$  are now expanded in terms of a Fourier series as

$$H_0(x, z') = \sum_{m=-\infty}^{\infty} e^{ik_m x} H_m$$

$$L_0(x, z') = \sum_{m=-\infty}^{\infty} e^{ik_m x} L_m ,$$

which retain the Bloch property and are substituted into Equation (69), resulting in

$$\frac{1}{2q_{n,o}D} \sum_{m=-\infty}^{\infty} \int_{-D/2}^{D/2} dx \left\{ (q_{n,o} \operatorname{sgn}(z-z') - k_n h'(x)) H_m - iL_m \right\} \\ - H_{n,o}^{\text{diff}} e^{iq_{n,o}z} \quad \text{for } z < d_0 + h(x) \quad (73a)$$

$$x e^{iq_{n,o}|z-z'|} e^{-i(k_n - k_m)x} = \\ |H_o^{\text{inc}}| e^{iq_o z} \quad \text{for } z > d_0 + h(x) , \quad (73b)$$

where  $z'$  is to be evaluated on the surface  $[d_0 + h(x)]$ . The modulus sign is dropped from subsequent development, but the amplitude of  $H_o^{\text{inc}}$  is assumed.

Generally, integration of the Green's function is made more difficult because of the modulus sign appearing in the exponent. Although the source point  $z'$  lies on the surface, the observation point  $z$  may be chosen so not to penetrate the selvage region. In this case, simpler equations are obtained. Thus, for observation in the upper region, we let  $z < \min h(x)$ ; for the lower region,  $z > \max h(x)$ .

If the observation point  $z$  lies in the substrate outside the selvage region, then  $z-z'$  points down in the  $+z$  direction. Evaluation of Equation (73b) is now carried out with  $\operatorname{sgn}(z-z') = +1$ , and integrating the term

$$\int_{-D/2}^{D/2} dx h'(x) H_m e^{-iq_{n,o}h(x)} e^{i(k_m - k_n)x} \quad (74)$$

by parts results in

$$\begin{aligned} & \frac{e^{-iq_{n,o}d_0}}{2q_{n,o}D} \sum_{m=-\infty}^{\infty} \int_{-D/2}^{D/2} \left( \frac{\epsilon_0 \left( \frac{\omega}{c} \right)^2 - k_n k_m}{q_{n,o}} \right) H_m - iL_m \left( e^{-iq_{n,o}h(x)} e^{i(k_m - k_n)x} \right) dx \\ & = H_o^{\text{inc}} \quad \text{for } z > d_0 + h(x) \end{aligned} \quad (75)$$

For an observation point in the upper region,  $z-z'$  points upward and  $\text{sgn}(z-z') = -1$ . Integrating Equation (73a) by parts results in

$$\begin{aligned} & \frac{e^{+iq_{n,o}d_0}}{2q_{n,o}D} \sum_{m=-\infty}^{\infty} \int_{-D/2}^{D/2} \left( - \frac{\epsilon_0 \left( \frac{\omega}{c} \right)^2 - k_n k_m}{q_{n,o}} \right) H_m - iL_m \left( e^{+iq_{n,o}h(x)} e^{i(k_m - k_n)x} \right) dx \\ & = H_{n,o}^{\text{diff}} \quad \text{for } z < d_0 + h(x) \end{aligned} \quad (76)$$

Notice that the groove profile enters the analysis within an integral over the grating period; explicit derivatives of the grating profile do not appear. By defining matrix elements  $\phi_{nm,o}^{\pm}$  and  $\eta_{nm,o}^{\pm}$  as

$$\phi_{nm,o}^{\pm} = \frac{1}{D} \int_{-D/2}^{D/2} dx e^{\pm iq_{n,o}h(x)} e^{i(k_m - k_n)x} \quad (77)$$

and

$$\eta_{nm,o}^{\pm} = \left( \frac{\epsilon_0 \left( \frac{\omega}{c} \right)^2 - k_n k_m}{q_{n,o}} \right) \phi_{nm,o}^{\pm} \quad (78)$$

the extinction theorem Equations (75) and (76) can be conveniently written as

$$\begin{aligned} \sum_{m=-\infty}^{\infty} (\eta_{nm,o}^- e^{-iq_{n,o}d_o} H_m - i \phi_{nm,o}^- e^{-iq_{n,o}d_o} L_m) \\ = 2q_{n,o} H_o^{\text{inc}} \quad \text{for } z > d_o + h(x) \end{aligned} \quad (79)$$

and

$$\begin{aligned} \sum_{m=-\infty}^{\infty} (-\eta_{nm,o}^+ e^{+iq_{n,o}d_o} H_m - i \phi_{nm,o}^+ e^{+iq_{n,o}d_o} L_m) \\ = -2q_{n,o} H_{n,o}^{\text{diff}} \quad \text{for } z < d_o + h(x) \end{aligned} \quad (80)$$

In these expressions, the  $\exp(iq_{n,o}d_o)$  term is unity, since the mean interface surface level is defined as  $d_o = 0$ .

The extinction theorem Equation (63) for the substrate region is now considered in a manner analogous to the derivation carried out for the upper region. This results in

$$\begin{aligned} \sum_{m=-\infty}^{\infty} \left( -\eta_{nm,s}^+ e^{+iq_{n,o}d_o} H_m - i \frac{\epsilon_s}{\epsilon_o} \phi_{nm,s}^+ e^{+iq_{n,o}d_o} L_m \right) \\ = 0 \quad \text{for } z < d_o + h(x) \end{aligned} \quad (81)$$

and

$$\begin{aligned}
& \sum_{m=-\infty}^{\infty} \left( \eta_{nm,s}^- e^{-iq_{n,o}d_o} H_m - i \frac{\epsilon_s}{\epsilon_o} \phi_{nm,s}^- e^{-iq_{n,o}d_o} L_m \right) \\
& = -2q_{n,s} H_{n,s}^{\text{trans}} \quad \text{for } z > d_o + h(x)
\end{aligned} \tag{82}$$

In these expressions, the subscript  $s$  (signifying the substrate region) has been substituted in place of subscript  $0$  for the incident medium.

### REFLECTION COEFFICIENT MATRIX

Equations (79) through (82) represent linear equation systems with unknowns  $H_m$ ,  $L_m$ ,  $H_{n,o}^{\text{diff}}$ , and  $H_{n,s}^{\text{trans}}$ . This type of problem is usually solved numerically by truncating the system of equations such that  $|n| \leq N$  and  $|m| \leq N$ . When this is done, each equation (79) through (82) yields a  $2N + 1$  equation system and unknowns  $H_m$  and  $L_m$ . In addition, the  $H_{n,o}^{\text{diff}}$  and  $H_{n,s}^{\text{trans}}$  are unknown quantities. In matrix notation, Equations (79) and (80) can be written as

$$\eta_o^- H - i \phi_o^- L = 2q_o H_o^{\text{inc}} \tag{83}$$

and

$$+\eta_o^+ H + i \phi_o^+ L = 2q_o H_o^{\text{diff}}, \tag{84}$$

where, after truncation,  $\phi_o^\pm$  and  $\eta_o^\pm$  are square matrices of dimension  $2N + 1$  with elements  $\phi_o^\pm = [\phi_{nm,o}^\pm]$  and  $\eta_o^\pm = [\eta_{nm,o}^\pm]$ . The integers  $n$  and  $m$  range from  $-N$  to  $N$  and designate the rows and columns, respectively, of the  $\phi_o$  and  $\eta_o$  matrices.  $H$  and  $L$  are column vectors of size  $2N + 1$  with elements  $H_m$  and

$L_m$ , and  $H_o^{inc}$  is a column vector with all zeros except the central terms. The square matrix  $q_o$  is of size  $2N + 1$ , which is diagonal. That is,  $q_o = \text{dia}[q_{n,o}]$ , where  $q_{n,o}^2 = \epsilon_o(\omega/c)^2 - k_n^2$ .  $H_o^{diff}$  is a  $2N + 1$  column vector representing the unknown diffracted magnetic field. Similarly, with the matrix definitions discussed above, Equations (81) and (82) become

$$-\eta_s^+ H - i \frac{\epsilon_s}{\epsilon_o} \phi_s^+ L = 0 \quad (85)$$

and

$$\eta_s^- H - i \frac{\epsilon_s}{\epsilon_o} \phi_s^- L = -2q_s H_s^{trans} \quad (86)$$

The system of equations represented by Equations (83) through (86) may be solved for the unknown quantities  $H_o^{diff}$  by first solving Equation (85) for  $L$  in terms of  $H$ , yielding

$$L = i \frac{\epsilon_o}{\epsilon_s} (\phi_s^+)^{-1} \eta_s^+ H \quad (87)$$

Substituting this equation into Equations (83) and (84) determines the reflection coefficient matrix  $\rho$  in the form  $H_o^{diff} = \rho H_o^{inc}$ . Thus, the following relationship is obtained:

$$q_{n,o} H_o^{diff} = \left[ +\eta_o^+ - \frac{\epsilon_o}{\epsilon_j} \phi_o^+ (\phi_j^+)^{-1} \eta_j^+ \right] \left[ \eta_o^- + \frac{\epsilon_o}{\epsilon_j} \phi_o^- (\phi_j^+)^{-1} \eta_j^+ \right]^{-1} q_o H_o^{inc} \quad (88)$$

For a planar boundary, the above expression reduces to the standard Fresnel reflection coefficient for TM-polarized light

$$\rho = \frac{H_o^{\text{diff}}}{H_o^{\text{inc}}} = \frac{\frac{-\epsilon_o}{q_o} + \frac{\epsilon_j}{q_j}}{\frac{\epsilon_o}{q_o} + \frac{\epsilon_j}{q_j}} \quad . \quad (89)$$

### TE POLARIZATION

In the case of TE polarization, the electric field is now normal to the plane of incidence and the boundary condition Equation (59) implies the continuity of the normal derivative of the electric field across the interface. The wave function  $U$  in Green's theorem now designates the electric field, and the inhomogeneous Helmholtz equation is utilized in solving Green's identity for the incident medium. The results derived in the section above for TM polarization become valid for TE polarization, provided the following substitution is made:

$$\frac{\epsilon_j}{\epsilon_{j-1}} \rightarrow 1 \quad . \quad (90)$$

## Chapter 5

### EXTINCTION THEOREM ANALYSIS FOR MULTILAYER STRUCTURES

#### INTRODUCTION

The extinction method technique reviewed in the previous chapter is extended in this chapter to analyze diffraction of light from multilayer structures. Figure 5 illustrates the geometry that will be considered. As in the previous section, the coordinate system is chosen such that the plane of incidence is parallel to the  $x,z$  plane and the  $z$ -axis points downward. The film layers are numbered from  $j = 1$  to  $j = J$ . The refractive index of the  $j$ th layer is referred to as  $n_j$ , which may be complex. The grating profile is given by  $z_j = d_j + h(x)$ , where  $d_j$  is the mean level of the  $j$ th layer and  $h(x)$  is the height profile function. As shown in Figure 5,  $h(x)$  is assumed to be the same for each interface. However, in a numerical analysis given later in this paper, the  $h(x)$  is taken to be generally different for each interface. In the equations developed in this chapter, the  $j$  index in parentheses refers to a specific *interface* at which the fields are evaluated. Furthermore, the  $j$  and  $j-1$  subscripts on the fields  $E$  and  $H$  refer to a specific *layer*.

To begin the analysis, the extinction theorem is applied to an arbitrary layer bounded by its bottom and top interfaces. Also, the boundary conditions across the bounding interfaces are applied. In order to develop a propagation scheme through the multilayer, the fields are initialized in the substrate. The fields are then transferred to the top surface by two methods:



(1) repeated multiplication or (2) recursion of the propagation matrices. Once the fields at the top interface have been determined, the diffracted field can be calculated by using the appropriate extinction theorem equation for the incident medium.

The two methods for propagating the magnetic and electric fields from the substrate to the top surface of the multilayer are outlined as follows. In the first method, the traditional characteristic matrix formalism is employed. The characteristic matrix for the  $j$ th layer  $M_j$  relates the tangential components of the electric  $E_j$  and magnetic  $H_j$  fields at the  $j$ th boundary to the fields at the  $j-1$  boundary  $E(j-1)$ ,  $H(j-1)$  by the following expression:

$$\begin{pmatrix} E(j-1) \\ H(j-1) \end{pmatrix} = M_j \begin{pmatrix} E(j) \\ H(j) \end{pmatrix} \quad (91)$$

The characteristic matrix for an assembly of  $J$ -layers is the product (beginning at the layer next to the substrate) of the individual layer matrices. The electric and magnetic fields at the substrate  $E_s$ ,  $H_s$  are then related to the fields at the superstrate  $E_0$ ,  $H_0$  by Equation (19). Details of the characteristic matrix technique were reviewed in Chapter 3.

For the R-matrix technique, Equation (91) can be rewritten as

$$\begin{pmatrix} H(j) \\ H(j-1) \end{pmatrix} = R_j \begin{pmatrix} H'(j) \\ H'(j-1) \end{pmatrix}, \quad (92)$$

where the prime denotes differentiation with respect to the interface normal.  $H'$  is related to the electric field, and  $R$  is the R-matrix for the  $j$ th layer. The R-matrix for the  $j-1$  layer  $R_{j-1}$  is generated from  $R_j$  by a recursion relation. By using this recursive scheme, the R-matrix is propagated from

the substrate to the superstrate, where the diffracted field can be calculated by using the appropriate extinction theorem equation for the incident medium. The essential difference between the characteristic matrix and the R-matrix propagation schemes are illustrated by Equations (91) and (92). In the characteristic matrix technique, the electric and magnetic fields at one interface are related to the fields at a lower interface by a propagation matrix. On the other hand, the R-matrix relates the magnetic field at two interfaces to the electric fields at those same interfaces.

It was found that the characteristic matrix approach frequently resulted in ill-conditioned matrices when guided waves were present, leading sometimes to numerical difficulties. These problems were avoided by incorporating an R-matrix or recursive method of generating a propagation matrix.<sup>81,82</sup> This approach leads to much better numerical stability and correspondingly improved algorithms. The greater numerical stability of the R-matrix technique results from the stability associated with the matrix elements.<sup>83</sup> For an evanescent state and planar boundaries, the characteristic matrix elements are hyperbolic functions,  $\sinh$  and  $\cosh$ ; whereas, the R-matrix elements are  $\coth$  and  $\operatorname{csch}$ . For large arguments, the  $\coth$  and  $\operatorname{csch}$  are well behaved; whereas, the  $\sinh$  and  $\cosh$  that arise in the characteristic matrix formulation increase exponentially. Thus, the R-matrix scheme is numerically stable and retains precision when evanescent waves corresponding to large arguments are present. However, for small arguments of the hyperbolic functions, the stability situation is reversed.

## EXTINCTION THEOREM: jTH LAYER

Extinction theorem equations for layer  $j$  are derived by employing the Green's identity to the volume enclosing the  $j$ th layer, bounded by the interfaces  $j$  and  $j-1$ . This results in an integration along the closed path ABCD as shown in Figure 5. Since the integration from A to B will cancel that of C to D, the integrals along the  $j$  and  $j-1$  surfaces only need be considered.

For both the lower and upper surfaces, two integral equations are developed for which the fields are extinguished. One equation determines the field relations for a point of observation below and outside the volume enclosing the  $j$ th layer, and the second incorporates the observation direction upward and again outside the volume of integration.

The extinction relation for the  $j$ th layer region developed by using Green's theorem along the bottom and top surfaces for field observation in the  $+z$  direction is

$$\begin{aligned} & \sum_{m=-\infty}^{\infty} \left\{ \eta_{nm,j}^- e^{-iq_{n,j}d(j)} H_{m,j}(j) - i\phi_{nm,j}^- e^{-iq_{n,j}d(j)} L_{m,j}(j) \right\} \\ & - \sum_{m=-\infty}^{\infty} \left\{ \eta_{nm,j}^- e^{-iq_{n,j}d(j-1)} H_{m,j-1}(j-1) \right. \\ & \quad \left. - i\phi_{nm,j}^- \frac{\epsilon_j}{\epsilon_{j-1}} e^{-iq_{n,j}d(j-1)} L_{m,j-1}(j-1) \right\} = 0, \end{aligned} \quad (93)$$

where  $q_{n,j}$  is the wave-vector component in the  $z$ -direction given by

$$q_{n,j} = \left[ \epsilon_j \left( \frac{\omega}{c} \right)^2 - k_o^2 \right]^{1/2} . \quad (94)$$

Equation (93) is seen easily by considering the development of Green's identity in the last chapter that led to Equations (79) through (82). As already mentioned, the evaluation of Green's identity within layer-j involves the integration along the lower (j) and upper (j-1) surfaces of the layer. Evaluation of Green's identity along the lower interface results in the left side of Equation (79) (where the subscript o is set = j). Similarly, the left side of Equation (82) (where o = j-1 and s = j) results from the evaluation of the surface integral along the upper surface. Equation (93) thus represents the surface integration appearing in Green's identity along the lower and upper boundaries.

An expression similar to Equation (101) results for the jth region by taking the observation point in the -z direction, i.e.,

$$\begin{aligned} & \sum_{m=-\infty}^{\infty} \left\{ -\eta_{nm,j}^+ e^{+iq_{n,j}d(j)} H_{m,j}(j) - i\phi_{nm,j}^+ e^{+iq_{n,j}d(j)} L_{m,j}(j) \right\} \\ & - \sum_{m=-\infty}^{\infty} \left\{ -\eta_{nm,j}^+ e^{+iq_{n,j}d(j-1)} H_{m,j-1}(j-1) \right. \\ & \left. - i \frac{\epsilon_j}{\epsilon_{j-1}} \phi_{nm,j}^+ e^{+iq_{n,j}d(j-1)} L_{m,j-1}(j-1) \right\} = 0 \end{aligned} \quad (95)$$

This equation follows from Equations (80) (where o = j) and (81) (where o = j-1 and s = j). The left side of Equation (80) results from the integration along

the lower surface and the left side of Equation (81) from integration along the upper interface.

The extinction theorem expressions are now rearranged in the form of a propagation matrix by which the fields in the substrate may be transferred to the top surface. This effectively reduces the multilayer problem to one of a single interface in terms of equivalent fields at the top surface. Once the fields at the top surface are known, the diffracted field in air is determined by use of the extinction theorem relation for the incident medium.

Combining Equations (93) and (95) in the form of a matrix expression results in

$$\begin{pmatrix} e^{-iq_{nj}d(j)} & 0 \\ 0 & e^{+iq_{nj}d(j)} \end{pmatrix} \begin{pmatrix} \eta_j^- & -i\phi_j^- \\ -\eta_j^+ & -i\phi_j^+ \end{pmatrix} \begin{pmatrix} H(j) \\ L(j) \end{pmatrix} - \begin{pmatrix} e^{-iq_{nj}d(j-1)} & 0 \\ 0 & e^{+iq_{nj}d(j-1)} \end{pmatrix} \begin{pmatrix} \eta_j^- & -i\frac{\epsilon_j}{\epsilon_{j-1}}\phi_j^- \\ -\eta_j^+ & -i\frac{\epsilon_j}{\epsilon_{j-1}}\phi_j^+ \end{pmatrix} \begin{pmatrix} H(j-1) \\ L(j-1) \end{pmatrix} = 0 \quad (96)$$

This is the primary equation for the analysis of diffracted fields from multilayer, periodic-modulated, thin-film layer and relates the magnetic and electric fields at the boundary surfaces by means of the layer and surface roughness characteristics.

### CHARACTERISTIC MATRIX PROPAGATION

Even though the R-matrix propagation scheme resulted in greater numerical stability, the characteristic matrix technique is considered in this section. This is because the characteristic matrix technique leads to a more intuitive notion of field propagation through each consecutive thin-film layer. Equation (96) is rewritten in matrix notation as

$$\psi(j-1) = \bar{Q}_j^{-1} \theta_j Q_j \psi(j) , \quad (97)$$

where  $\theta_j$  is a square matrix that is diagonal and has the form

$$\theta_j = \begin{pmatrix} e^{iq_{nj}(d_{j-1}-d_j)} & 0 \\ 0 & e^{-iq_{nj}(d_{j-1}-d_j)} \end{pmatrix} , \quad (98)$$

where the off-diagonal zeros represent null matrices and the diagonal terms are diagonal matrices with elements  $\delta_{m,n} e^{\pm iq_{n,j}(d_{j-1} - d_j)}$ .  $Q_j$  and  $\bar{Q}_j$  are square matrices of the form

$$Q_j = \begin{pmatrix} \eta_j^- & -i\phi_j^- \\ -\eta_j^+ & -i\phi_j^+ \end{pmatrix} \quad (99)$$

and

$$\bar{Q}_j = \begin{pmatrix} \eta_j^- & -i \frac{\epsilon_j}{\epsilon_{j-1}} \phi_j^- \\ -\eta_j^+ & -i \frac{\epsilon_j}{\epsilon_{j-1}} \phi_j^+ \end{pmatrix} . \quad (100)$$

The  $\psi(j-1)$  and  $\psi(j)$  are column vectors given by

$$\psi(j-1) = \begin{pmatrix} H(j-1) \\ L(j-1) \end{pmatrix} \quad (101)$$

and

$$\psi(j) = \begin{pmatrix} H(j) \\ L(j) \end{pmatrix}, \quad (102)$$

where  $H(j)$ ,  $H(j-1)$ ,  $L(j)$ , and  $L(j)$  are also column vectors.

Equation (97) is in the form of a propagation matrix  $P_j$ , where

$$P_j = \bar{Q}_j^{-1} \theta_j Q_j. \quad (103)$$

This matrix propagates the fields from the  $j$ th interface (evaluated on the negative or upper side) to the positive side of its  $j-1$  interface. Because the boundary conditions have been applied to the  $Q_j$  matrix, the fields are continuous across the  $j-1$  interface. For a multilayer structure of  $J$  layers, the overall propagation is determined by multiplication of the individual layer propagation matrices beginning at the substrate, i.e.,

$$P = \left\{ \prod_{j=J}^1 \bar{Q}_j^{-1} \theta_j Q_j \right\}. \quad (104)$$

In the propagation scheme given by the above equation, the boundary conditions are repeatedly applied to the top surface of each layer of the multilayer structure. Thus, the fields are propagated through each layer and across the top interface into the adjacent layer, which effectively allows

computation of the field at the top surface of the multilayer stack in terms of the fields at the substrate boundary.

#### EXTINCTION THEOREM: SUBSTRATE INITIALIZATION

In the propagation scheme given by Equation (97), the fields are initialized in the substrate region. This is accomplished by solving Equation (85) in terms of  $L(J)$ :

$$L(J) = i(\phi_s^+)^{-1} \eta_s^+ \frac{\epsilon_J}{\epsilon_s} H(J) \quad (105)$$

Combining Equations (97), (101), (102), (104), and (105) results in

$$\begin{pmatrix} H(o) \\ L(o) \end{pmatrix} = \begin{pmatrix} P_{11} & P_{12} \\ P_{21} & P_{22} \end{pmatrix} \begin{pmatrix} H(J) \\ i(\phi_s^+)^{-1} \eta_s^+ \frac{\epsilon_J}{\epsilon_s} H(J) \end{pmatrix}, \quad (106)$$

where  $P_{ij}$  are square submatrices of the propagator  $P$  of order  $2N + 1$ .

#### EXTINCTION THEOREM: INCIDENT MEDIUM

Use of the extinction theorem at the top surface follows directly from the single-surface analysis presented in the previous chapter. A reflection coefficient expressed in terms of the  $H$  and  $L$  fields at the top surface is now developed. The final result is found by propagating the fields at the substrate boundary to the top surface. This determines a relation of the fields in terms



of the propagation matrix that is then substituted into the reflection coefficient expression.

The unknown diffracted field  $H_o^{\text{diff}}$  is found by substituting the fields at the surface of the multilayer [given by  $H(o)$  and  $L(o)$  from Equation (106) into Equations (83) and (84)], thus giving

$$q_o H_o^{\text{diff}} = [\eta_o^+ (P_{11} + P_{12}\Lambda) + i\phi_o^+ (P_{21} + P_{22}\Lambda)] \times [\eta_o^- (P_{11} + P_{12}\Lambda) - i\phi_o^- (P_{21} + P_{22}\Lambda)]^{-1} q_o H_o^{\text{inc}} \quad (107)$$

where  $\Lambda$  is the  $2N + 1$  square matrix given by

$$\Lambda = i(\phi_s^+)^{-1} \eta_s^+ \frac{\epsilon_j}{\epsilon_s}$$

#### EXTINCTION THEOREM: R-MATRIX PROPAGATION

Consistent with utilizing the R-matrix propagation scheme Equation (92), the extinction theorem relation for the  $j$ th layer Equation (96) is now cast in the form of the R-matrix relation, resulting in

$$\begin{aligned}
\begin{pmatrix} H(j) \\ H(j-1) \end{pmatrix} &= \begin{pmatrix} \zeta_j^+ & \eta_j^- & -\eta_j^- \\ -\zeta_j^- & \eta_j^+ & +\eta_j^+ \end{pmatrix}^{-1} \begin{pmatrix} \zeta_j^+ i \phi_j^- & -i \frac{\epsilon_j}{\epsilon_{j-1}} \phi_j^- \\ \zeta_j^- i \phi_j^+ & -i \frac{\epsilon_j}{\epsilon_{j-1}} \phi_j^+ \end{pmatrix} \begin{pmatrix} L(j) \\ L(j-1) \end{pmatrix} \\
&= \begin{pmatrix} r_{11} & r_{12} \\ r_{21} & r_{22} \end{pmatrix} \begin{pmatrix} L(j) \\ L(j-1) \end{pmatrix}
\end{aligned} \tag{108}$$

where the electric field has been substituted for the derivative of the magnetic field.  $R_j$  is the sector matrix for the  $j$ th layer and is written as square submatrices  $r_{mn}$ :

$$R_j = \begin{pmatrix} r_{11} & r_{12} \\ r_{21} & r_{22} \end{pmatrix} . \tag{109}$$

The  $\zeta_j^\pm$  is also a square matrix, which is diagonal and has elements

$$(\zeta_j^\pm)_{m,n} = \delta_{m,n} \exp[\pm q_{n,j}(d(j-1) - d(j))] , \tag{110}$$

where  $\delta_{m,n}$  is the Kronecker  $\delta$ -function.

Propagation of the fields through the multilayer is accomplished by developing a recursive scheme. At each step of the recursion, a global R-matrix  $R$  is formed by combining a new sector matrix with the previous global R-matrix. The global R-matrix is developed by assuming that the magnetic field is related to the electric field in the following manner:

$$H(j) = R(j)L(j) \quad (111)$$

$$H(j-1) = R(j-1)L(j-1) \quad (112)$$

Combining Equations (108), (109), (111), and (112) determines the global R-matrix recursion,

$$R(j-1) = r_{12} [R(j) - r_{22}]^{-1} r_{21} + r_{11} \quad (113)$$

This equation propagates the fields from the  $j$ th to the  $j-1$  boundary. In the propagation scheme given above, the boundary conditions are repeatedly applied to the top surface of each layer of the multilayer structure. Thus, the fields are propagated through each layer and across the top interface into the adjacent layer, which again effectively allows computation of the field at the top surface of the multilayer stack in terms of the fields at the substrate boundary.

The R-matrix recursion equation is initiated in the substrate by the following:

$$R_{(s)} = -i \frac{\epsilon_s}{\epsilon_j} (\eta_s^+)^{-1} \phi_s^+ \quad (114)$$

which is derived directly from the extinction theorem relation for the substrate region.

Beginning with  $R_{(s)}$ , a recursive global matrix is generated from Equations (109) and (113) by assembling the previous global matrix with the sector R-matrix. By repeated use of Equation (113), the magnetic and electric

fields are transferred to the top surface of the multilayer assembly. A further discussion of the R-matrix technique can be found in Reference 83.

Once the final global R-matrix  $R(o)$  has been determined from Equation (113), the diffracted field can be found from the extinction theorem Equations (83) and (84) for the incident medium, which can be written in matrix notation as

$$\begin{pmatrix} \eta_o^- & -i\phi_o^- \\ +\eta_o^+ & +i\phi_o^+ \end{pmatrix} \begin{pmatrix} H(o) \\ L(o) \end{pmatrix} = \begin{pmatrix} 2q_o H(o)^{inc} \\ 2q_o H(o)^{diff} \end{pmatrix} . \quad (115)$$

By using the above equation and the following relation,

$$H(o) = R(o) L(o) , \quad (116)$$

the diffractive field can be solved for, resulting in

$$q_o H(o)^{diff} = [+ \eta_o^+ R(o) + i\phi_o^+] [\eta_o^- R(o) - i\phi_o^-]^{-1} q_o H(o)^{inc} . \quad (117)$$

### CONCLUSIONS

To solve Equation (107) or (117), note that  $H_o^{inc}$  is a column vector, which is null everywhere except the central element. This nonzero element is  $I$ , the incident beam intensity. Notice that solutions to Equation (117) are inversely proportional to the determinant of the matrix  $M = [\eta_o^- R(o) - i\phi_o^-]$ . If the incident intensity is zero, the boundary conditions can be satisfied only if the determinant of  $M$  ( $\det M$ ) vanishes. This provides the dispersion

relations or allowable wave vectors for guided modes that can be supported by the multilayer stack. Solutions to the homogeneous equation corresponding to Equation (117) do not always exist, however. For cases where the incident medium is air, there cannot be direct coupling between an incident beam and a guided wave. This is because the wave vectors parallel to the surface of the incident beam  $k_0$  and guided wave  $k_{gw}$  are  $k_0 = (\omega/c)\sin\theta_0 < (\omega/c)$  and  $k_{gw} > (\omega/c)$ . Thus, phase matching cannot occur. When a grating profile is introduced at the multilayer interfaces, a resonant condition exists when  $\det M$  passes through a minimum and the guided wave becomes a leaky wave.

We have compared numerical results utilizing the extinction theorem to results derived from other calculational techniques. The extinction theorem calculation for a dielectric waveguide is compared in Figure 6 to the results given by Chandezon *et al.*<sup>84</sup> utilizing their differential method. Excellent agreement was attained. Also, extinction theorem calculations at resonance agreed with those of a Rayleigh-Fourier method<sup>3</sup> for multilayer-coated gratings as well as those of the Maystre 'Omega Code'<sup>8</sup> for a nine-layer-coated metallic grating.<sup>85</sup> Additional comparisons were made with both experimental and theoretical data, and good agreement was attained.<sup>53,86-88</sup>

It was found that the characteristic matrix approach frequently resulted in ill-conditioned matrices, which sometimes led to numerical difficulties. These problems were avoided by incorporating an R-matrix method of generating a propagation matrix. This approach led to much better numerical stability and a correspondingly improved algorithm. The

numerical analysis performed and reported in the following chapter utilized the R-matrix propagation scheme.

## Chapter 6

### NUMERICAL RESULTS

#### INTRODUCTION

This chapter presents numerical results on resonance effects on single- and multilayer-overcoated gratings. Because of the experimental difficulty of exploring the effects of various parameters such as grating profile and coating design, a calculational approach was employed to examine the influence of various parameters on diffraction efficiency at resonance.

Although it was not the purpose of this research to perform a numerical analysis of various calculational techniques, both the characteristic matrix and R-matrix methods were programmed. The core of each program was the same; only the propagation method differed. It was found that the R-matrix propagation scheme led to much better numerical stability and a corresponding improved algorithm over the traditional characteristic matrix method. This was determined in two ways. First, as the groove depth ( $h$ ) of the surface profile was increased, the energy balance became  $>1$  for the characteristic matrix method when  $h/\lambda \sim 0.1$ ; whereas, this occurred at  $h/\lambda \sim 1.0$  for the R-matrix method. Second, computer subroutines were used to solve linear equation systems of the form  $Ax = B$  and to estimate the condition of  $A$ . The condition of the equation system is a quantity that measures the sensitivity of the solution  $x$  to round off errors in  $A$  and  $B$ . Thus, it is an estimate of the accuracy of which the elements of  $x$  can be computed. When

the exponent of the condition value approaches the precision of the computer, the computed results may be suspect. For a nine-layer-overcoated grating problem, the condition of the characteristic propagation matrix was on the order of  $10^{23}$ ; whereas, the R-matrix calculation algorithm had a condition of  $10^3$ , indicating vastly improved numerical precision.

Using the extinction theorem equations and the R-matrix propagation scheme, diffraction efficiencies for single- and multilayer-overcoated gratings were calculated. Both TE- and TM-polarized light were considered at a 0.6328- $\mu\text{m}$  wavelength. The grating period was 0.7  $\mu\text{m}$ ; thus, for the angles of incidence considered here, only a -1 diffracted order (other than the specular) was present in air. Numerical results show diffraction efficiencies at resonance for the -2, -1, 0, +1, +2 order as functions of the incident angle. Many of the numerical analysis results that follow share the same substrate profile shape, which is shown in Figure 7(a). Sinusoidal and rectangular shapes were investigated also. The grating grooves are perpendicular to the plane of incidence.

Anomalous resonance effects were investigated for both replication and nonreplication of groove profile at the interfaces between layers. For the case of perfect replication, the substrate profile shape was assumed at each film interface. For cases of nonreplication, a rounding of the trapezoidal shape was assumed, as illustrated in Figure 7(b), where the profile was rounded to a greater extent at each film interface above the substrate. A reduction in groove depth also was investigated for some of the nonreplication cases. Most of the calculations were carried out to the 7th



order on the Naval Weapons Center's VAX facility and the Naval Research Laboratory's CRAY.

This chapter is divided into four sections that deal with (1) resonance effects associated with a single-dielectric layer upon a dielectric substrate (TE polarization) as well as the effect of groove shape, groove depth, and nonreplication on resonance; (2) single-dielectric layer upon a metallic substrate (TE polarization); (3) effects of nonreplication through multilayers for TE polarization; and (4) effects of nonreplications for a multilayer high-index (H) and low-index (L) pair upon a metallic substrate (TM polarization).

Waveguide modes for each of the four cases considered were found by using the graphical technique outlined in Chapter 3, where the phase shifts for the upward- ( $\phi_-$ ) and downward- ( $\phi_+$ ) traveling waves within the film assembly are calculated and plotted. The allowed guided-wave modes are determined by the intersection points of the phase curves, which are solutions of the equation  $\phi_+ + \phi_- = m2\pi$ , as shown in Figures 8(a) through (f). These points indicate the propagating angle  $\theta_{gw}$  of the guided wave within the top layer of the assembly. Shown in Table 1 are the normalized wave modes and the phase-matching angles of incidence calculated from the grating equation for the cases investigated.

TABLE 1. Normalized Guided-Wave Numbers  $k_{gw}$  and Mode Coupling Angles  $\theta_o$  ( $k_{gw} = n_1 \sin \theta$ ;  $n_1 = 2.26$ ).

Design	Mode	$\theta_{gw}$ , deg.	$k_{gw}$	m=1 $\theta_o$ , deg	m=2 $\theta_o$ , deg	m=3 $\theta_o$ , deg
H/L $t_h=0.25 \mu$ TE	0	43.5	1.556	40.7	-14.6	proh
	1	67.4	2.086	proh	-16.1	-38.8
H/Ag $t_h=0.3 \mu$ TE	0	43.0	1.541	39.6	-15.5	proh
	1	68.0	2.095	proh	-16.7	-38.1
HL/Ag TE	0	45.2	1.604	44.4	-11.8	proh
(HL) <sup>2</sup> /Ag TE	0	41.5	1.498	36.4	-18.1	proh
	1	52.0	1.781	61.3	-1.5	-68.6
(HL) <sup>4</sup> /Ag TE	0	37.3	1.370	27.8	-26.0	proh
	1	44.0	1.570	41.8	-13.8	proh
	2	50.0	1.731	55.8	-4.4	-78.8
	3	54.2	1.833	68.3	1.4	-61.5
(HL) <sup>2</sup> /Ag TM	0	35.0	1.296	23.1	-30.1	proh
	1	49.0	1.706	53.3	-5.9	proh
	2	63.5	2.023	proh	12.4	-43.6

#### SINGLE-DIELECTRIC LAYER UPON A DIELECTRIC SUBSTRATE: TE POLARIZATION

Considered is a 0.25- $\mu$ m-thick, thin-film layer of dielectric constant  $\epsilon_1 = (5.11, 0.0)$  upon a semi-infinite substrate of dielectric constant  $\epsilon_s = (2.25, 0.0)$ . The diffraction efficiencies for the 0, -1, and +1 orders for the H/L-coated grating are plotted in Figure 9 near the resonant angle of 40.5°. The groove shape is trapezoidal. The incident beam couples into the 0th guided-wave mode at the film surface. Notice that the guided-wave resonance causes rapid

variation in the specular reflectance [Figure 9(b)]. The variation in the -1 order intensity increases from 0.0003 to 0.1. Figure 9(c) clearly shows the resonance associated with the +1 order, which is evanescent in the air and substrate regions but is propagating in the thin-film layer.

The influence of groove depth on the diffraction efficiencies at resonance is considered in Figures 10 and 11. Figure 10 shows the 0, 1, and +1 intensities at resonance when the trapezoidal groove depth is increased ten times to  $0.1\text{ }\mu\text{m}$ . The sharp resonant features are broadened because of the increased damping. The +1 order coupling into the guided wave is lower by two orders of magnitude in this case from that seen in Figure 9. The -1 intensity has increased; however, it no longer displays a sharp resonant structure.

The resonant response when the groove depth is decreased from  $0.01$  to  $0.001\text{ }\mu\text{m}$  is shown in Figure 11. At resonance, the intensities for the 0, -1, and +1 orders are lower; however, they are narrower than was seen for the  $0.01\text{-}\mu\text{m}$ -groove-depth case.

Figures 12 through 15 examine the influence of the duty cycle of a rectangular grating on diffraction efficiencies. The duty cycle is defined as the ratio of the length of the raised position of the profile to the period. Furthermore, since the height parameter  $L$  is equivalent to  $-L$  in the theoretical treatment, a 90% duty cycle is identical to a 10% duty cycle, for example. It is interesting to note that as the duty cycle decreases from 90 to 50%, the intensity in the +1 guided wave increases. Also, the resonant coupling in the specular reflected beam increases and attains a maximum for the 50% duty cycle case. Also, note that the intensity in the -1 diffracted

order for a 50% duty cycle dips at the resonant angle below the off-resonance intensity level. As the duty cycle increases from 50%, the -1 order efficiency also increases.

In the case of the 50% duty cycle rectangular profile, the Fourier coefficients are similar to that of the trapezoidal profile in that they fall off with increasing order. However, comparison of Figures 9 and 13 indicates that the behavior is different. As reported in Reference 3, the cause for such a difference lies in the fact that for the 50% duty cycle rectangular profile the coupling matrix elements given by Equations (83) and (84) are reduced for even combinations of  $n-m$ . In other words, the grating only allows changes of  $\pm 1, 3, 5$ , etc. to the wave vector parallel to the surface. For the case considered in this section, the incident beam is coupled via the +1 diffraction order into a guided wave. In order for the energy in the guided wave to outcouple into the -1 diffracted order, a -2 order matrix element is needed. Since even orders are greatly reduced, outcoupling does not occur and, instead, the guided wave is transmitted in the case of a transparent substrate or absorbed for a metallic substrate.

Triangular and sinusoidal profile shapes are considered in Figures 16 and 17. For both the triangular and sinusoidal cases, the specular intensity is increased slightly while the resonant intensities in the -1 order are drastically reduced over the trapezoidal profile case, Figure 9. Furthermore, the intensity curves for both the triangular and sinusoidal profiles closely resemble the intensities seen for the 50% duty cycle rectangular profile (Figure 13).

The primary cause of the difference in intensities in the -1 order between the trapezoidal and sinusoidal profiles is the coupling strengths that depend upon Fourier transforms of the grating profile. For a sinusoidal profile, the coupling strengths entail Bessel functions. Coupling of the incident beam via a +1 diffraction order into a guided wave and then outcoupling into the -1 order involves a second-order Bessel function. For a grating whose sinusoidal amplitude is small compared to the wavelength of light, the arguments of the Bessel functions are typically small. It is believed, therefore, that the weak coupling strength is the primary cause of lack of resonant enhancement of the -1 order.

Two extreme cases of nonreplication of the grating profile at the film interfaces for the H/L design are considered in Figures 18 and 19. In Figure 18 can be seen the 0<sup>-</sup>, -1, and +1 intensities at resonance for a trapezoidal grating profile on the substrate only, the top surface being flat. The intensities at resonance are reduced over those shown in Figure 9. Also, the position of the resonance has shifted from 41.5 to 43.25°. Figure 19 shows the case for a trapezoidal profile only on the top surface of the film, while the substrate interface is smooth. Note, that there is a shift in the resonant coupling angle in the direction of smaller angle from 41.5 to 39.5°. Also, note the presence of an additional resonance at 39.3° in the 0, -1, +1 intensity plots. This resonance is caused by the  $m = -3$  coupling into the 4th guided-wave mode and can be explained as follows. The propagation angle of the 4th guided-wave mode is beyond the critical angle for the substrate boundary and for a flat substrate profile is totally reflected. A grating profile on the substrate, however, creates diffracted orders in transmission, thus reducing

the intensity of the guided wave available for outcoupling at the top interface.

#### SINGLE-DIELECTRIC LAYER UPON A METALLIC SUBSTRATE: TE POLARIZATION

In this section, the effects of nonreplication of the trapezoidal grating profile are explored. Alternate groove shapes are not considered. In this case, a single-dielectric layer of dielectric constant  $\epsilon_1 = (5.11, 0.0)$  and a thickness of  $0.30 \mu\text{m}$  is placed upon a semi-infinite silver substrate of  $\epsilon_s = (-16.4, 0.52)$ . The allowed guided-wave modes are indicated in Table 1. Figure 20 plots the diffraction efficiencies at resonance when the trapezoidal profile is replicated at both the top and bottom interfaces. Two resonant situations are present: (1)  $\theta_i = 38.3^\circ$ , representing coupling of the  $m = -3$  diffraction order into the 1st mode and (2)  $\theta_i = 38.7^\circ$ , representing  $m = +1$  coupling into the 0th guided-wave mode. From Figure 20, it is apparent that there can be large differences in the resultant resonant effects of coupling into different guided-wave modes.

In Figure 21, a trapezoidal profile at the substrate is assumed while the top surface is flat. This has the effect of eliminating the 1st mode guided-wave resonance and reducing the zero guided-wave resonance while shifting its position to  $\theta_i = 41.3^\circ$ . The resonant condition for the grating on the top surface only is shown in Figure 22. The angular position of the resonance has moved to  $36.2^\circ$ , and the diffraction intensities are lower than the above case.

An important difference in the shape of the diffraction efficiency curves between the dielectric and metallic substrate cases can be seen by comparing Figures 9 and 20. In the case of the dielectric substrate, the specular efficiency goes through a maximum and minimum near the resonant coupling angle. However, in the case of the metallic substrate, the specular efficiency curve exhibits a dip at resonance. This is most likely due to the absorptive nature of the metal.

#### MULTILAYER DIELECTRIC UPON A METAL SUBSTRATE: TE POLARIZATION

In this section, increasing a high- and low-index layer pair upon a metallic substrate is considered. The substrate is Ag with a dielectric constant  $\epsilon_s = (-16.4, 0.52)$  at  $\lambda = 0.6328 \mu\text{m}$ . The high- and low-index dielectric constants are  $\epsilon_H = (5.11, 0.0)$  and  $\epsilon_L = (2.25, 0.0)$ , respectively, with the low-index layer being adjacent to the Ag substrate. The layer thicknesses are  $\tau_H = 0.0737 \mu\text{m}$  and  $\tau_L = 0.1196 \mu\text{m}$ , which correspond to one-quarter-wave optical thickness at  $\lambda = 0.6328 \mu\text{m}$  and  $45^\circ$  angle of incidence. The substrate profile is assumed to be trapezoidal in this section, and various degrees of nonreplication are considered. A number of guided-wave mode coupling possibilities have been investigated. A wide range of behavior was found in the resonant effects on the -1 order and specular beam among the various coupling possibilities. Several possibilities yielded only minimal effects on the -1 and specular intensities. There are many other possibilities that are unexplored here, and some of these situations may predict strong optical

anomalies. This section concentrates on resonant effects resulting from the  $m = +1$  coupling into the 0th guided-wave mode.

Figures 23 and 24 illustrate the effect of one and two high- and low-index layer pairs on resonant diffraction efficiencies, respectively. In general, increasing the number of layer pairs has the effect of (1) deepening the dip in the specular reflectance and (2) increasing the diffraction efficiency in the -1 order and coupling via the +1 order into the guided wave.

Figure 25 shows numerical results for the design  $(HL)^4/Ag$  with perfect replication of the trapezoidal profile at all interfaces. Figure 26 considers the  $(HL)^4/Ag$  case when the grating profile appears on the top surface only, and Figure 27 shows the resonant behavior when the grating is on the substrate only, all other film interfaces being flat. It can be seen from Figures 26 and 27 that a grating profile on one surface only of a multilayer drastically reduces the resonant behavior. The intensity in the -1 and +1 orders is considerably lower, while the dip in the specular is nearly eliminated.

Figure 28 shows the effect upon resonance for the  $(HL)^4/Ag$  case when the trapezoidal profile is rounded at each interface, as indicated in Figure 7(b); however, it retains the same groove height. The minimum in the specular increases to approximately 0.2 from 0.002, as seen in Figure 25 for perfect replication. Also, the range in the -1 order intensity is reduced from six to five orders of magnitude. The +1 guided-wave intensity appears to have remained about the same. In Figure 29, the trapezoidal profile is again rounded at each interface; however, in addition, the profile height is reduced from  $0.01\ \mu\text{m}$  at the substrate to  $0.002\ \mu\text{m}$  at the top surface in  $0.001\text{-}\mu\text{m}$  steps.



This has the effect of reducing further the resonant coupling. In this case, the specular dips to 0.62 and the -1 intensity peaks at 0.1, as opposed to 0.8 for perfect replication. Again, the +1 guided-wave intensity was not appreciably reduced. Interestingly, the lack of profile replication does not seem to broaden the resonant intensity curves.

#### MULTILAYER DIELECTRIC UPON A METAL SUBSTRATE: TM POLARIZATION

Resonant diffraction efficiency for TM-polarized light is examined in this section. The design considered is  $(HL)^2Ag$ , and the substrate profile is trapezoidal.

Figure 30 shows the intensities in the 0, -1, and +1 orders at resonance for the  $(HL)^2/Ag$  design and TM polarization. The +1 diffractive order is evanescent in air. For the situations investigated, it was found generally that TM polarization results in a weaker resonant condition than TE polarization; this can be seen by comparing the specular intensity from Figure 30 to the corresponding case for TE polarization (Figure 24). Also, the intensities in the -1 are down an order of magnitude for TM polarization over the TE-polarization case. In Figure 31, the trapezoidal profile is rounded at each film interface and reduced in height. Again, this has the effect of lessening the coupling strength at resonance. Other cases have been investigated for TM polarization. Generally, the resonance behavior for TE and TM polarization follows the same trends; however, resonance strengths are weaker for TE polarization.

## Chapter 7

### EXPERIMENTAL VERIFICATION

It has been mentioned that numerical results calculated using the extinction theorem technique compared closely to results derived from other theoretical methods. In this chapter, a comparison is made of theory and experiment of anomalous resonant effects associated with coated low-efficiency gratings.

Calculations and measurements of anomalous diffraction efficiencies were made at  $3.8\text{ }\mu\text{m}$  for a single-dielectric-layer-coated grating. The coating was sapphire ( $\text{Al}_2\text{O}_3$ ) of thickness  $0.164\text{ }\mu\text{m}$  and dielectric constant  $\epsilon = 2.56$ ,  $0.0$ . The grating material was silver ( $\epsilon = -769.84$ ,  $111.1$ ). The grating period was  $4.2\text{ }\mu\text{m}$  with a ruling depth of approximately  $0.1\text{ }\mu\text{m}$ . The groove profile was assumed to be similar to the trapezoidal profile of Figure 7(a).

The coupling angles associated with the guided-wave modes supported by the sapphire layer were determined by the graphical technique described previously. No TE-polarized modes were found. A TM mode for  $m = 1$  diffraction order was determined for a coupling angle of  $6.5^\circ$ . Figure 32 shows the efficiencies in the  $-1$ ,  $0$ , and  $+1$  diffraction orders calculated from the extinction theorem method.

Diffraction efficiency measurements in the  $-1$  order were made on the coated grating at  $3.8\text{ }\mu\text{m}$ . The light source was a deuterium-fluoride laser, operating single line at  $3.8\text{-}\mu\text{m}$  TM polarization with an output power of 30 to

40 mW. The experimental arrangement is shown in Figure 33. The angle of incidence on the grating was chosen by rotating the optical dividing head on which the sample was mounted. A high-Curie-temperature pyroelectric detector was moved by hand and aligned to measure the intensity in either the specular or -1 diffracted beam. To minimize the effect of fluctuations in the laser output power, the intensity in the diffracted beams was normalized to the intensity measured by a reference detector. The diffraction efficiency was then calculated by ratioing this value to the normalized intensity of the incident beam. The incidence angle was varied slowly about the predicted coupling angle to locate resonant angles.

Numerical and experimental results are summarized in Table 2. Close agreement between calculated and experimentally determined resonant angles and efficiencies was attained.

TABLE 2. Numerical and Experimental Results for the Sapphire-Coated Grating ( $\lambda = 3.8 \mu\text{m}$ , TM Polarization,  $m = 1$  Coupling Into the 0th Guided-Wave Mode).

	Incident coupling angle	Efficiency at resonance, -1 order	Off-resonant efficiency, -1 order
Calculated	6.1°	0.30	0.01
Measured	6.5°	0.25	0.02

## Chapter 8

### CONCLUSION

This dissertation concludes with a brief summary of the results attained, followed by suggestions for future work.

### SUMMARY

Observations of anomalous diffraction phenomena were surveyed in Chapter 2. As early as 1902, using a white light source, Wood observed rapid variation in the intensity of diffracted spectral orders from reflection gratings. The first theoretical treatment of Wood's anomalies was given by Rayleigh in 1907. His theory was based upon an expansion of the diffracted field in terms of outgoing plane waves. Rayleigh explained these anomalies as resulting from the redistribution of energy when a diffracted order grazes the surface of the grating. Another type of anomaly evident on bare metallic gratings is associated with surface plasmon excitation. Surface plasmons are transverse-magnetic (TM) evanescent waves. Multilayer dielectric structures can support a wider class of guided waves and may be TM or transverse-electric (TE) polarized.

Resonant phenomena in multilayer-overcoated gratings result from the coupling of the incident light into guided waves within the multilayer assembly. If the propagating angle of the diffracted beam corresponds to a waveguide mode supported by the multilayer, energy flows into the guided

wave, a resonance condition develops, and energy is reradiated into air by subsequent diffraction at the film interfaces.

Chapter 3 presented a method for the calculation of waveguide modes in thin-film multilayer coatings using the characteristic matrix technique. By using the grating equation, it was possible to determine the incident angles by which diffracted light may be coupled into guided waves supported by the multilayer structure.

In this dissertation, an integral method based upon the extinction theorem was used to calculate diffraction efficiencies at resonance from overcoated gratings. The extinction method is based on Green's theorem, which involves the electric or magnetic fields and their derivatives on the diffracting surface.

The extinction theorem technique discussed in Chapter 4 for a single-grating surface was extended in Chapter 5 to analyze the diffracted field for a multilayer structure of periodic roughness. The calculation scheme began by analyzing the fields within an arbitrary layer and employing the extinction theorem at the bottom and top interfaces of that layer with appropriately applied boundary conditions. In order to develop a propagation scheme through the multilayer, the fields are initialized in the substrate. The fields are then transferred to the top surface by (1) repeated multiplication or (2) recursion of the propagation matrices. Once the fields at the top interface have been determined, the diffracted field can be calculated by using the appropriate extinction theorem equation for the incident medium.

It was found that the characteristic matrix approach frequently resulted in ill-conditioned matrices, which sometimes led to numerical difficulties. These problems were avoided by incorporating an R-matrix or recursive method of generating a propagation matrix. This approach leads to greater numerical stability and correspondingly improved algorithms.

By using the extinction theorem equations and the R-matrix propagation scheme, numerical analyses of overcoated gratings were presented in Chapter 6. Both TE- and TM-polarized light were considered at a  $0.6328\text{-}\mu\text{m}$  wavelength. The grating period was  $0.7\text{ }\mu\text{m}$ ; thus, for the angles of incidence considered here, only a -1 diffracted order other than the specular will be present in air. Numerical results showed diffraction efficiencies at resonance for the -1, 0, 1 order as functions of the incident angle. The effect on resonant diffraction due to sinusoidal, rectangular, trapezoidal, and triangular groove profiles as well as nonreplication of the groove profile through the multilayer was examined.

Following is a review of the conclusions reached.

1. In general, increasing the grating amplitude to a certain depth causes an enhancement in resonant effects. This is because the coupling strength increases with groove depth. However, further groove-depth increases do not cause a significant enhancement in resonant effects but, rather, broaden the diffraction efficiency curves caused by damping introduced by the grating.

2. An enhanced diffraction efficiency in the -1 order and a reduction in the specular occur as the duty cycle for a rectangular grating increases

beyond 50%. For a 50% duty cycle grating, the specular is at maximum efficiency and the -1 order dips below the off-resonant intensity.

3. The sinusoidal profile, like the 50% rectangular duty cycle, provided strong coupling into guided-wave modes. However, whereas the trapezoidal profile allowed strong outcoupling into the -1 diffracted order, the sinusoidal profile suppressed such effects.

4. Resonant effects increase with increasing number of high-/low- index pairs.

5. In this dissertation, emphasis was placed on comparing cases of nonreplication of the grating profile to that of perfect replication of the substrate profile at each film interface. A simple rounding of the profile with no reduction in grating amplitude had little effect on the resonant efficiencies. However, only when the groove height was reduced substantially did a significant reduction in resonant effects occur.

#### SUGGESTIONS FOR FUTURE WORK

In many numerical investigations—some not presented here—it was found that coupling into certain waveguide modes led to enhanced resonant intensity in the -1 order; for other modes, little effect was calculated. The reason why some modes produce strong outcoupling and others do not was not investigated in this dissertation; however, it probably depends on the complex phase behavior of the overall coupled system. Many factors such as profile shape, thin-film optical thickness, and guided-wave mode number can affect the phase.

Calculations of the electric-field distribution through the multilayer assembly, although laborious, would provide additional insight concerning the guided-wave phenomena.

A further effort—not covered in this work—would be a perturbative analysis of resonant diffraction from multilayer-coated gratings. This type of analysis may lead to a greater physical interpretation of the influence of the many parameters on resonance effects. A perturbative analysis for a single surface has been used to study the dispersion of plasmons on metallic gratings and reflectivity of a grating. Unfortunately, this method is as complex as the rigorous integral solution, and it is not certain if this type of perturbative analysis can be extended to a multilayer case.<sup>89</sup>

Another possible fruitful area of guided-wave resonant research is binary-coated optics. Improved optical performance of infrared optical systems can be achieved with diffractive optical elements. Developments in the last ten years in pattern generation and deposition and large-scale dry reactive ion-etching techniques have made it feasible to generate binary holographic gratings with blaze-like characteristics.<sup>90</sup> A combination of binary-etched surfaces with multilayer-coated optics in which resonant effects are exploited may lead to improved performance or additional applications of diffractive elements.

It was found that diffraction efficiency calculations utilizing the extinction theorem technique developed numerical instabilities when the grating amplitude approached the wavelength of light used in the calculations. Although the limit of stability depended upon the parameters of the grating and number of layers, the low limit is discouraging. Excellent



numerical stability appears to have been achieved employing a coupled-wave analysis.<sup>88,91</sup> In this analysis, the grating region is divided into a number of planar-grating slabs and the permittivity of each slab is expanded in a Fourier series. Greater computational ability may be achieved by employing the coupled-wave approach, thereby allowing a greater grating amplitude to be used in the resonant effects calculations.

## Appendix A

### DERIVATION OF THE EXTINCTION THEOREM FROM GREEN'S IDENTITY

In this Appendix, the extinction theorem relations are derived<sup>92</sup> for the incident and substrate regions [Equations (44) and (47)]. Equations (38) and (41) are substituted into the Green's identity [Equation (37)] resulting in the following relation for the upper or incident medium:

$$\begin{aligned}
 & 4\pi \iiint_{V'} H \delta(x-x') \delta(y-y') \delta(z-z') dx' dy' dz' \\
 &= \iint_{S'} \left( G_o \frac{\partial H}{\partial n} - H \frac{\partial G_o}{\partial n} \right) ds' \quad ,
 \end{aligned}
 \tag{A-1}$$

where the volume and surface of integrations pertain to the upper or incident medium. Note that Equation (A-1) is for p-polarization and that the elemental surface area  $ds' = dy'dx'\sqrt{1 + [h'(x')]^2}$  over the interface with profile shape given by  $h(x')$  and  $h'(x') = dh(x')/dx'$ .

In order to evaluate the surface integral appearing on the right side of Equation (A-1), a rectangular contour is used as shown in Figure 35. The contour is divided along four paths of integration  $P_1, P_2, P_3, P_4$ , where  $P_1$  is parallel to the  $x$ -axis and is within the incident medium;  $P_2$  and  $P_3$  are parallel to the  $z$ -axis and will be moved to  $x = \pm \infty$ ; and  $P_4$  is the contour along

the grating profile. The surface integral can be written as the sum of the surface integrals along  $P_1$ ,  $P_2$ ,  $P_3$ , and  $P_4$  yielding

$$\iint_{s'} \left( G_o \frac{\partial H}{\partial n} - H \frac{\partial G_o}{\partial n} \right) ds' = \iint_{P_1} + \iint_{P_2} + \iint_{P_3} + \iint_{P_4} . \quad (A-2)$$

In order to evaluate the surface integral along the paths  $P_1$ ,  $P_2$ , and  $P_3$ , the total magnetic field is written as the sum of the incident  $H^{inc}$  and diffracted fields  $H^{dif}$ :

$$H = H^{inc} + H^{dif} .$$

The total field  $H$ , however, is used in the evaluation of the surface integral along the grating profile  $P_4$ . Thus, the right side of Equation (A-2) can now be written:

$$\iint_{P_1} H^{inc} + H^{dif} + \iint_{P_2} H^{inc} + H^{dif} + \iint_{P_3} H^{inc} + H^{dif} + \iint_{P_4} H . \quad (A-3)$$

The integral along the grating surface  $P_4$  is to be retained in the extinction theorem. This integral is considered first. With the integral form of the three-dimensional Green's function [Equation (39)], the surface integral along  $P_4$  becomes

$$\begin{aligned}
\iint_{P_4} \left( G_o \frac{\partial H}{\partial n} - H \frac{\partial G_o}{\partial n} \right) ds' &= \frac{1}{2\pi} \iint dx' dy' \sqrt{1+h'(x')^2} \\
&\times \left\{ \int_{-\infty}^{\infty} \int dk d\beta_o \frac{1}{q_o} e^{i[k(x-x')+\beta_o(y-y')+q_o|z-z'|]} \frac{\partial H}{\partial n} \right. \\
&\left. - H \frac{\partial}{\partial n} \int_{-\infty}^{\infty} \int dk d\beta_o \frac{1}{q_o} e^{i[k(x-x')+\beta_o(y-y')+q_o|z-z'|]} \right\} .
\end{aligned} \tag{A-4}$$

Integration over  $dy'$  may be done easily by taking advantage of the fact that the geometry of this work dictates that the  $H$  fields are independent of  $y'$ . The  $dy'$  integration yields  $2\pi\delta(\beta_o)$ . Consequently, integration over  $d\beta_o$  sets  $\beta_o = 0$ . With this, the right side of Equation (A-2) reduces to

$$\begin{aligned}
\iint_{P_4} dx' \sqrt{1+(h'(x'))^2} &\left[ \frac{\partial H}{\partial n} \int \frac{dk}{q_o} e^{i[k(x-x')+q_o|z-z'|]} \right. \\
&\left. - H \frac{\partial}{\partial n} \int \frac{dk}{q_o} e^{i[k(x-x')+q_o|z-z'|]} \right] .
\end{aligned} \tag{A-5}$$

The surface integral along  $P_4$  can thus be written simply as

$$\int_{P_4} \left( G_o^{(2)} \frac{\partial H}{\partial n} - H \frac{\partial G_o^{(2)}}{\partial n} \right) dx' \sqrt{1+[h'(x')]^2} , \tag{A-6}$$

where  $G_o^{(2)}$  is the two-dimensional Green's function given by

$$G_o^{(2)} = i \int \frac{dk}{q_o} e^{i[k(x-x')+q_o|z-z'|]}$$

and  $q_0 = \sqrt{(\omega/c^2 \epsilon_0 - k^2)}$ . The superscript (2) in  $G_0^{(2)}$  is assumed from here on.

Each of the  $P_1$ ,  $P_2$ , and  $P_3$  integrals in Equation (A-3) can be further divided into an integration over  $H^{inc}$  plus  $H^{dif}$ . However, the integrals containing  $H^{dif}$  satisfy the radiation condition since only outgoing waves are involved, and thus vanish. The remaining integrals on  $P_1$ ,  $P_2$ , and  $P_3$  contain the incident field  $H^{inc}$  only.

Consider first the integral

$$\iint_{P_1} H^{inc} = \iint_{P_1} \left( G_0 \frac{\partial H^{inc}}{\partial n} - H^{inc} \frac{\partial G_0}{\partial n} \right) ds' \quad , \quad (A-7)$$

where

$$\frac{\partial G_0}{\partial n} = - \frac{\partial G_0}{\partial z'} = - \int dk \operatorname{sgn}(z+Z) e^{i[k(x-x') + q|z+Z|]}$$

$$H^{inc} = e^{i(k_0 x' - q_0 Z)}$$

and

$$\frac{\partial H^{inc}}{\partial n} = \frac{-\partial H^{inc}}{\partial z'} = -iq_0 e^{i(k_0 x' - q_0 Z)}$$

With these substitutions and the fact that  $ds' = dx'$  when evaluating the two-dimensional Green's function, Equation (A-7) becomes

$$\begin{aligned}
& \int_{-X}^{+X} dx' e^{i(k_o x' - q_o Z)} \int_{-\infty}^{\infty} dk \left[ \frac{q_o}{q} + \text{sgn}(z + Z) \right] e^{i[k(x-x') + q|z+Z|]} \\
& = \int_{-X}^{+X} dx' e^{i(k_o - k)x'} \int_{-\infty}^{\infty} dk \left[ \frac{q_o}{q} + \text{sgn}(z + Z) \right] e^{i(kx + q|z+Z| - q_o Z)}
\end{aligned} \quad (A-8)$$

As  $X \rightarrow +\infty$ ,

$$\int_{-X}^{+X} dx' e^{i(k_o - k)x'} = 2\pi\delta(k - k_o)$$

and Equation (A-8) becomes

$$\iint_{P_1} H^{inc} = 2\pi[1 + \text{sgn}(z + Z)]e^{i(k_o x + q_o |z+Z| - q_o Z)}$$

Therefore,

$$\iint_{P_1} H^{inc} = \begin{cases} 4\pi H^{inc} & \text{if } Z > -z' \\ 0 & \text{if } Z < z' \end{cases} \quad (A-9)$$

The surface integral along  $P_2$  is considered next, i.e.,

$$\iint_{P_2} H^{inc} = \iint_{P_2} ds' \left( G_o \frac{\partial H^{inc}}{\partial n} - H^{inc} \frac{\partial G_o}{\partial n} \right) \quad (A-10)$$

where

$$\frac{\partial G_o}{\partial n} = \frac{\partial G_o}{\partial x'} = \int dk \frac{k}{q} e^{ik(x-X)+q|z-z'|}$$

and

$$\frac{\partial H^{inc}}{\partial n} = \frac{\partial H^{inc}}{\partial x'} = ik_o e^{i(k_o X + q_o z')}$$

Again, the integration variable  $ds' = dz'$  when considering the two-dimensional Green's function. Equation (A-10) becomes

$$\begin{aligned} & - \int_{-Z}^{f(X)} dz' e^{i(k_o X + q_o z')} \int_{-\infty}^{\infty} dk \left( \frac{k+k_o}{q} \right) e^{ik(x-X)+q|z-z'|} \\ & = - \int_{-Z}^{f(X)} dz' e^{iq_o z'} \int_{-\infty}^{\infty} dk e^{i(k_o - k)X} f(x, z - z') \end{aligned} \quad (A-11)$$

where

$$f(x, z - z') = \left( \frac{k+k_o}{q} \right) e^{ikx+q|z-z'|} \quad (A-12)$$

For a well-defined function  $f(x, z - z')$ , the Fourier transform tends to zero as  $X \rightarrow \infty$ .<sup>93</sup> Thus, the contribution along path  $P_2$  vanishes in this limit.

Likewise, it can be shown that

$$\iint_{P_3} H^{inc} = 0 \quad (A-13)$$

Therefore, the only contributions to the surface integral along the closed contour made up of paths  $P_1$ ,  $P_2$ ,  $P_3$ , and  $P_4$  are due to (1)  $P_4$ , the grating surface path and (2)  $P_1$ , the path resulting in the incident source field.

Integration of the volume integral in Equation (A-1) results in the magnetic field evaluated at the observation point  $(x,y,z)$ . This is the total magnetic field in the upper region,  $H_0^{\text{total}}$ , which equals the incident plus diffracted magnetic fields. If, however, the observation point is located outside the region of integration, then this volume integral is zero. This term can thus be written:

$$4\pi \iiint_V H \delta(x-x') \delta(y-y') \delta(z-z') dx' dy' dz' = \begin{cases} 4\pi H_0^{\text{total}} & z < d_0 + h(x) \\ 0 & z > d_0 + h(x) \end{cases} \quad (\text{A-14})$$

Finally, combining Equations (A-6), (A-9), and (A-14) gives the extinction theorem, Equation (44).

The extinction theorem relations for the substrate region ( $j = s$ ) are formed by substituting Equations (38) and (46) into Green's identity, yielding

$$4\pi \iiint_{V'} H \delta(x-x') \delta(y-y') \delta(z-z') dv' = \iint_{S'} \left( G_s \frac{\partial H}{\partial n} - H \frac{\partial G_s}{\partial n} \right) ds' \quad (\text{A-15})$$



Integration of the left side of Equation (A-15) over the volume enclosing the lower medium results in the magnetic field evaluated at observation points  $(x,y,z)$  within the lower region. This field  $H(x,y,z)$  is termed the transmitted, diffracted field  $H_s^{\text{trans}}$ . Again, if the observation point is located outside of the volume of integration, the volume integral equals zero.

Finally, substitution of the elemental surface area  $ds' = dy'dx'\sqrt{1+[h'(x')]^2}$  into Equation (A-15) results in the extinction theorem relation, Equation (47).

## Appendix B

### CALCULATION OF MATRIX ELEMENTS FOR ARBITRARY GROOVE PROFILE

Calculation of the matrix elements  $\phi_{nm}^{\pm}$  and  $\eta_{nm}^{\pm}$  can be accomplished explicitly for trapezoidal and sinusoidal groove profiles. For an arbitrary shape, a point-to-point integration was used;  $\phi_{nm}^{\pm}$  is written as

$$\phi_{nm}^{\pm} = \frac{1}{D} \int_0^D dx e^{i \frac{2\pi}{D}(m-n)x} e^{\pm i q_n h(x)} \quad . \quad (B-1)$$

Next, the following substitution is made:

$$\alpha \rightarrow \frac{x}{D} \quad ,$$

which results in

$$\phi_{nm}^{\pm} = \int_0^1 d\alpha e^{i 2\pi(m-n)\alpha} e^{\pm i q_n h(\alpha)} \quad . \quad (B-2)$$

Considering Figure 35, the equation of a line between points  $y(j)$  and  $y(j+1)$  is

$$\begin{aligned} h(\alpha) &= \left( \frac{h(j+1) - h(j)}{y(j+1) - y(j)} \right) (\alpha - y(j)) + h(j) \\ &= \left( \frac{h(j+1) - h(j)}{y(j+1) - y(j)} \right) \alpha - \left( \frac{h(j+1) - h(j)}{y(j+1) - y(j)} \right) y(j) + h(j) \quad . \end{aligned} \quad (B-3)$$

The integration over one period is divided into integrations over  $J$  straight-line segments. Thus,  $\phi_{nm}^{\pm}$  is separated into  $J$ -independent elements,  $\phi_{j,nm}^{\pm}$ , where  $j = 1, 2, \dots, J$ .

For convenience, let

$$S = \frac{h(j+1) - h(j)}{y(j+1) - y(j)} ; \quad (B-4)$$

then

$$\begin{aligned} \phi_{j,nm}^{\pm} &= \int_{y(j)}^{y(j+1)} d\alpha e^{i2\pi(m-n)\alpha} e^{\pm i q_n (s\alpha - sy(j) + h(j))} \\ &= \int_{y(j)}^{y(j+1)} d\alpha e^{i[2\pi(m-n) \pm q_n s]\alpha} e^{\pm i q_n (-sy(j) + h(j))} \end{aligned} \quad (B-5)$$

It is advantageous to change the integration limits from  $y(j) \rightarrow y(j+1)$  to  $P(j) - \Delta P \rightarrow P(j) + \Delta P$ , where  $P(j)$  is the midpoint of the  $j$ th segment and  $\Delta P$  is half the length of the  $j$ th segment along the  $y$ -axis.

Direct integration of Equation (B-5) results in

$$\begin{aligned} \phi_{j,nm}^{\pm} &= e^{\pm i q_n (-Sy(j) + h(j))} \left[ \frac{e^{i(2\pi(m-n) \pm q_n S)(P(j) + \Delta P)} - e^{i(2\pi(m-n) \pm q_n S)(P(j) - \Delta P)}}{i(2\pi(m-n) \pm q_n S)} \right] \\ &= e^{\pm i q_n (-Sy(j) + h(j))} e^{i(2\pi(m-n) \pm q_n S)P(j)} \frac{\sin(2\pi(m-n) \pm q_n S)\Delta P}{\pi(m-n) \pm q_n S} \end{aligned} \quad (B-6)$$

Finally,

$$\phi_{nm}^{\pm} = \sum_{j=1}^N \phi_{j,nm}^{\pm} . \quad (\text{B-7})$$

The matrix elements  $\eta_{nm}^{\pm}$  are related to  $\phi_{nm}^{\pm}$  by Equation (78).

### Appendix C

#### CALCULATION OF MATRIX ELEMENTS FOR SINUSOIDAL GROOVE PROFILE

The matrix elements for a sinusoidal groove profile, where

$$h(x) = b \sin\left(\frac{2\pi}{D} x\right), \quad (C-1)$$

are calculated as follows. Let

$$\phi_{nm}^{\pm} = \frac{1}{D} \int_0^D e^{\pm i b q_n \sin\left(\frac{2\pi}{D} x\right)} e^{i(k_m - k_n)x} dx. \quad (C-2)$$

Recognizing that the Bessel function<sup>94</sup>  $J_p(z)$  is

$$J_p(z) = \frac{1}{2\pi} \int_0^{2\pi} e^{-i(z \sin \theta - p\theta)} d\theta, \quad (C-3)$$

the following substitution,

$$\theta = \frac{2\pi}{D} x, \quad (C-4)$$

is made in (C-2) above, resulting in

$$\begin{aligned}
\phi_{nm}^{\pm} &= \frac{1}{2\pi} \int_0^{2\pi} e^{\pm i b q_n \sin \theta + i(m-n)\theta} d\theta \\
&= \begin{cases} J_{p=m-n}(-bq_n) = (-1)^p J_{p=m-n}(bq_n) & \text{for } \phi_{nm}^+ \\ J_{p=m-n}(bq_n) & \text{for } \phi_{nm}^- \end{cases} .
\end{aligned}
\tag{C-5}$$

## Appendix D

### EXTINCTION THEOREM COMPUTER PROGRAM

The computer program, written in Fortran, calculates intensities of the diffracted fields and coefficients of the evanescent fields just above the surface of the film for each diffraction order up to the order of the calculation. Intensities are calculated as a function of angle of incidence, wavelength, or grating period. It would be a simple matter to modify the program to scan in groove height as well. The program allows for homogeneous multilayers, transverse electric (TE) or transverse magnetic (TM) polarization, and any groove profile at each film interface. Absorption is allowed for all media except the incident. The groove profile is divided into a number of straight-line segments, and the integration routine calculates the matrix elements between points connecting the straight-line segments. The order of the calculation is also variable; for any order, however, convergence should be tested by comparing numerical results attained by increasing the order of the calculation.

As it is currently written, the main program calls for data file 20 in which input data are stored. A sample input file is shown in Table 3(a). The program can be specified by the following input parameters that are stored in the data file:

1. Grating period, number of overlayers, order of the calculation, and wavelength in microns for the calculation if a wavelength scan is not wanted
2. Beginning, final, and increment in angle of incidence
3. Complex permittivity and thickness in microns of each layer (layer 1 is the substrate)
4. Number of points for each interface in which the groove profile over one period is divided
5. Beginning at the substrate, the groove profile specified over one period.

TABLE 3(a). Sample Input Files.

```

.7,1,7,.6328
40.5,42.0,.1
(2.25,0.0),0.0
(5.11,0.0),.25
(1.0,0.0),0.0
8,8
0.0,0.0
.05,0.0
.15,.0
.85,.0
.95,0.0
1.0,0.0
0.0,0.0
.05,0.0
.15,.01
.85,.01
.95,0.0
1.0,0.0

```

The number of points at each interface must be identical to the number of points stated in 4 above. Each point specifying the groove profile contains



two numbers: (1) the fraction of a period along the x-axis and (2) the height of the groove (in microns) at the x-value.

Interactive input parameters to be entered are the following:

1. TE or TM polarization (s or p)
2. The beginning, final, and wavelength increment if a wavelength scan is to be used.

In case 2, the angle of incidence used in the calculation is the beginning angle stored in the input file.

The program output is sent to the screen and to output file 25, where the data can be used in a plotting routine. Table 3(b) shows a sample screen output. Following the angle of incidence, a three-number line appears. The first is the condition of the matrix. The determinant of the propagation matrix is given by the next two numbers as a singly subscripted array with two elements in the form  $\det(A) = \text{DET}(1) * 10.0 ** \text{DET}(2)$ . Next appears three columns. The first column is the diffracted order, followed by the expansion coefficient of the field evaluated just above the top surface of the film assembly in the second column. The third column gives the field intensity for each propagating order. The sum of the intensities in the propagating fields is shown also. The output stored in file 25 can be used for plotting purposes.

TABLE 3(b). Sample Output Files.

```

40.50000000000000
5.221582531949289      (0.5108838962376867, 0.5917645529352254)
-7  7.2377867514169247E-08  0.0000000000000000E+00
-6  1.2871755826966346E-07  0.0000000000000000E+00
-5  2.5118561285902428E-08  0.0000000000000000E+00
-4  1.0868438538519593E-06  0.0000000000000000E+00
-3  3.4976888590827479E-04  0.0000000000000000E+00
-2  6.0496733178791677E-05  0.0000000000000000E+00
-1  1.9062593197104572E-04  2.4243174126400967E-04
 0  0.3527354678283363      0.3527354678283363
 1  3.8930510438667169E-02  0.0000000000000000E+00
 2  1.2904674263245593E-04  0.0000000000000000E+00
 3  1.9020389749217778E-05  0.0000000000000000E+00
 4  2.8693726883088512E-06  0.0000000000000000E+00
 5  2.0635922920448664E-07  0.0000000000000000E+00
 6  3.4353937305555226E-09  0.0000000000000000E+00
 7  2.9830442682932901E-08  0.0000000000000000E+00
0.3529778995696003

```

The structure of the program closely follows the theory developed in the text. A copy of the program is included in this Appendix. Numbers to the right of the program statements refer to the equations numbered in the text. A number of subroutines are called during execution of the program. The subroutines TINV5 and TINVB5 used Linpack routines to solve linear equation systems of the form  $Ax = B$ . When B is the identity matrix, the inverse of A is found. These subroutines also factor A and estimate its condition.<sup>95</sup> The subroutine DETER also uses Linpack routines to calculate the determinant of a matrix. The subroutine BESSEL calculates Bessel functions and matrix elements for sinusoidal groove profiles. A modification to the program as it is currently written must be made in order to call the BESSEL subroutine for a particular layer interface. Finally, the IO file allows interactive declaration of the input and output data files.

## EXTINCTION THEOREM COMPUTER PROGRAM

C R-MATRIX TECHNIQUE - POINT TO POINT PROFILE

C EXTINTION THEORY PROGRAM - ORDER VARIABLE-13 LAYERS MAX

C S OR P POLARIZATION

INTEGER ORDER, O, O2, LA, LDA

PARAMETER (O=15, O2=30, LA=15, LDA=15)

INTEGER WA(O), WA2(O2), NPTS(LA), PT

COMPLEX\*16 I, E(LA), Q(O, LA), Q1(O2, O2, LA), C1(O), C2(O2), Q2(O2, O2, LA)

COMPLEX\*16 Q3(O2, O2, LA), Z4(O, O), Z5(O, O), Z6(O, O), MU(O)

COMPLEX\*16 R1, R2, R3, R4, R5, Z0, P1(O, O, LA), P3(O, O, LA), ICINC(O, O)

COMPLEX\*16 Z1(O, O), Z0(O, O), Z2(O, O), Z3(O, O), PS1(O, O)

COMPLEX\*16 IPS2(O, O), HIL(O, O), CDIF(O, O), CINC(C, O), JV(O:200)

COMPLEX\*16 A(O2, O2), B(O2, O2), X(O, O), Y(O, O), Y2(O, O), Y3(O, O)

COMPLEX\*16 PS2(O, O), ICDIF(O, O), MU2(O2), Z7(O, O), Z8(O, O)

REAL\*8 K(O), KO, D(LA), T(LA), PERIOD, LAMDA, BETA, S1, S2, ABC

REAL\*8 WC, TO, H(20, LA), PI, T1, T2, DT, SUM, ALPHA, DELTAPT(20, LA)

REAL\*8 DELTAPT2(20, LA), SLOPE(20, LA), YY(20, LA), YPOS, LL1, LL2, DL

COMPLEX\*16 QS4(O, O, LA), QS3(O, O, LA), IQS3(O, O), RR(O, O, LA), X1, X2

COMPLEX\*16 ZZ(O, O, LA), IZZ(O, O), ZZ1(O, O, LA), ZZ2(O, O, LA)

COMPLEX\*16 RU(O, O), DRU(O, O), AB1(O, O, LA), AB2(O, O, LA), AB3(O, O, LA)

COMPLEX\*16 AB4(O, O, LA), IAB1(O, O), IAB2(O, O), IAB3(O, O), IAB4(O, O)

COMPLEX\*16 AA5(O, O, LA), AA6(O, O, LA), AA(O, O, LA), IAA(O, O)

COMPLEX\*16 BB5(O, O, LA), BB6(O, O, LA), BB(O, O, LA), IBB(O, O)

COMPLEX\*16 INC1(O, O, LA), INC2(O, O, LA), INC3(O, O, LA), INC(O, O, LA)

COMPLEX\*16 DIF1(O, O, LA), DIF2(O, O, LA), DIF3(O, O, LA), DIF(O, O, LA)

COMPLEX\*16 IINC(O, O), IDIF(O, O), P1U(O, O, LA), P1L(O, O, LA)

COMPLEX\*16 P3L(O, O, LA), P3U(O, O, LA)

CHARACTER\*100 Input\_File

CHARACTER S\*1, P\*1, POLAR\*1, ANSWER\*4, YES\*4, NINE\*4

INTEGER INUNIT, OUTUNIT

PARAMETER (INUNIT=20, OUTUNIT=25)

CALL IOFile (InUnit, OutUnit, Input\_File)

TYPE\*, 'S OR P POLARIZATION S/P'

ACCEPT 10, POLAR

10 FORMAT(A)

READ(20, \*) PERIOD, LAYERS, ORDER, LAMDA

READ(20, \*) T1, T2, DT

C WRITE(25, 172) H

172 FORMAT('HEIGHT=', F10.8)

L1=LAYERS+1

L2=LAYERS+2

READ(20, \*) (E(L), T(L), L=1, L2)

READ(20, \*) (NPTS(L), L=1, L1)

```

DO 179 L=1,L1
READ(20,*)(YY(PT,L),H(PT,L),PT=1,NPTS(L))
179 CONTINUE
NO=2*ORDER+1
NO2=2*NO
NULL=ORDER+1
I=(0.0D00,1.0D00)
PI=DACOS(-1.0D00)
WC=2.0D00*PI/LAMDA

TYPE*, 'WAVELENGTH SCAN! YES/NINE'
ACCEPT 10,ANSWER
IF(ANSWER.EQ. 'NINE') THEN
ITLIM=INT((T2-T1)/DT)+1
WRITE(25,*) ITLIM
ELSE
TYPE*, 'ENTER BEGINNING,FINAL WAVELENGTH AND INCREMENT IN MICRONS'
ACCEPT*,LL1,LL2,DL
ITLIM=INT((LL2-LL1)/DL)+1
WRITE(25,*) ITLIM
END IF
80 DO 1000 IT=1,ITLIM
IF(ANSWER.EQ. 'NINE') GO TO 85
LAMDA=LL1+(IT-1)*DL
TYPE*, 'WAVELEGTH=',LAMDA
TO=T1
WC=2.0D00*PI/LAMDA
WRITE(25,*) LAMDA
GO TO 175
85 TO=T1+(IT-1)*DT
TYPE*, 'ANGLE OF INCIDENCE =',TO
WRITE(25,*) TO
171 FORMAT('ANGLE OF INCIDENCE=',F6.2)
175 KO=DSIN(TO*PI/180.0D00)
D(1)=0.0D00
IF(L1.EQ.1) GO TO 202
DO 203 L=2,L1
203 D(L)=D(L-1)+T(L)
C NEXT THREE LINES FOR TRAP CALCS ONLY
202 DO 209 ISIGN=1,2
IF (ISIGN.EQ.1) IS=1
IF (ISIGN.EQ.2) IS=-1
DO 201 LL=1,L2
DO 201 JJ=1,NO
N=JJ-NULL
K(JJ)=(KO+N*LAMDA/PERIOD)*WC

```

(71)

```

      Q(JJ,LL)=IS*CDSQRT(E(LL)*WC**2-K(JJ)**2)          (102)
C   USE Q ABOVE FOR TRAP.CALC
C   USE Q BELOW FOR BESSEL ROUTINE
C      Q(JJ,LL)=CDSQRT(E(LL)*WC**2-K(JJ)**2)
201  CONTINUE
C      CALL BESSEL(Q,JV,L2,NO,H,P1,P3,LA,P1Q,P3Q)
      L=1
      JJ=1
204  DO 208 N=1,NO
      DO 208 M=1,NO
      YPOS=0.0D00
      IF(ISIGN.EQ.1) P1(N,M,L)=(0.0D00,0.0D00)
      P3(N,M,L)=(0.0D00,0.0D00)
206  DO 211 PT=2,NPTS(JJ)
      DELTAPT(PT,JJ)=YY(PT,JJ)-YY(PT-1,JJ)
      IF (DELTAPT(PT,JJ).EQ.0.0) GO TO 211
      DELTAPT2(PT,JJ)=DELTAPT(PT,JJ)/2.0D00
      YPOS=YPOS+DELTAPT(PT-1,JJ)
      SLOPE(PT,JJ)=(H(PT,JJ)-H(PT-1,JJ))/DELTAPT(PT,JJ)      (S: eq. B-4)
      X1=Q(N,L)*(-SLOPE(PT,JJ)*YPOS+H(PT-1,JJ))
      X2=2.0*PI*(M-N)+Q(N,L)*SLOPE(PT,JJ)
      R1=2.0*CDEXP(I*X1)
      R2=CDEXP(I*X2*(YPOS+DELTAPT2(PT,JJ)))
      R3=CDSIN(X2*DELTAPT2(PT,JJ))
      IF(ISIGN.EQ.1.AND.X2.EQ.(0.0,0.0)) THEN
      P1(N,M,L)=P1(N,M,L)+R1*R2*DELTAPT2(PT,JJ)
      ELSEIF(ISIGN.EQ.1) THEN                                  (φ+nm,j: eq. B-6)
      P1(N,M,L)=P1(N,M,L)+R1*R2*R3/X2
      ELSE
      CONTINUE
      ENDIF
      IF(ISIGN.EQ.2.AND.X2.EQ.(0.0,0.0)) THEN
      P3(N,M,L)=P3(N,M,L)+R1*R2*DELTAPT2(PT,JJ)
      ELSEIF(ISIGN.EQ.2) THEN                                  (φ-nm,j: eq. B-6)
      P3(N,M,L)=P3(N,M,L)+R1*R2*R3/X2
      ELSE
      CONTINUE
      ENDIF
211  CONTINUE
208  CONTINUE
      IF(L.EQ.L2) GO TO 210
      L=L2
      JJ=L2-1
      GO TO 204
210  IF(L1.EQ.1) GO TO 209

```

```

DO 220 L=2,L1
DO 220 N=1,NO
DO 220 M=1,NO
YPOS=0.0D00
IF(ISIGN.EQ.1) P1U(N,M,L)=(0.0D00,0.0D00)
P3U(N,M,L)=(0.0D00,0.0D00)
DO 221 PT=2,NPTS(L)
DELTAPT(PT,L)=YY(PT,L)-YY(PT-1,L)
IF (DELTAPT(PT,JJ).EQ.0.0) GO TO 221
DELTAPT2(PT,L)=DELTAPT(PT,L)/2.0D00
YPOS=YPOS+DELTAPT(PT-1,L)

SLOPE(PT,L)=(H(PT,L)-H(PT-1,L))/DELTAPT(PT,L)
X1=Q(N,L)*(-SLOPE(PT,L)*YPOS+H(PT-1,L))
X2=2.0*PI*(M-N)+Q(N,L)*SLOPE(PT,L)
R1=2.0*CDEXP(I*X1)
R2=CDEXP(I*X2*(YPOS+DELTAPT2(PT,L)))
R3=CDSIN(X2*DELTAPT2(PT,L))
IF(ISIGN.EQ.1.AND.X2.EQ.(0.0,0.0)) THEN
P1U(N,M,L)=P1U(N,M,L)+R1*R2*DELTAPT2(PT,L)
ELSEIF(ISIGN.EQ.1) THEN
P1U(N,M,L)=P1U(N,M,L)+R1*R2*R3/X2
ELSE
CONTINUE
ENDIF
IF(ISIGN.EQ.2.AND.X2.EQ.(0.0,0.0)) THEN
P3U(N,M,L)=P3U(N,M,L)+R1*R2*DELTAPT2(PT,L)
ELSEIF(ISIGN.EQ.2) THEN
P3U(N,M,L)=P3U(N,M,L)+R1*R2*R3/X2
ELSE
CONTINUE
ENDIF
221 CONTINUE
220 CONTINUE

DO 230 L=2,L1
DO 230 N=1,NO
DO 230 M=1,NO
YPOS=0.0D00
IF(ISIGN.EQ.1) P1L(N,M,L)=(0.0D00,0.0D00)
P3L(N,M,L)=(0.0D00,0.0D00)
DO 231 PT=2,NPTS(L-1)
DELTAPT(PT,L)=YY(PT,L-1)-YY(PT-1,L-1)
IF (DELTAPT(PT,L).EQ.0.0) GO TO 231
DELTAPT2(PT,L)=DELTAPT(PT,L)/2.0D00
YPOS=YPOS+DELTAPT(PT-1,L)

```

( $\phi^+_{nm,j}$ : eq. B-6)  
upper surface

( $\phi^-_{nm,j}$ : eq. B-6)  
upper surface

```

SLOPE(PT,L)=(H(PT,L-1)-H(PT-1,L-1))/DELTAPT(PT,L)
X1=Q(N,L)*(-SLOPE(PT,L)*(YPOS)+H(PT-1,L-1))
X2=2.0*PI*(M-N)+Q(N,L)*SLOPE(PT,L)
R1=2.0*CDEXP(I*X1)
R2=CDEXP(I*X2*(DELTAPT2(PT,L)+YPOS))
R3=CDSIN(X2*DELTAPT2(PT,L))
IF(ISIGN.EQ.1.AND.X2.EQ.(0.0,0.0)) THEN
P1L(N,M,L)=P1L(N,M,L)+R1*R2*DELTAPT2(PT,L)
ELSEIF(ISIGN.EQ.1) THEN
P1L(N,M,L)=P1L(N,M,L)+R1*R2*R3/X2
ELSE
CONTINUE
ENDIF
IF(ISIGN.EQ.2.AND.X2.EQ.(0.0,0.0)) THEN
P3L(N,M,L)=P3L(N,M,L)+R1*R2*DELTAPT2(PT,L)
ELSEIF(ISIGN.EQ.2) THEN
P3L(N,M,L)=P3L(N,M,L)+R1*R2*R3/X2
ELSE
CONTINUE
ENDIF
231 CONTINUE
230 CONTINUE
209 CONTINUE

240 DO 291 LL=1,L2
DO 291 JJ=1,NO
N=JJ-NULL
K(JJ)=(KO+N*LAMDA/PERIOD)*WC

Q(JJ,LL)=CDSQRT(E(LL)*WC**2-K(JJ)**2)
291 CONTINUE

DO 3000 I3=1,NO
DO 3000 I4=1,NO
L=1
IF(POLAR.EQ.'P') THEN
QS4(I3,I4,L)=-I*P1(I3,I4,L)*E(1)/E(2)
QS3(I3,I4,L)=P1(I3,I4,L)*((E(L)*WC**2-K(I3)*K(I4))/Q(I3,L))
ELSE
QS4(I3,I4,L)=-I*P1(I3,I4,L)
QS3(I3,I4,L)=P1(I3,I4,L)*Q(I3,L)
END IF

3000 CONTINUE
CALL TINV5(QS3,IQS3,X,MU,WA,NO,L,L2,C1,RCOND,LDA)
DO 3110 I3=1,NO

```

( $\phi^+_{nm,j}$ : eq. B-6)  
lower surface

( $\phi^-_{nm,j}$ : eq. B-6)  
lower surface

( $\eta^+_{nm,j}$ : eq. B-7)

```

DO 3110 I4=1,NO
RR(I3,I4,1)=(0.0D00,0.0D00)
DO 3100 M=1,NO
3100 RR(I3,I4,1)=RR(I3,I4,1)+IQS3(I3,M)*QS4(M,I4,1) (122)
3110 CONTINUE

DO 2000 L=2,L2
IF(T(2).EQ.0.0) THEN
DO 712 I3=1,NO
DO 712 I4=1,NO
RU(I3,I4)=RR(I3,I4,1)
712 CONTINUE
GO TO 6650
ELSE IF(T(L).EQ.0.0) THEN
L0=L
GO TO 3115
ELSE
GO TO 293
END IF

293 DO 700 I4=1,NO
DO 700 I3=1,NO
ZO=I*Q(I3,L)*T(L)

IF(POLAR.EQ.'P') THEN
Q1(I3,I4,L)=((E(L)*WC**2-K(I3)*K(I4))/Q(I3,L))
**P3L(I3,I4,L)*CDEXP(-ZO)
Q1(I3,I4+NO,L)=-((E(L)*WC**2-K(I3)*K(I4))/Q(I3,L))*P3U(I3,I4,L)
Q1(I3+NO,I4,L)=-((E(L)*WC**2-K(I3)*K(I4))/Q(I3,L))
**P1L(I3,I4,L)*CDEXP(ZO)
Q1(I3+NO,I4+NO,L)=((E(L)*WC**2-K(I3)*K(I4))/Q(I3,L))*P1U(I3,I4,L)

Q2(I3,I4,L)=I*P3L(I3,I4,L)*CDEXP(-ZO)
Q2(I3,I4+NO,L)=-I*P3U(I3,I4,L)*E(L)/E(L+1)
Q2(I3+NO,I4,L)=I*P1L(I3,I4,L)*CDEXP(ZO)
Q2(I3+NO,I4+NO,L)=-I*P1U(I3,I4,L)*E(L)/E(L+1)
ELSE
Q1(I3,I4,L)=Q(I3,L)
**P3L(I3,I4,L)*CDEXP(-ZO)
Q1(I3,I4+NO,L)=-Q(I3,L)*P3U(I3,I4,L)
Q1(I3+NO,I4,L)=-Q(I3,L)
**P1L(I3,I4,L)*CDEXP(ZO)
Q1(I3+NO,I4+NO,L)=Q(I3,L)*P1U(I3,I4,L)

Q2(I3,I4,L)=I*P3L(I3,I4,L)*CDEXP(-ZO)

```



```

      Q2(I3,I4+NO,L)=-I*P3U(I3,I4,L)
      Q2(I3+NO,I4,L)=I*P1L(I3,I4,L)*CDEXP(ZO)
      Q2(I3+NO,I4+NO,L)=-I*P1U(I3,I4,L)
      END IF
700  CONTINUE
      CALL TINVB5(Q1,A,B,MU2,WA2,NO2,L,L2,C2,RCOND,LDA)
C    WRITE(25,34) L,RCOND
34   FORMAT('L=',I2'RCOND=',D13.4)

      DO 710 I4=1,NO2
      DO 710 I3=1,NO2
      Q3(I3,I4,L)=(0.0D00,0.0D00)
      DO 711 M=1,NO2
711  Q3(I3,I4,L)=Q3(I3,I4,L)+A(I3,M)*Q2(M,I4,L)          (116)
710  CONTINUE
2000 CONTINUE

3115 DO 4000 L=2,L0-1
      DO 5000 I3=1,NO
      DO 5000 I4=1,NO
      ZZ(I3,I4,L)=Q3(I3,I4,L)-RR(I3,I4,L-1)
5000 CONTINUE
      CALL TINV5(ZZ,IZZ,X,MU,WA,NO,L,L2,C1,RCOND,LDA)
      DO 5110 I3=1,NO
      DO 5110 I4=1,NO
      ZZ1(I3,I4,L)=(0.0D00,0.0D00)
      DO 5100 M=1,NO
5100  ZZ1(I3,I4,L)=ZZ1(I3,I4,L)+IZZ(I3,M)*Q3(M,I4+NO,L)
5110  CONTINUE
      DO 6000 I3=1,NO
      DO 6000 I4=1,NO
      ZZ2(I3,I4,L)=(0.0D00,0.0D00)
      DO 6500 M=1,NO
6500  ZZ2(I3,I4,L)=ZZ2(I3,I4,L)+Q3(I3+NO,M,L)*ZZ1(M,I4,L)
      RR(I3,I4,L)=Q3(I3+NO,I4+NO,L)-ZZ2(I3,I4,L)          (121)
6000  CONTINUE

4000  CONTINUE
      DO 4050 I3=1,NO
      DO 4050 I4=1,NO
      RU(I3,I4)=RR(I3,I4,L0-1)
      DRU(I3,I4)=RU(I3,I4)
4050  CONTINUE

      CALL DETER(DRU,WA,NO,C1,RCOND,LDA,COND,DET,WORK)

```

```

6650 DO 7000 I3=1,NO
      DO 7000 I4=1,NO
      AB1(I3,I4,L2)=P3(I3,I4,L2)

      IF(POLAR.EQ.'P') THEN
      AB2(I3,I4,L2)=P3(I3,I4,L2)*((E(L2)*WC**2-K(I3)*K(I4))/Q(I3,L2))
      AB4(I3,I4,L2)=P1(I3,I4,L2)*((E(L2)*WC**2-K(I3)*K(I4))/Q(I3,L2))
      ELSE
      AB2(I3,I4,L2)=P3(I3,I4,L2)*Q(I3,L2)
      AB4(I3,I4,L2)=P1(I3,I4,L2)*Q(I3,L2)
      END IF
      AB3(I3,I4,L2)=P1(I3,I4,L2)
7000 CONTINUE
      L=L2
      CALL TINV5(AB1,IAB1,X,MU,WA,NO,L,L2,C1,RCOND,LDA)
      CALL TINV5(AB2,IAB2,X,MU,WA,NO,L,L2,C1,RCOND,LDA)
      CALL TINV5(AB3,IAB3,X,MU,WA,NO,L,L2,C1,RCOND,LDA)
      CALL TINV5(AB4,IAB4,X,MU,WA,NO,L,L2,C1,RCOND,LDA)

      DO 7500 I3=1,NO
      DO 7500 I4=1,NO
      AA5(I3,I4,L2)=(0.0D00,0.0D00)
      AA6(I3,I4,L2)=(0.0D00,0.0D00)
      BB5(I3,I4,L2)=(0.0D00,0.0D00)
      BB6(I3,I4,L2)=(0.0D00,0.0D00)
      DO 7700 M=1,NO
      AA5(I3,I4,L2)=AA5(I3,I4,L2)+IAB1(I3,M)*AB2(M,I4,L2)
      AA6(I3,I4,L2)=AA6(I3,I4,L2)+IAB3(I3,M)*AB4(M,I4,L2)
      BB5(I3,I4,L2)=BB5(I3,I4,L2)+IAB2(I3,M)*AB1(M,I4,L2)
7700 BB6(I3,I4,L2)=BB6(I3,I4,L2)+IAB4(I3,M)*AB3(M,I4,L2)
      AA(I3,I4,L2)=AA5(I3,I4,L2)+AA6(I3,I4,L2)
      BB(I3,I4,L2)=BB5(I3,I4,L2)+BB6(I3,I4,L2))*I
7500 CONTINUE

      CALL TINV5(AA,IAA,X,MU,WA,NO,L,L2,C1,RCOND,LDA)
      CALL TINV5(BB,IBB,X,MU,WA,NO,L,L2,C1,RCOND,LDA)
      DO 8000 I3=1,NO
      DO 8000 I4=1,NO
      INC1(I3,I4,L2)=(0.0D00,0.0D00)
      DO 8100 M=1,NO
8100 INC1(I3,I4,L2)=INC1(I3,I4,L2)+IBB(I3,M)*IAB2(M,I4)
8000 CONTINUE

      DO 8200 I3=1,NO
      DO 8200 I4=1,NO
      INC2(I3,I4,L2)=(0.0D00,0.0D00)

```

```

      INC3(I3,I4,L2)=(0.0D00,0.0D00)
      DO 8300 M=1,NO
      INC2(I3,I4,L2)=INC2(I3,I4,L2)+RU(I3,M)*INC1(M,I4,L2)
8300  INC3(I3,I4,L2)=INC3(I3,I4,L2)+IAA(I3,M)*IAB1(M,I4)
      INC(I3,I4,L2)=INC3(I3,I4,L2)+INC2(I3,I4,L2)
8200  CONTINUE

      DO 8500 I3=1,NO
      DO 8500 I4=1,NO
      DIF1(I3,I4,L2)=(0.0D00,0.0D00)
      DO 8600 M=1,NO
8600  DIF1(I3,I4,L2)=DIF1(I3,I4,L2)+IBB(I3,M)*IAB4(M,I4)
8500  CONTINUE

      DO 8700 I3=1,NO
      DO 8700 I4=1,NO
      DIF2(I3,I4,L2)=(0.0D00,0.0D00)
      DIF3(I3,I4,L2)=(0.0D00,0.0D00)
      DO 8800 M=1,NO
      DIF2(I3,I4,L2)=DIF2(I3,I4,L2)+RU(I3,M)*DIF1(M,I4,L2)
8800  DIF3(I3,I4,L2)=DIF3(I3,I4,L2)+IAA(I3,M)*IAB3(M,I4)
      DIF(I3,I4,L2)=DIF3(I3,I4,L2)-DIF2(I3,I4,L2)
8700  CONTINUE

C      CALL TINV5(INC,IINC,X,MU,WA,NO,L,L2,C1,RCOND,LDA)
C      CALL TINV5(DIF,IDIF,X,MU,WA,NO,L,L2,C1,RCOND,LDA)
      DO 901 I3=1,NO
      DO 901 I4=1,NO
C      TYPE*,I3,I4,CDIF,ICDIF
      MU(I3)=INC(I3,NULL,L2)*Q(NULL,L2)
C      TYPE*, 'MU(I3)', I3,I4,MU(I3), 'ANGLE OF INCIDENCE', TO
      X(I3,I4)=-DIF(I3,I4,L2)*Q(I4,L2)
901  CONTINUE
      CALL ZGECO(X,LDA,NO,WA,RCOND,C1)
C      WRITE(25,35) RCOND
      CALL ZGESL(X,LDA,NO,WA,MU,0)
      DO 520 I3=1,NO
(125)

C      WRITE(25,45) I3=NULL,MU(I3)
      TYPE*,I3=NULL, (CDABS(MU(I3)))**2,DREAL(Q(I3,L2)/Q(NULL,L2))
      C*(CDABS(MU(I3)))**2
C      TYPE*, 'ORDER, FIELD=', I3=NULL,MU(I3)
520  CONTINUE

      DO 533 I3=1,NO
      TYPE*,I3=NULL, 'PHAZ IS',ASIND(DIMAG(MU(I3))/CDABS(MU(I3)))

```

533 CONTINUE

```
SUM=0.0D00
DO 2 I3=1,NO
ABC=DREAL(Q(I3,L2)/Q(NULL,L2))
IF(DABS(K(I3)).GE.WC) WRITE(25,*) (CDABS(MU(I3)))**2
IF(DABS(K(I3)).LT.WC) WRITE(25,*) ABC*(CDABS(MU(I3)))**2
```

```
IF(DABS(K(I3)).GE.WC) GO TO 2
SUM=SUM+DREAL(Q(I3,L2)*(CDABS(MU(I3)))**2)
2 CONTINUE
SUM=SUM/Q(NULL,L2)
TYPE*, 'SUM=', SUM
WRITE(25,*) SUM
65 FORMAT('SUM=', 2D15.5)
1000 CONTINUE
45 FORMAT(I5, 2D15.5)
55 FORMAT(2D15.5)
STOP
END
```

C234567

```
SUBROUTINE TINV5(P1,Y,X,MU,WA,NO,L,L2,C1,RCOND,LDA)
REAL*8 T,RCOND
COMPLEX*16 P1(NO,NO,L2),Y(NO,NO),MU(NO),X(NO,NO),C1(NO)
INTEGER WA(NO),LDA
```

```
J=1
DO 4 K=1,NO
DO 4 I=1,NO
X(I,K)=P1(I,K,L)
4 CONTINUE
```

```
CALL ZGECO(X,LDA,NO,WA,RCOND,C1)
T=1.0+RCOND
IF(T.EQ.1.0) GO TO 90
DO 2 M=1,NO
DO 1 I=1,NO
1 MU(I)=(0.D00,0.D00)
MU(M)=(1.D00,0.D00)
CALL ZGESL(X,LDA,NO,WA,MU,0)
DO 6 I=1,NO
6 Y(I,J)=MU(I)
J=J+1
```

```

2      CONTINUE
      RETURN
90     TYPE *, 'MATRIX IS SINGULAR TO WORKING PRECISION'
      RETURN
      END

```

```

      SUBROUTINE TINVB5(Q1,A,B,MU2,WA2,NO2,L,L2,C2,RCOND,LDA)
C234567
      REAL*8 T,RCOND
      COMPLEX*16 Q1(NO2,NO2,L2),B(NO2,NO2),MU2(NO2),C2(NO2),A(NO2,NO2)
      INTEGER WA2(NO2),LDA,LDA2
      LDA2=LDA*2
      J=1
      DO 4 K=1,NO2
      DO 4 I=1,NO2
      B(I,K)=Q1(I,K,L)
4      CONTINUE
      CALL ZGECO(B,LDA2,NO2,WA2,RCOND,C2)
      T=1.0+RCOND
      IF(T.EQ.1.0) GO TO 90
      DO 2 M=1,NO2
      DO 1 I=1,NO2
1      MU2(I)=(0.D00,0.D00)
      MU2(M)=(1.D00,0.D00)
      CALL ZGESL(B,LDA2,NO2,WA2,MU2,0)
      DO 6 I=1,NO2
6      A(I,J)=MU2(I)
      J=J+1
      DO 2 CONTINUE
      RETURN
90     TYPE*, 'MATRIX IS SINGULAR TO WORKING PRECISION'
      RETURN
      END

```

```

C2345678
      SUBROUTINE DETER(A,WA,NO,C1,RCOND,LDA,COND,DET,WORK)
      REAL*8 RCOND,COND
      COMPLEX*16 A(NO,NO),C1(NO),DET(2),WORK(NO)
      INTEGER WA(NO),LDA2
      LDA2=LDA*2
      CALL ZGECO(A,LDA,NO,WA,RCOND,C1)
      IF(RCOND.EQ.0.0) GO TO 10
      COND=1.0/RCOND
      CALL ZGEDI(A,LDA,NO,WA,DET,WORK,10)
      K=INT(DET(2))
10     TYPE*,COND,DET(1),K

```

RETURN  
END

```

SUBROUTINE BESSEL(Q,JV,L2,NO,H,P1,P3,LA,P1Q,P3Q)
C234567
C    PROGRAMM TO CALCULATE BESSELL FUNCTIONS OF ANY ORDER

COMPLEX*16 JV(0:200),J(0:200),ZO,FAC,Q(NO,LA),P1(NO,NO,LA)
COMPLEX*16 SUM,P3(NO,NO,LA),P1Q(NO,NO,LA),P3Q(NO,NO,LA)
REAL*8 H,PI
INTEGER L2,NO,P,PO,PO1,GAMMA,NU
PI=DACOS(-1.0D00)
DO 100 L=1,L2
DO 100 N=1,NO
DO 100 M=1,NO
ZO=Q(N,L)*H/2.0D00
PO=5
10  J(PO)=((2.7182*ZO/(2.0*PO))**PO)/DSQRT(2.0*PO*PI)
    IF(CDABS(J(PO)).LT.10.0**-15) GO TO 15
    PO=PO+1
    GO TO 10
15  PO1=PO-1
    J(PO1)=((2.7182*ZO/(2.0*PO1))**PO1)/DSQRT(2.0*PO1*PI)
    DO 20 P=PO1,1,-1
    J(P-1)=((2*P/ZO)*J(P))-J(P+1)
20  CONTINUE
    SUM=(0.0D00,0.0D00)
    DO 30 P=1,INT(PO/2)
    SUM=SUM+2*J(2*P)
30  CONTINUE
    FAC=SUM+J(0)
    DO 40 P=0,PO
    JV(P)=J(P)/FAC
40  CONTINUE

    IF(M.LT.N) GO TO 70
    P=M-N
    P3(N,M,L)=JV(P)
    P1(N,M,L)=(-1)**P*JV(P)
    IF(CDABS(Q(N,L)).LT.10.0**-5) GO TO 80
    GO TO 100
70  P=N-M
    P3(N,M,L)=(-1.0)**P*JV(P)
    P1(N,M,L)=JV(P)
75  IF(CDABS(Q(N,L)).LT.10.0**-5) GO TO 80

```

( $\phi_{nm}^-$ : eq. C-5)

( $\phi_{nm}^+$ : eq. C-5)

( $\phi_{nm}^-$ : eq. C-5)

( $\phi_{nm}^+$ : eq. C-5)

```

      GO TO 100

80    IF(M.LT.N) GO TO 90
      P=M-N
      GAMMA=1
      IF(P.EQ.0) GO TO 100
      DO 60 NU=P,1,-1
      GAMMA=GAMMA*NU
60    CONTINUE
      P3Q(N,M,L)=((0.5)**P)*(ZO**(P-1))/GAMMA
      P1Q(N,M,L)=((-1)**P)*((0.5)**P)*(ZO**(P-1))/GAMMA
      GO TO 100

90    P=N-M
      GAMMA=1
      DO 95 NU=P,1,-1
      GAMMA=GAMMA*NU
95    CONTINUE
      P3Q(N,M,L)=((-1)**P)*((0.5)**P)*(ZO**(P-1))/GAMMA
      P1Q(N,M,L)=((0.5)**P)*(ZO**(P-1))/GAMMA

100   CONTINUE
C     TYPE*, 'ZO=', ZO
C     TYPE*, 'N, JV'
C     DO 200 N=0, PO
C     TYPE*, N, JV(N)
C200  CONTINUE
C     DO 300 L=1, L2
C     DO 300 M=1, NO
C     DO 300 N=1, NO
C     TYPE*, 'M, N, L, Q, P1, P3'
C     TYPE*, M, N, L, Q(N, L), P1(N, M, L), P3(N, M, L)
C     TYPE*, 'P1Q, P3Q'
C     TYPE*, P1Q(N, M, L), P3Q(N, M, L)
C300  CONTINUE

      RETURN
      END
      SUBROUTINE IOFile(InUnit, OutUnit, Input_File)

      INTEGER InUnit, Ierr, OutUnit
      CHARACTER*100 Input_File, OutPut_File

C ....Read in the name of the input file....
C

```

```
100  PRINT*, 'Enter in the name of the input file'
      READ(5,50) Input_File
C    WRITE(6,50) Input_File
      OPEN (Unit = InUnit, File = Input_File, Status = 'old',
*       iostat = Ierr)
      IF (Ierr .NE. 0) THEN
        PRINT*, 'Error in opening input file, Ierr = ',Ierr
        GO TO 100
      ENDIF
      PRINT*, 'Enter in the name of the output file'
      READ(5,50) Output_File
      OPEN (Unit = OutUnit, File = OutPut_File, Status = 'New',
*       iostat = Ierr)

50    FORMAT(A100)
      RETURN
      END
```



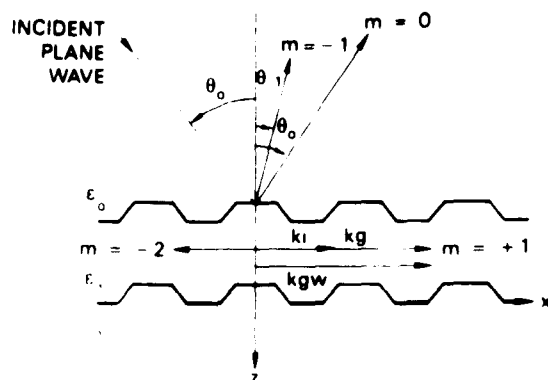


FIGURE 1. Schematic of a Single-Layer Coated Grating With Identical Trapezoidal Profiles at Each Interface. The  $m = 0$  and  $m = -1$  represent the specular and  $-1$  order reflected beams, respectively. The  $m = +1$  and  $m = -2$  orders represent guided waves propagating in the  $+x$  and  $-x$  directions, respectively. The incident beam is at angle  $\theta_0$  and is the  $x$ - $z$  plane.  $\epsilon_0$ ,  $\epsilon_1$ , and  $\epsilon_s$  are the dielectric functions of the superstrate, layer 1, and the substrate, respectively.

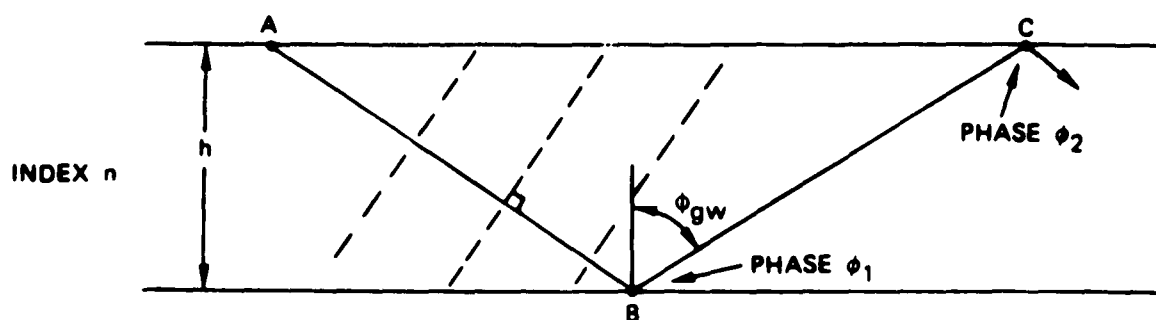


FIGURE 2. Illustration of the Phase Condition  $\phi_1 + \phi_2 + 2\delta = 2\pi m$  for a Single-Layer Planar Waveguide Where the Phase Thickness  $\delta = 2\pi/\lambda_0 n h \cos \theta_{gw}$ .

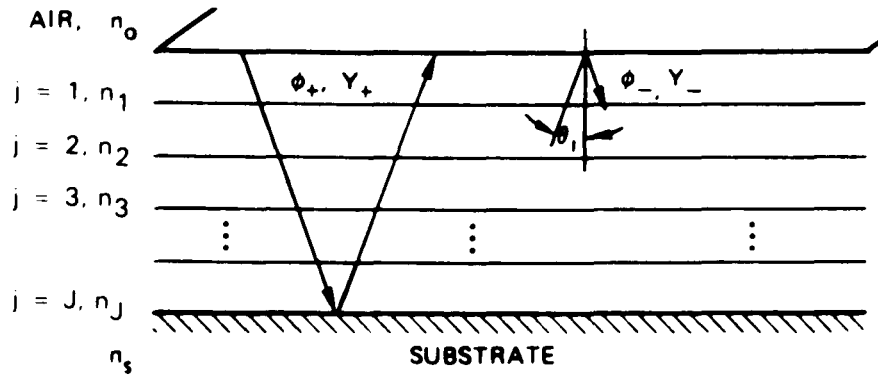


FIGURE 3. Schematic of a Multilayer Assembly Divided at the Surface Boundary and Showing Phase  $\phi$  and Admittance  $Y$  of the Ingoing and Outgoing Waves.

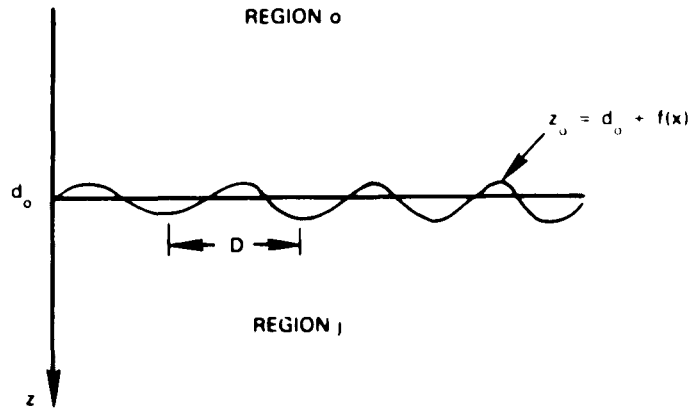
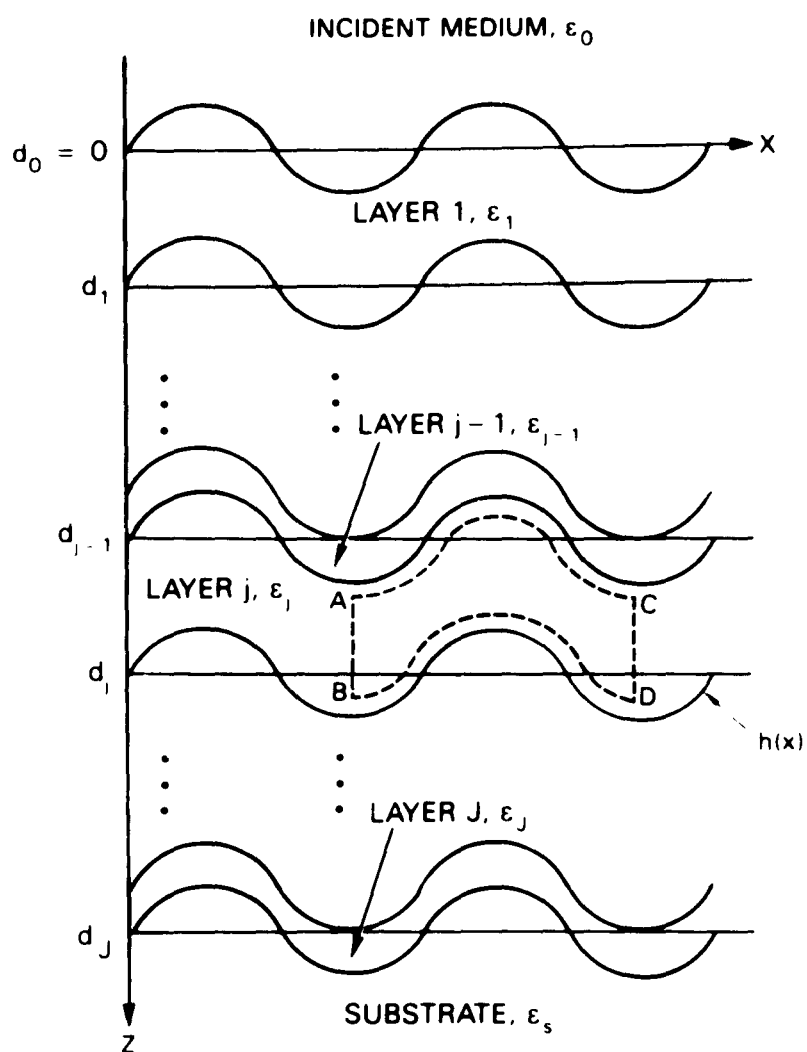
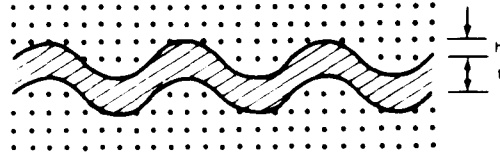


FIGURE 4. Schematic of a Grating Surface of Period  $D$  and With Profile Function  $f(x)$ . Region 0 is the superstrate and  $j$  is the substrate. The mean reference level of the surface is  $d_0$ .



**FIGURE 5.** Schematic Representation of a Multilayer-Coated Sinusoidal Grating. The dashed line indicates the path of integration of Green's theorem in layer  $j$ .



(Figure 2(b) in Reference 64.)

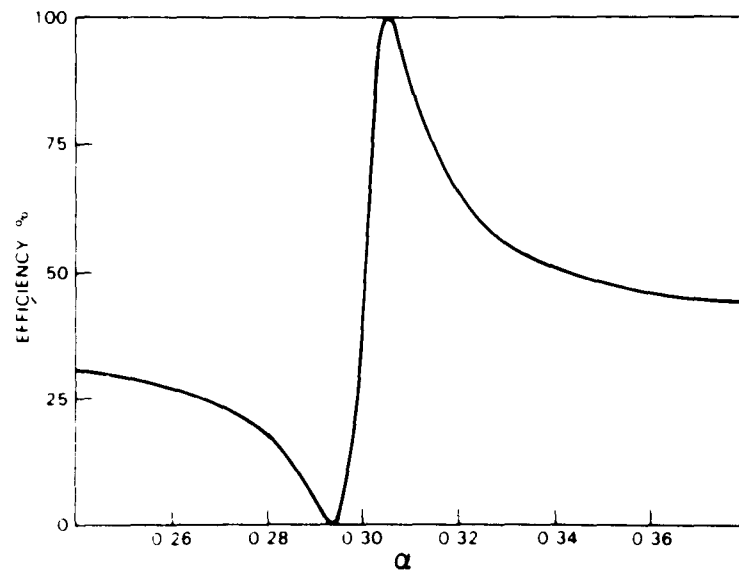


**FIGURE 6(a).** Diffraction Efficiency of the Zeroth Reflected Order of the Sinusoidal Grating, as Shown in Figure 2(b) in Reference 64. Parameters of the system:  $n_1 = n_2 = 1$ ,  $n_3 = 2.3$ ,  $t = 0.19 \mu\text{m}$ ,  $h = 0.04 \mu\text{m}$ ,  $d = 0.37 \mu\text{m}$ , and  $\lambda = 632.8 \text{ nm}$  for TE polarization;  $\alpha = \sin \theta_i$ .

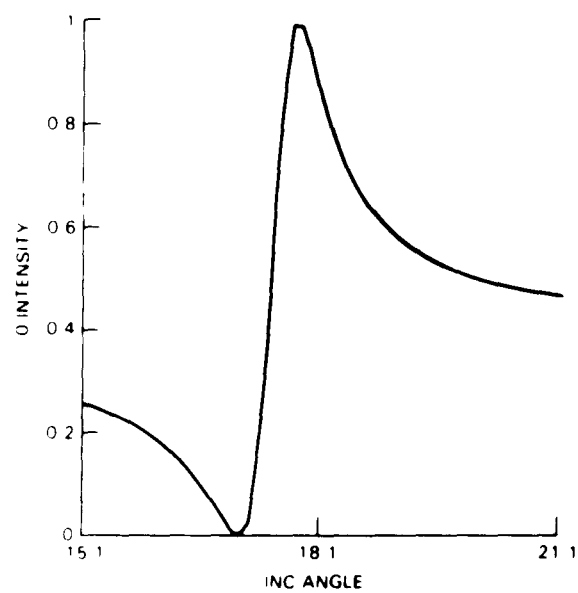


**FIGURE 6(b). Comparison of Extinction Method Calculation Used in This Paper for a Dielectric Waveguide Shown in Figure 6(a).**

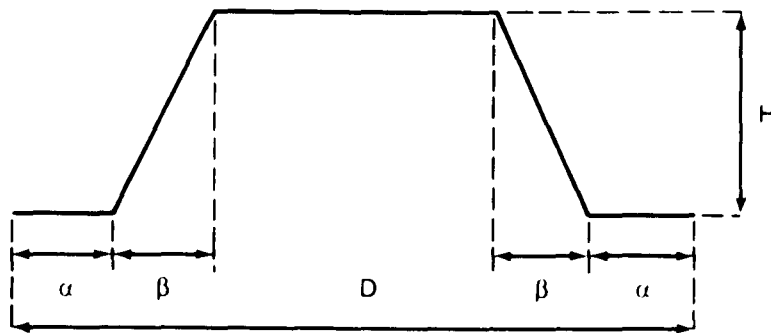


FIGURE 7(a). The Trapezoidal Profile Used in the Numerical Analysis. The period  $D = 0.7 \mu\text{m}$ , where the  $\alpha$  and  $\beta$  values were  $0.05D$  and  $0.1D$ , respectively.

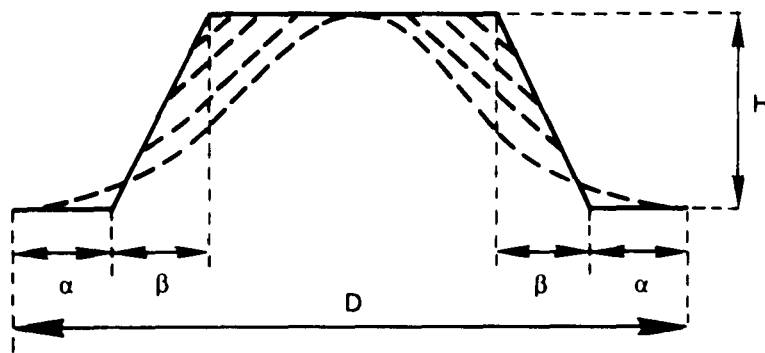


FIGURE 7(b). Rounded Trapezoidal Profile Used in the Numerical Analysis. The period  $D = 0.7 \mu\text{m}$ , where the  $\alpha$  and  $\beta$  values were  $0.05D$  and  $0.1D$ , respectively.

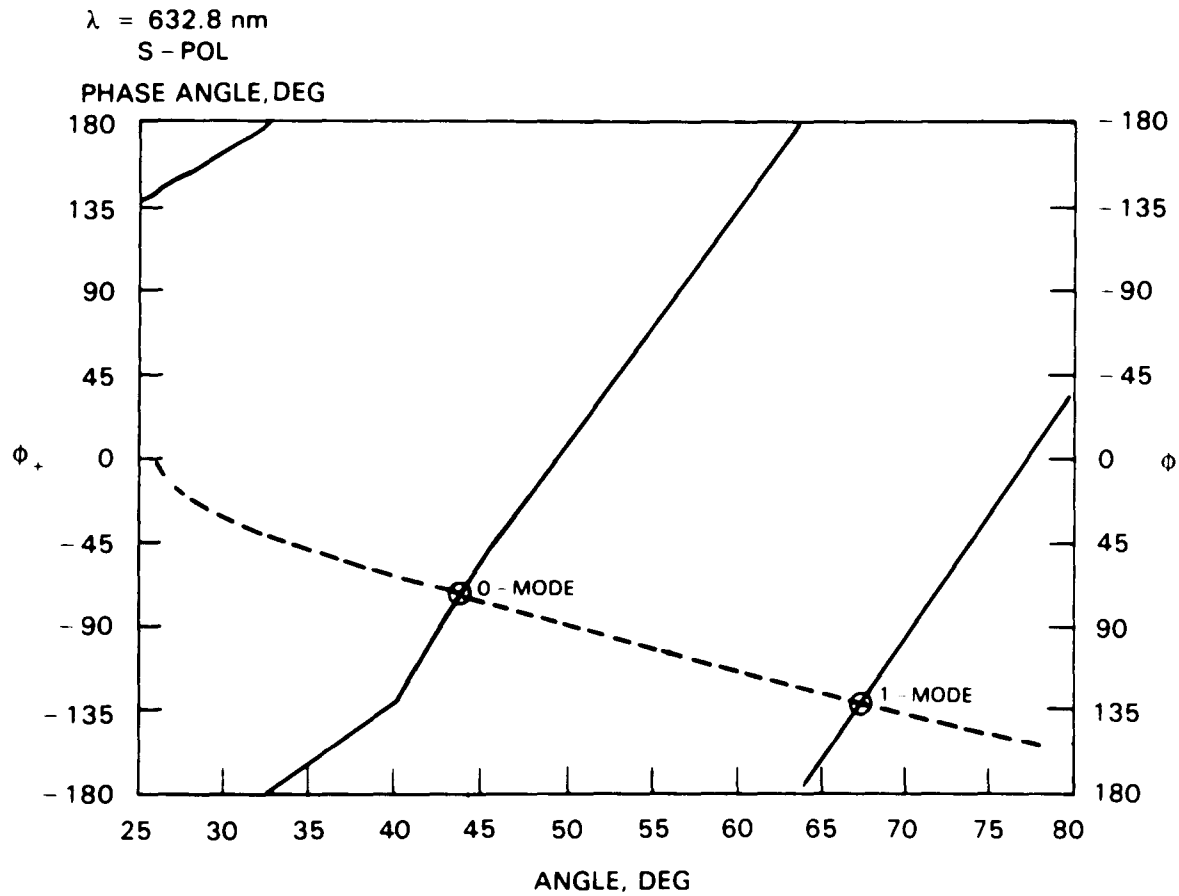


FIGURE 8(a). Phase Plot for the Upward- ( $\phi_-$ ---) and Downward- ( $\phi_+$ —) Traveling Waves. Intersection points determine the guided-wave propagation angles  $\theta_{gw}$  with wave vector  $\omega/c n_1 \sin \theta_{gw}$ : single-dielectric layer ( $\epsilon_1 = 5.11$ , 0.0), thickness  $0.25 \mu\text{m}$ , upon a dielectric substrate ( $\epsilon_s = 2.25$ , 0.0).

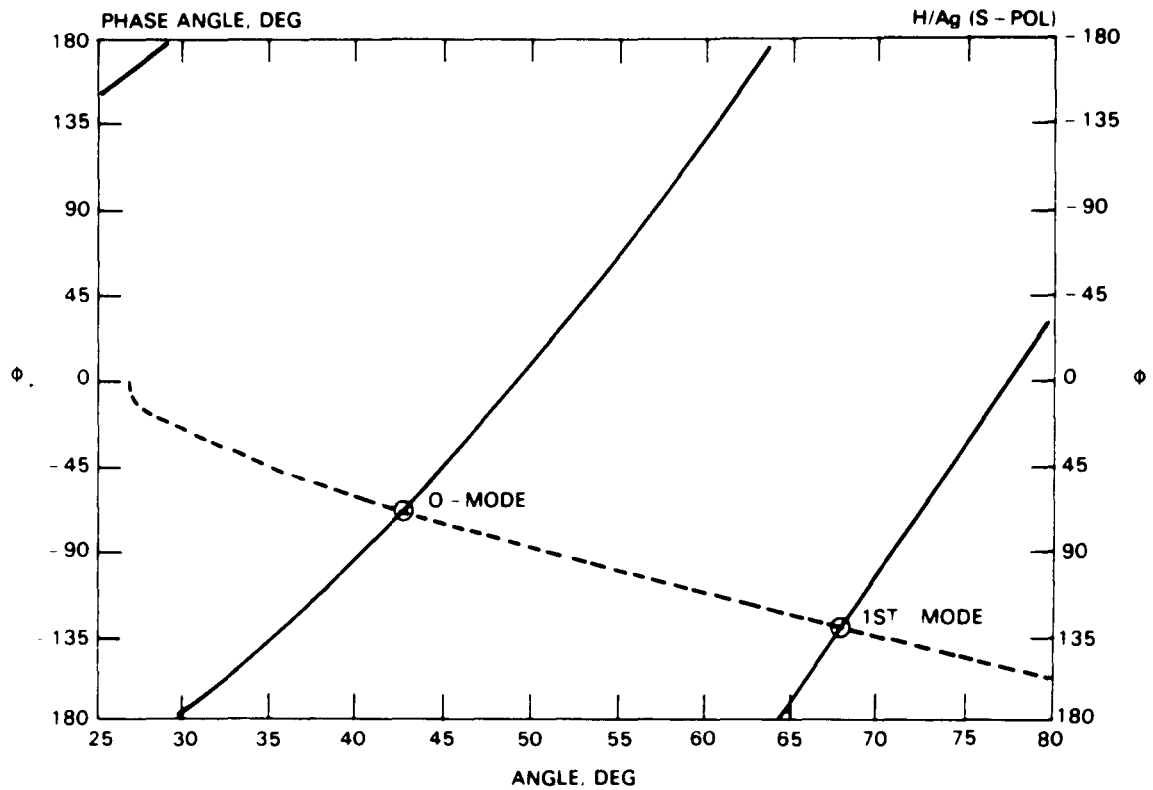


FIGURE 8(b). Phase Plot for the Upward- ( $\phi_+$ ---) and Downward- ( $\phi_-$ —) Traveling Waves. Intersection points determine the guided-wave propagation angles  $\theta_{gw}$  with wave vector  $\omega/c n_1 \sin \theta_{gw}$ : single-dielectric layer ( $\epsilon_1 = 5.11$ , 0.0), thickness  $0.30 \mu\text{m}$ , upon a metallic substrate ( $\epsilon_s = -16.4$ , 0.52).



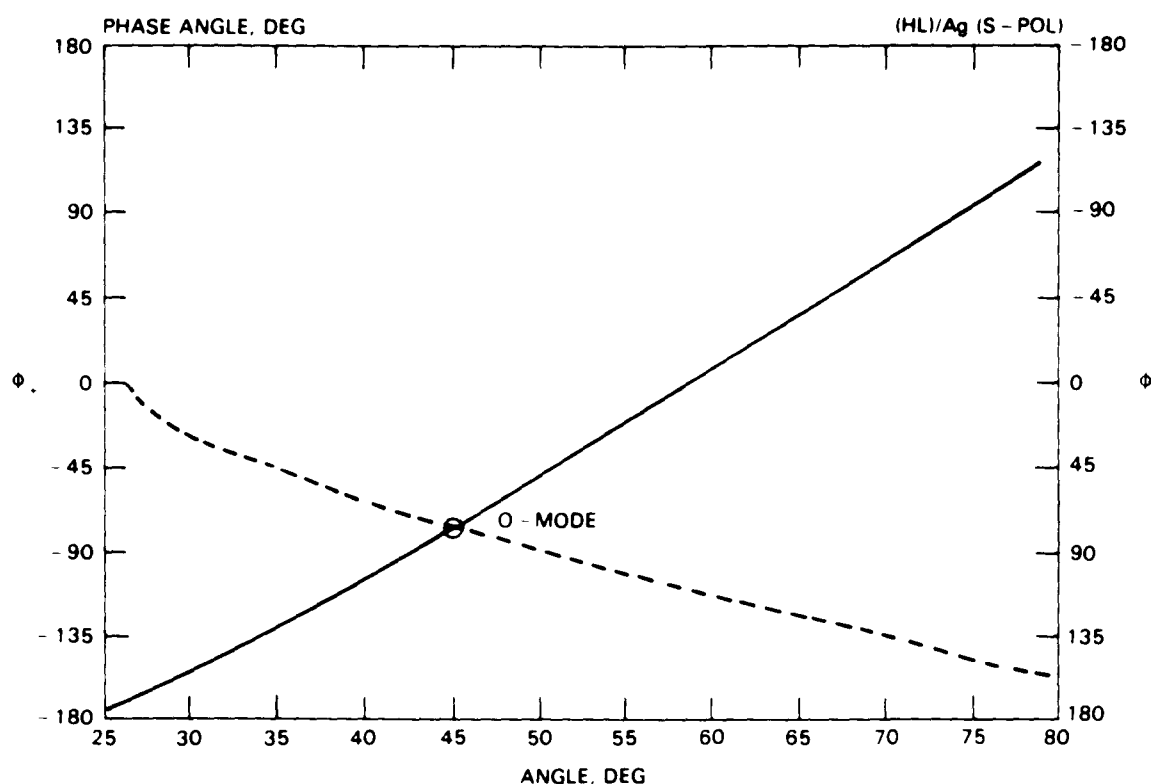


FIGURE 8(c). Phase Plot for the Upward- ( $\phi_-$ ---) and Downward- ( $\phi_+$ —) Traveling Waves. Intersection points determine the guided-wave propagation angles  $\theta_{gw}$  with wave vector  $\omega/c n_1 \sin \theta_{gw}$ : multilayer dielectric of design HL ( $\epsilon_H = 5.11, 0.0$ ;  $\epsilon_L = 2.25, 0.0$ ), quarter-wave optical thickness at  $45^\circ$  angle of incidence, metallic substrate ( $\epsilon_S = -16.4, 0.52$ ).

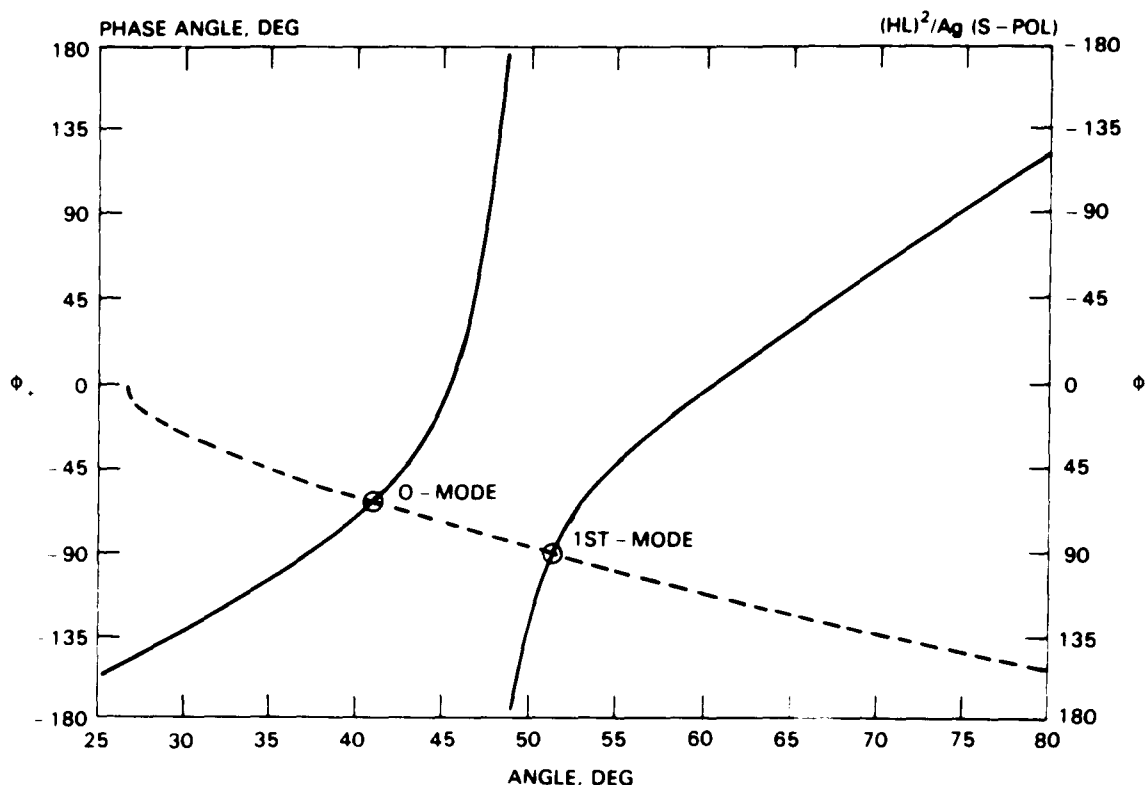


FIGURE 8(d). Phase Plot for the Upward- ( $\phi_-$ ---) and Downward- ( $\phi_+$ —) Traveling Waves. Intersection points determine the guided-wave propagation angles  $\theta_{gw}$  with wave vector  $\omega/c n_1 \sin \theta_{gw}$ : multilayer dielectric of design  $(HL)^2$  ( $\epsilon_H = 5.11, 0.0$ ;  $\epsilon_L = 2.25, 0.0$ ), quarter-wave optical thickness at  $45^\circ$  angle of incidence, metallic substrate ( $\epsilon_S = -16.4, 0.52$ ).

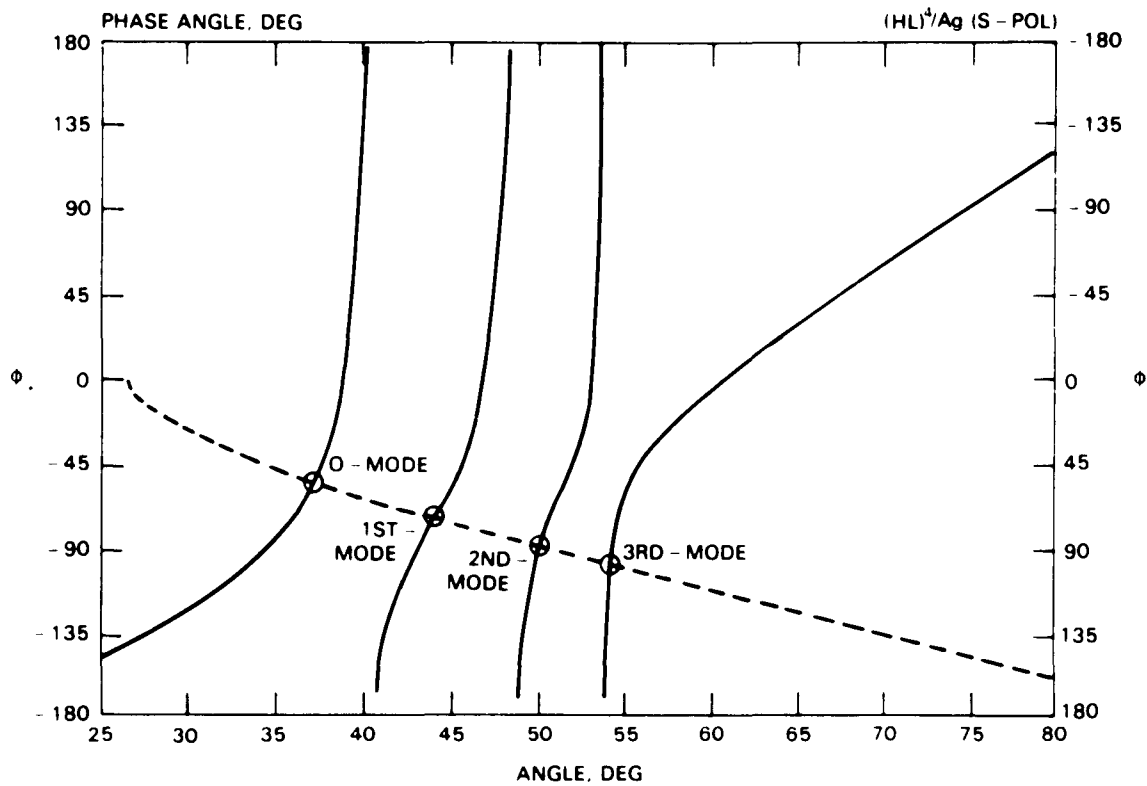


FIGURE 8(e). Phase Plot for the Upward- ( $\phi_-$ ---) and Downward- ( $\phi_+$ —) Traveling Waves. Intersection points determine the guided-wave propagation angles  $\theta_{gw}$  with wave vector  $\omega/c n_1 \sin \theta_{gw}$ : multilayer dielectric of design  $(HL)^4$  ( $\epsilon_H = 5.11, 0.0$ ;  $\epsilon_L = 2.25, 0.0$ ), quarter-wave optical thickness at  $45^\circ$  angle of incidence, metallic substrate ( $\epsilon_S = -16.4, 0.52$ ).

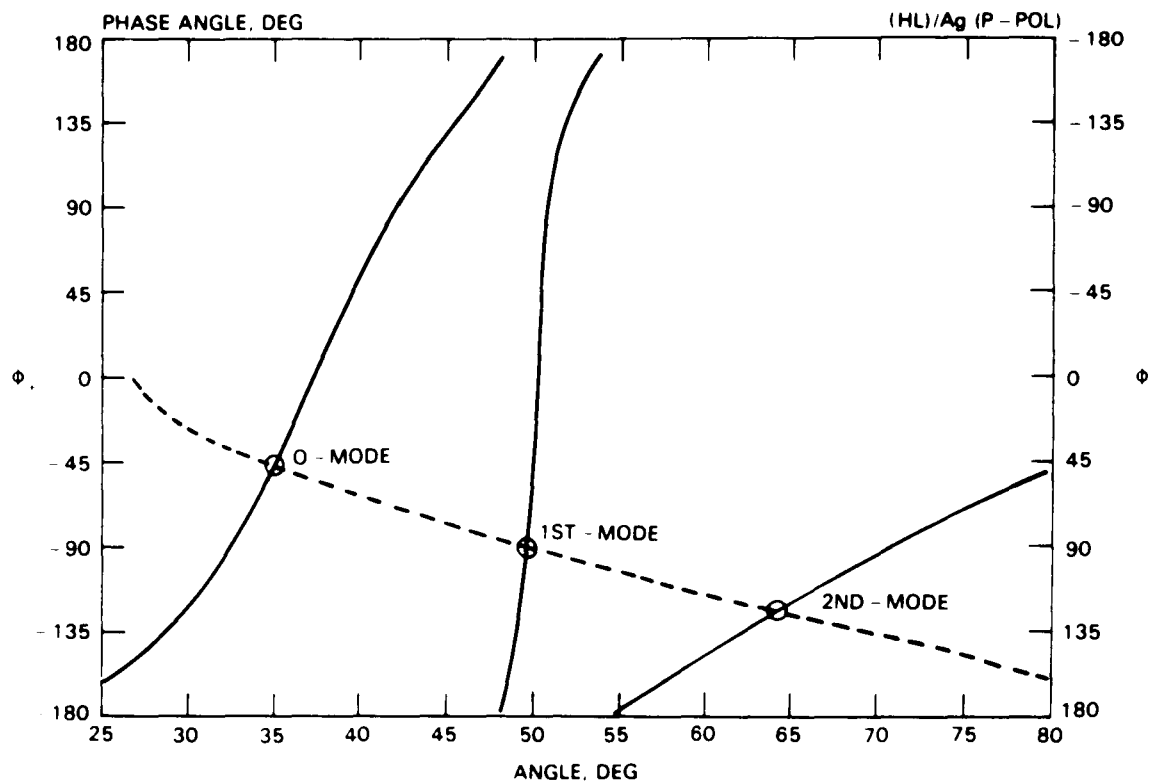


FIGURE 8(f). Phase Plot for the Upward- ( $\phi_-$ ---) and Downward- ( $\phi_+$ —) Traveling Waves. Intersection points determine the guided-wave propagation angles  $\theta_{gw}$  with wave vector  $\omega/c n_1 \sin \theta_{gw}$ : multilayer dielectric of design HL ( $\epsilon_H = 5.11, 0.0$ ;  $\epsilon_L = 2.25, 0.0$ ), quarter-wave optical thickness at  $45^\circ$  angle of incidence, metallic substrate ( $\epsilon_S = -16.4, 0.52$ ).

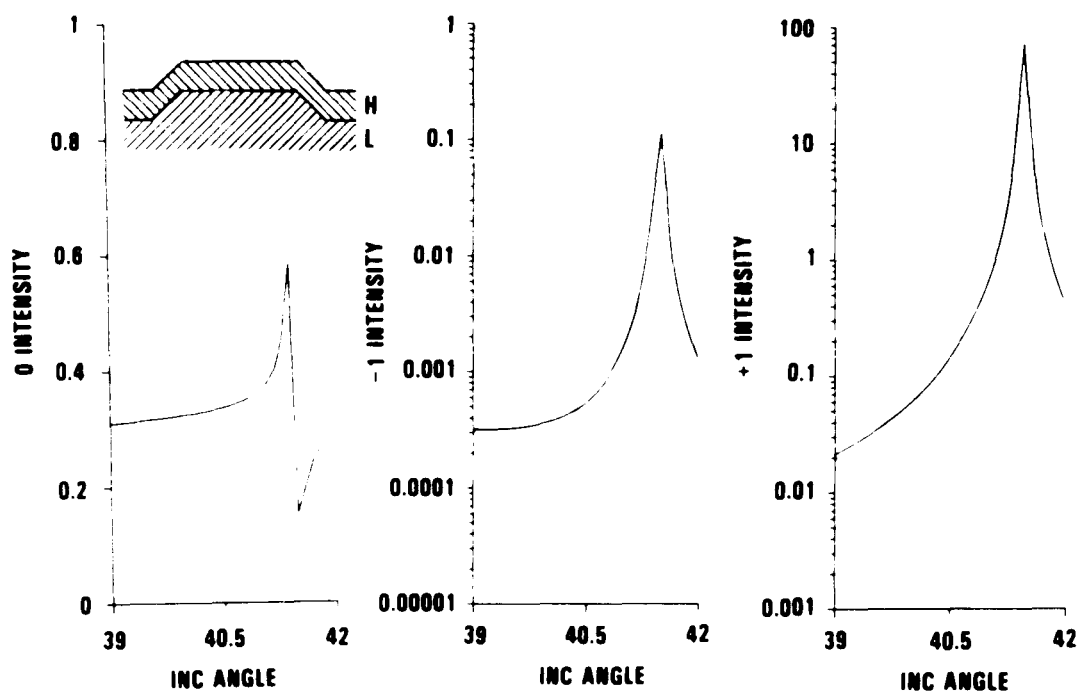


FIGURE 9. Intensity Versus Angle of Incidence for (a) 0 and (b) -1 Order Reflected Beams and (c) +1 Order Coupling to the  $j = 0$  Guided-Wave Mode (H/L: Trapezoid;  $h = 0.01 \mu\text{m}$ ; s-Polarized).

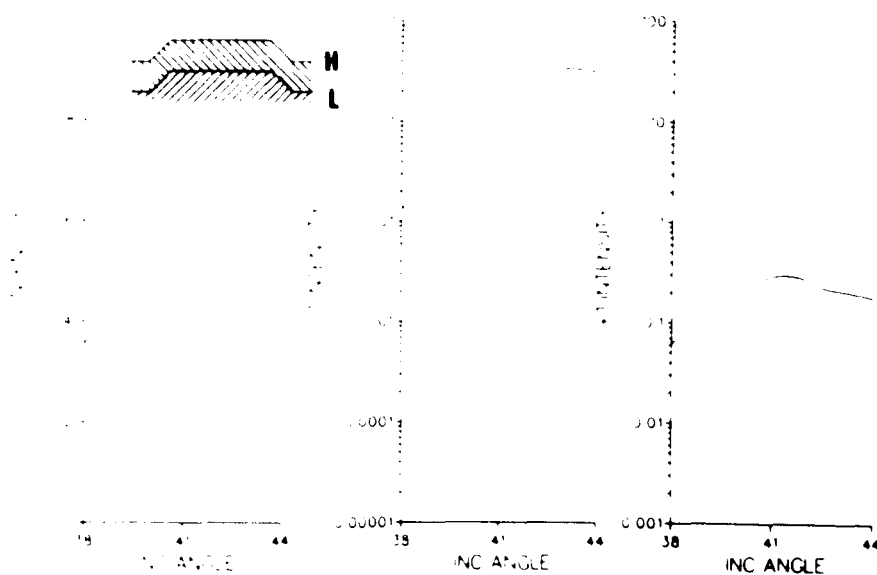


FIGURE 10. Intensity Versus Angle of Incidence for (a) 0 and (b) -1 Order Reflected Beams and (c) +1 Order Coupling to the  $j = 0$  Guided-Wave Mode (H/L: Replicated Trapezoid;  $h = 0.1 \mu\text{m}$ ; s-Polarized).

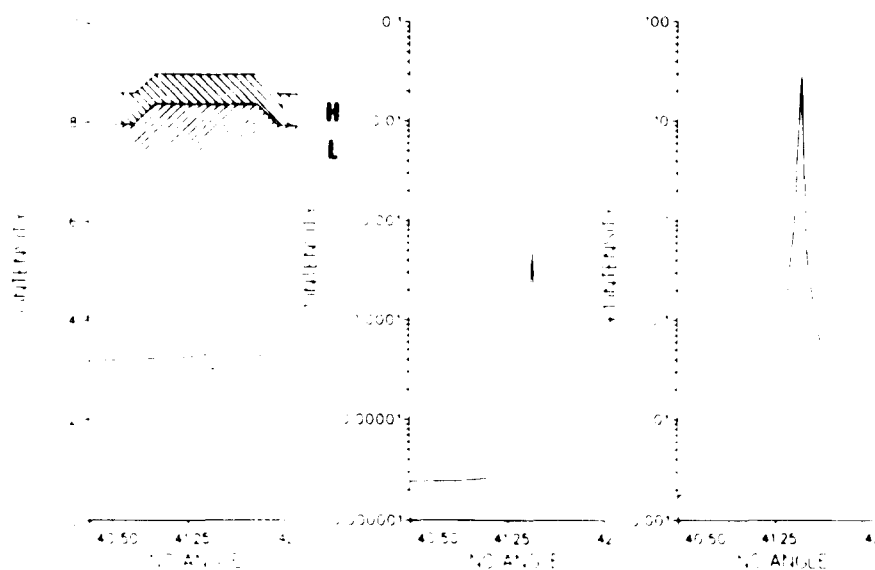


FIGURE 11. Intensity Versus Angle of Incidence for (a) 0 and (b) -1 Order Reflected Beams and (c) +1 Order Coupling to the  $j = 0$  Guided-Wave Mode (H/L: Replicated Trapezoid;  $h = 0.001 \mu\text{m}$ ; s-Polarized).

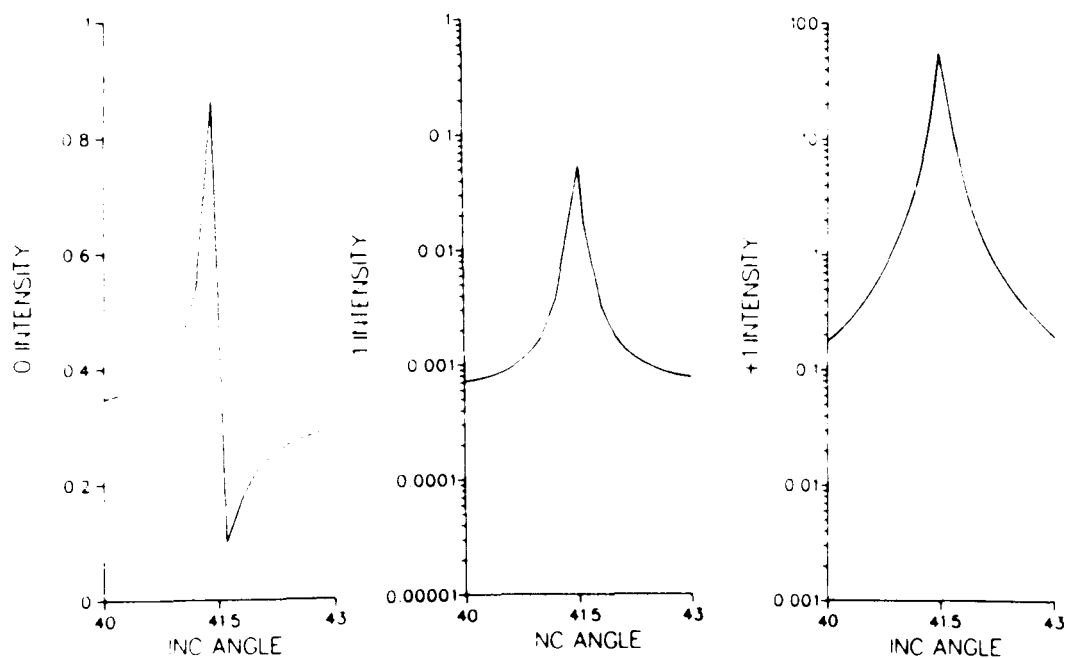


FIGURE 12. Intensity Versus Angle of Incidence for (a) 0 and (b) -1 Order Reflected Beams and (c) +1 Order Coupling to the  $j = 0$  Guided-Wave Mode (H/L: Rectangle;  $h = 0.01 \mu\text{m}$ ; 40% Duty Cycle; s-Polarized).

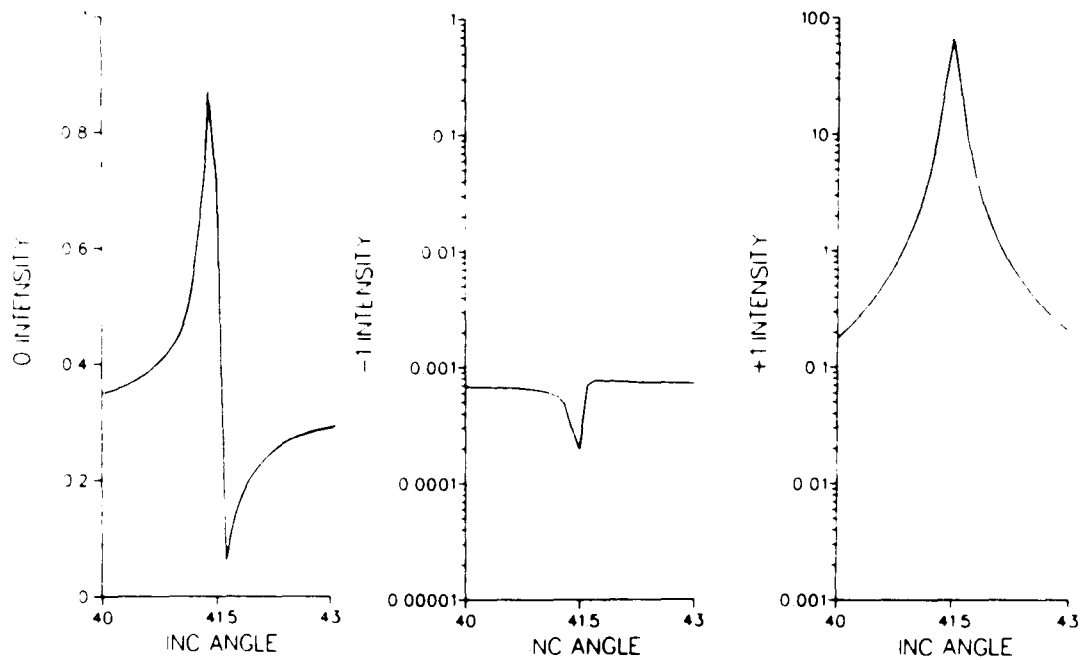


FIGURE 13. Intensity Versus Angle of Incidence for (a) 0 and (b) -1 Order Reflected Beams and (c) +1 Order Coupling to the  $j = 0$  Guided-Wave Mode (H/L: Rectangle;  $h = 0.01 \mu\text{m}$ ; 50% Duty Cycle; s-Polarized).

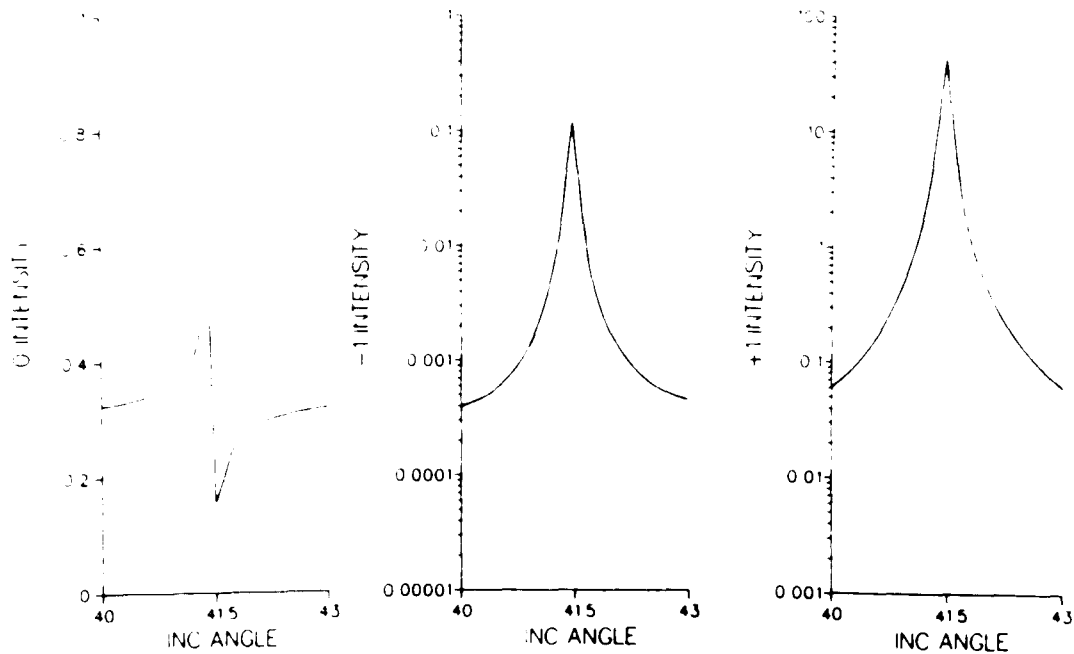
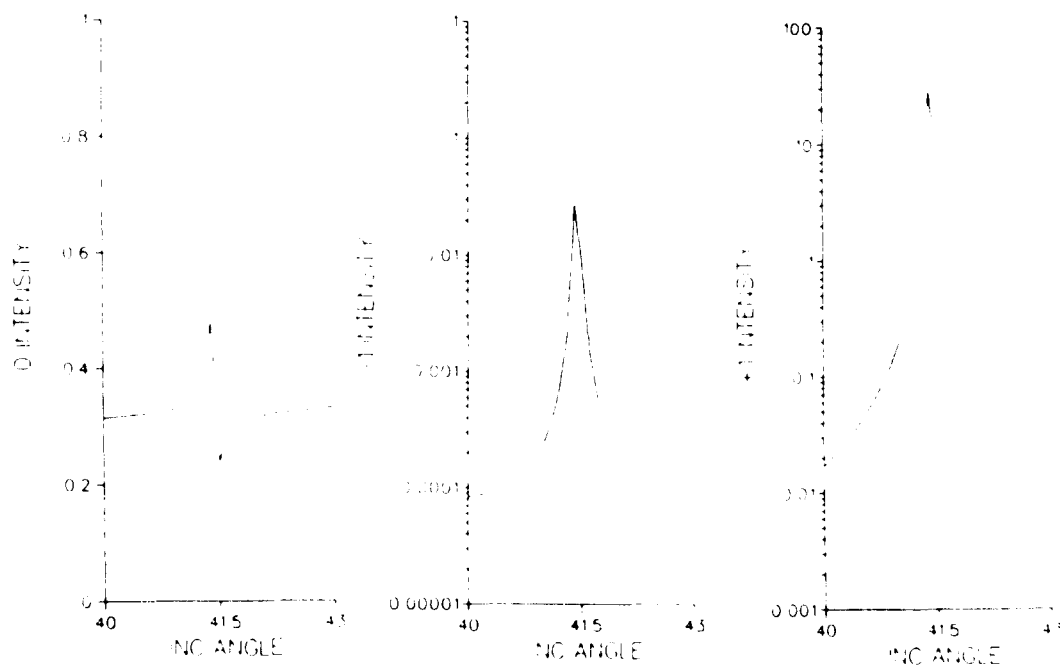
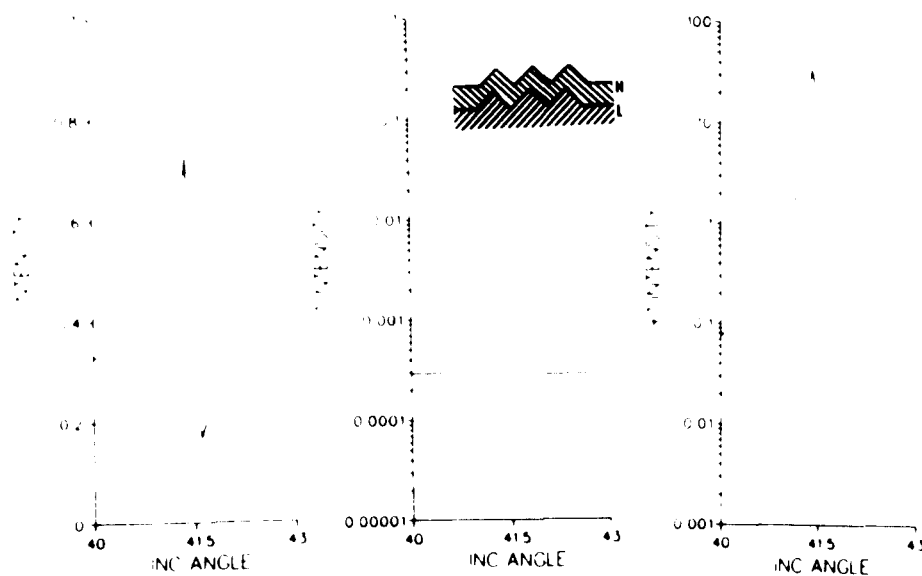


FIGURE 14. Intensity Versus Angle of Incidence for (a) 0 and (b) -1 Order Reflected Beams and (c) +1 Order Coupling to the  $j = 0$  Guided-Wave Mode (H/L: Rectangle;  $h = 0.01 \mu\text{m}$ ; 80% Duty Cycle; s-Polarized).



**FIGURE 15. Intensity Versus Angle of Incidence for (a) 0 and (b) -1 Order Reflected Beams and (c) +1 Order Coupling to the  $j = 0$  Guided-Wave Mode (H/L: Rectangle;  $h = 0.01 \mu\text{m}$ ; 90% Duty Cycle; s-Polarized).**



**FIGURE 16. Intensity Versus Angle of Incidence for (a) 0 and (b) -1 Order Reflected Beams and (c) +1 Order Coupling to the  $j = 0$  Guided-Wave Mode (H/L: Triangle;  $h = 0.01 \mu\text{m}$ ; s-Polarized).**



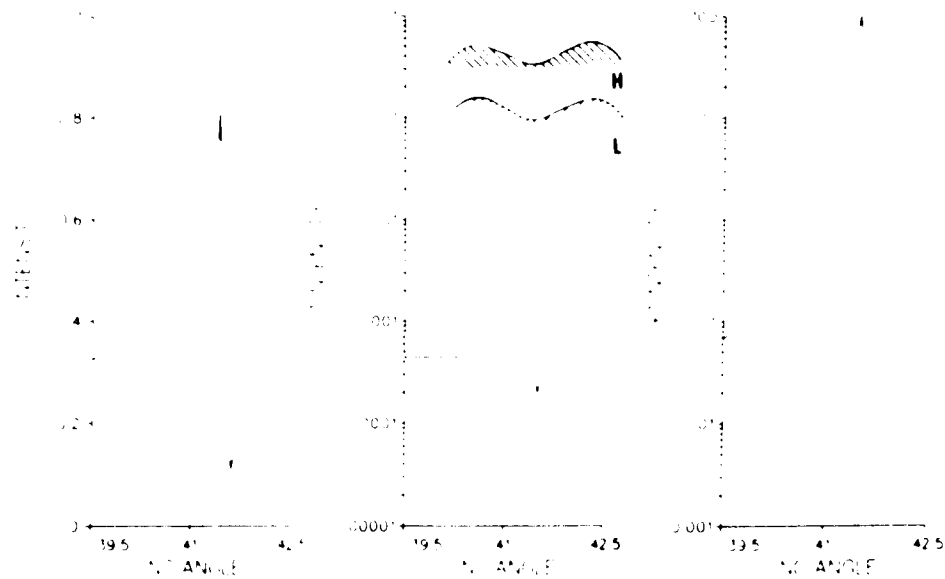


FIGURE 17. Intensity Versus Angle of Incidence for (a) 0 and (b) -1 Order Reflected Beams and (c) +1 Order Coupling to the  $j = 0$  Guided-Wave Mode (H/L: Replicating Sinusoidal;  $h = 0.01 \mu\text{m}$ ; s-Polarized).

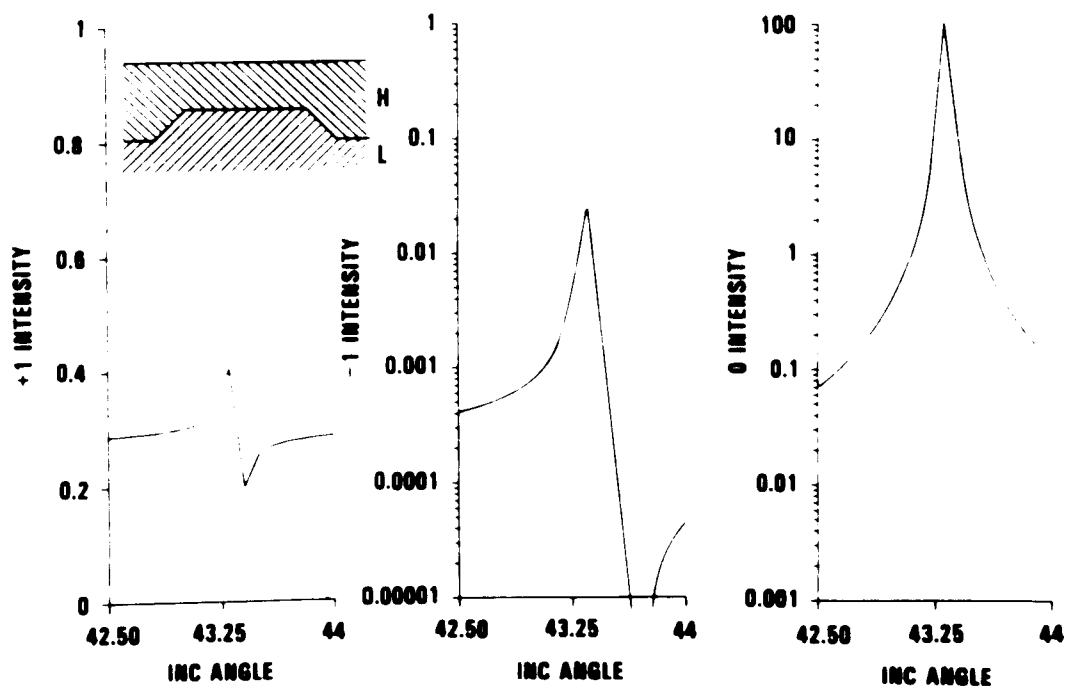


FIGURE 18. Intensity Versus Angle of Incidence for (a) 0 and (b) -1 Order Reflected Beams and (c) +1 Order Coupling to the  $j = 0$  Guided-Wave Mode (H/L: Nonreplicating Trapezoid;  $h = 0, h = 0.01 \mu\text{m}$ ; s-Polarized).

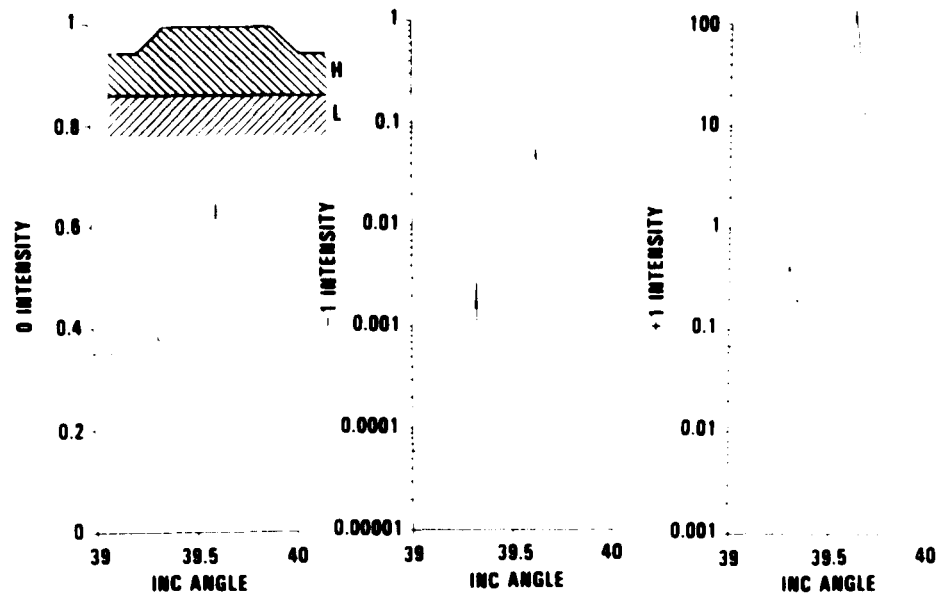


FIGURE 19. Intensity Versus Angle of Incidence for (a) 0 and (b) -1 Order Reflected Beams and (c) +1 Order Coupling to the  $j = 0$  Guided-Wave Mode (H/L: Nonreplicating Trapezoid;  $h = 0.01$ ,  $h = 0$   $\mu\text{m}$ ; s-Polarized).

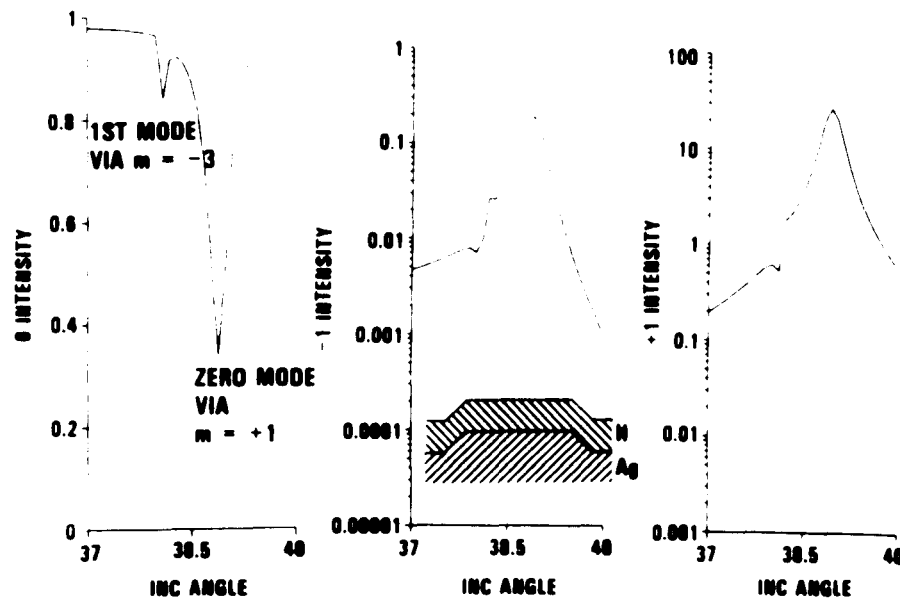


FIGURE 20. Intensity Versus Angle of Incidence for (a) 0 and (b) -1 Order Reflected Beams and (c) +1 Order Coupling to the  $j = 0$  Guided-Wave Mode (H/ $A_g$ : Replicating Trapezoid;  $h = 0.01$   $\mu\text{m}$ ; s-Polarized).

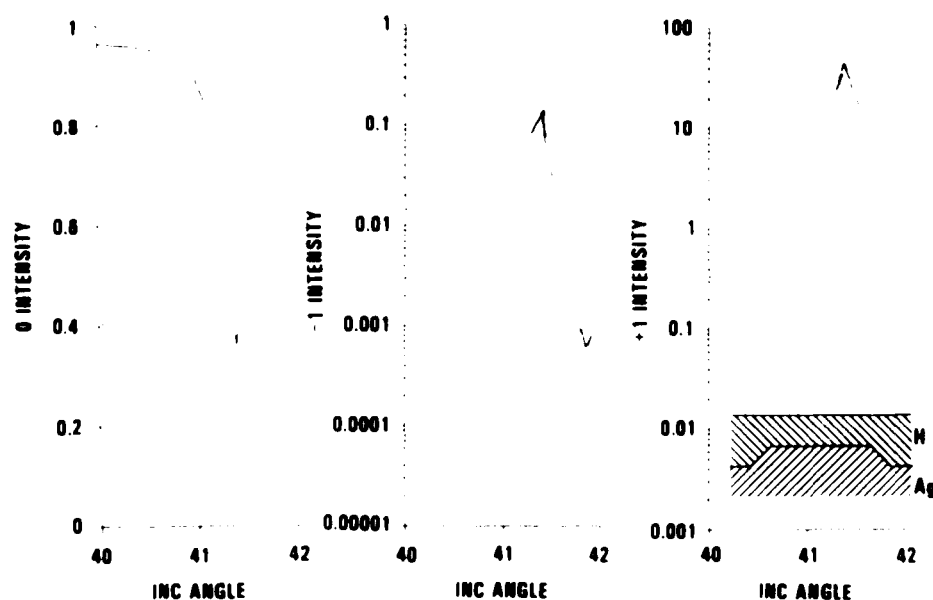


FIGURE 21. Intensity Versus Angle of Incidence for (a) 0 and (b) -1 Order Reflected Beams and (c) +1 Order Coupling to the  $j = 0$  Guided-Wave Mode ( $H/A_g$ : Nonreplicating Trapezoid;  $h = 0$ ,  $h = 0.01 \mu\text{m}$ , s-Polarized).

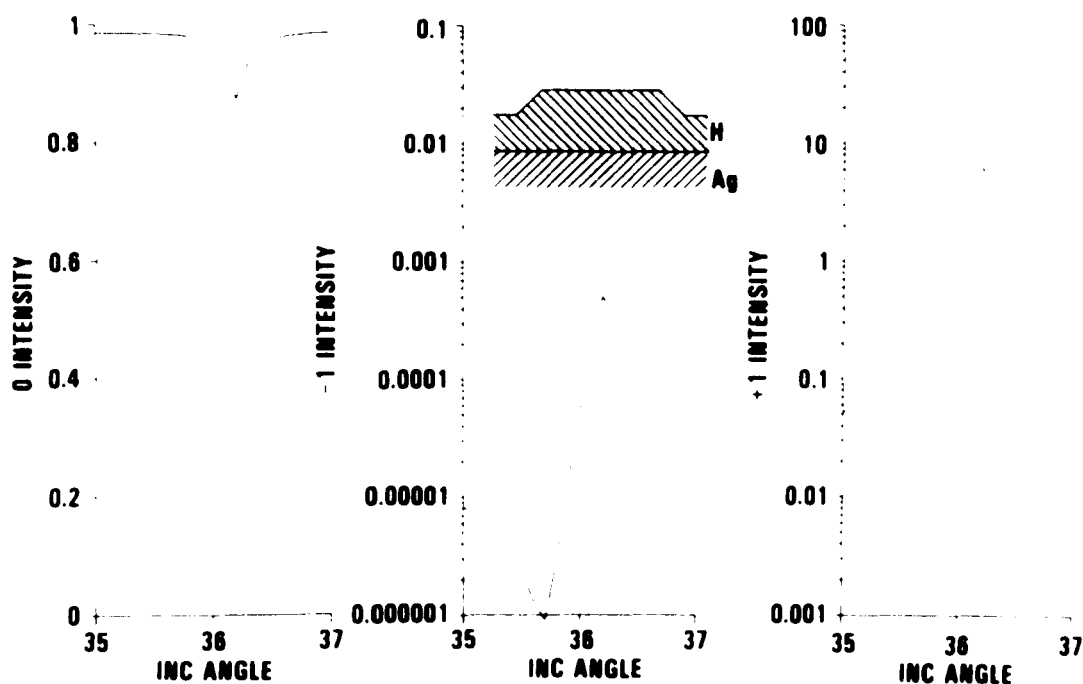


FIGURE 22. Intensity Versus Angle of Incidence for (a) 0 and (b) -1 Order Reflected Beams and (c) +1 Order Coupling to the  $j = 0$  Guided-Wave Mode ( $H/A_g$ : Nonreplicating Trapezoid;  $h = 0.01$ ,  $h = 0 \mu\text{m}$ ; s-Polarized).

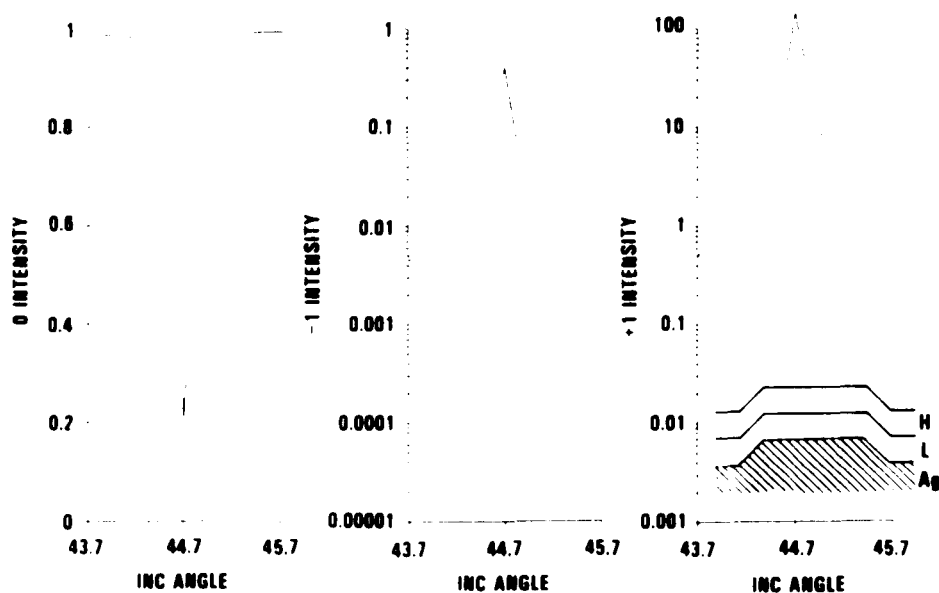


FIGURE 23. Intensity Versus Angle of Incidence for (a) 0 and (b) -1 Order Reflected Beams and (c) +1 Order Coupling to the  $j = 0$  Guided-Wave Mode (HL/Ag: Replicating Trapezoid;  $h = 0.01 \mu\text{m}$ ; s-Polarized).

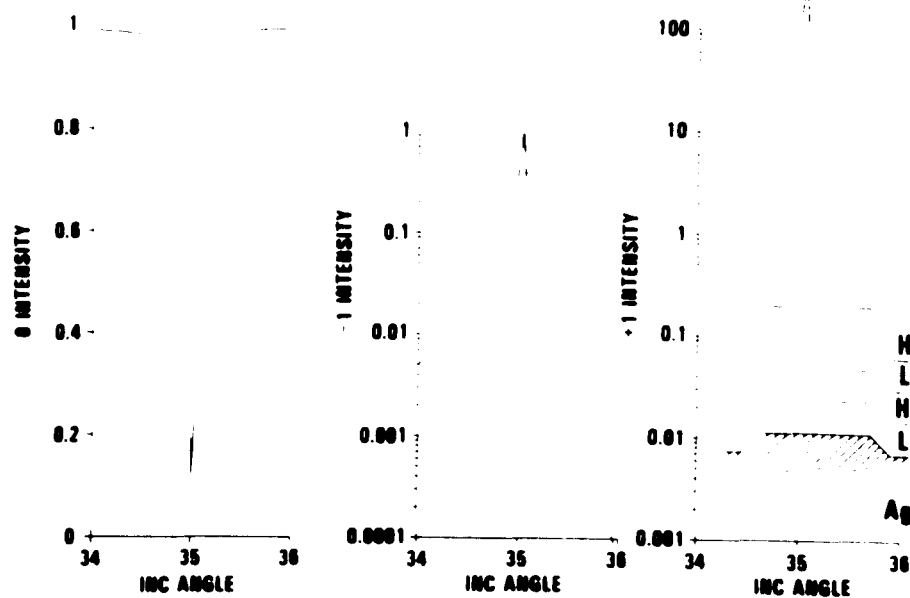


FIGURE 24. Intensity Versus Angle of Incidence for (a) 0 and (b) -1 Order Reflected Beams and (c) +1 Order Coupling to the  $j = 0$  Guided-Wave Mode  $[(HL)^2/Ag]$ : Replicating Trapezoid;  $h = 0.01 \mu\text{m}$ ; s-Polarized].

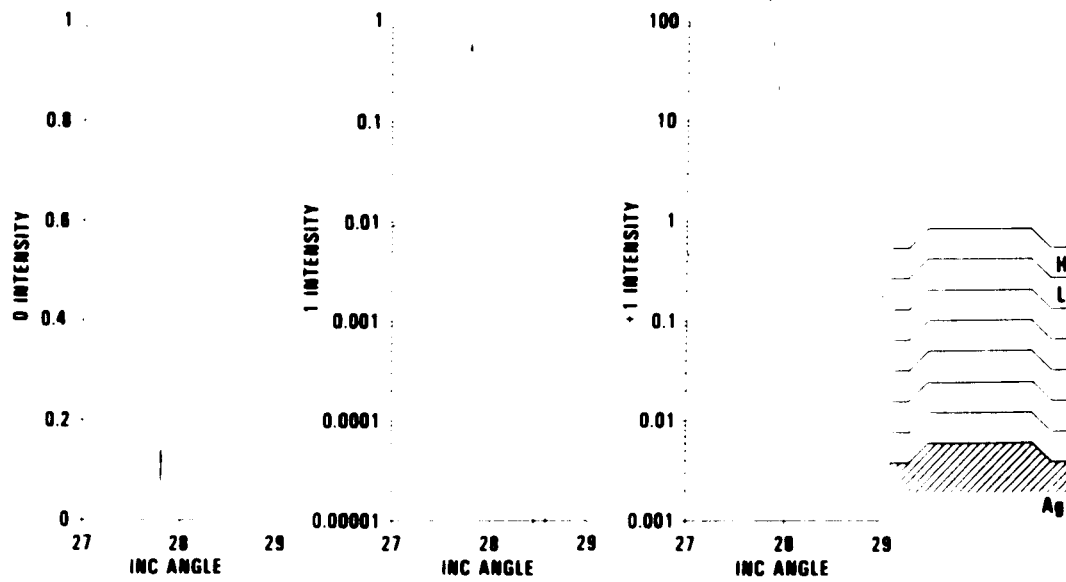


FIGURE 25. Intensity Versus Angle of Incidence for (a) 0 and (b) -1 Order Reflected Beams and (c) +1 Order Coupling to the  $j = 0$  Guided-Wave Mode  $[(HL)^4/Ag]$ : Replicating Trapezoid;  $h = 0.01 \mu\text{m}$ ; s-Polarized].

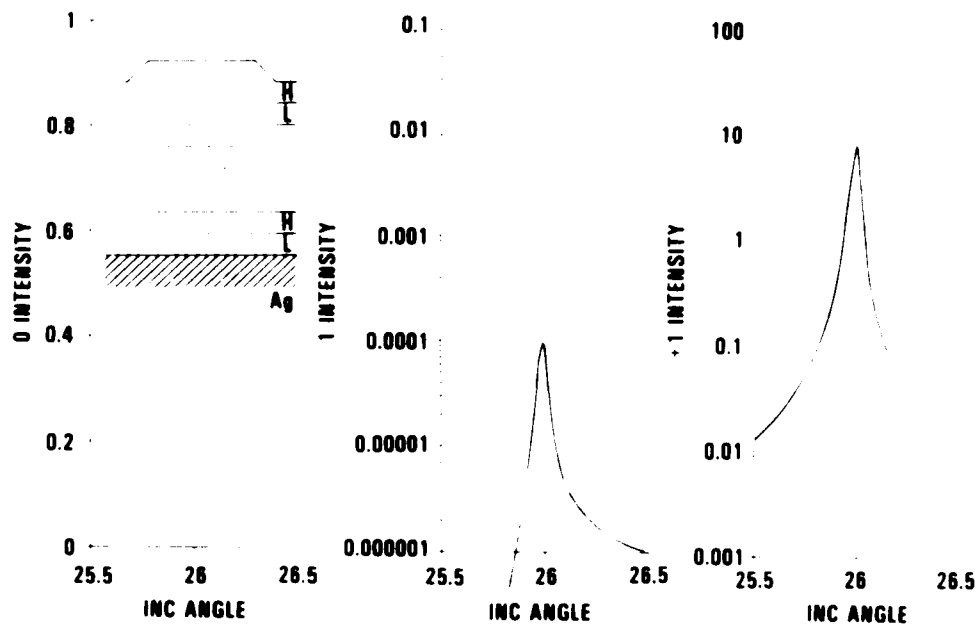


FIGURE 26. Intensity Versus Angle of Incidence for (a) 0 and (b) -1 Order Reflected Beams and (c) +1 Order Coupling to the  $j = 0$  Guided-Wave Mode  $[(HL)^4/Ag$ : Trapezoid on Surface;  $h = 0.01 \mu\text{m}$ ; s-Polarized].

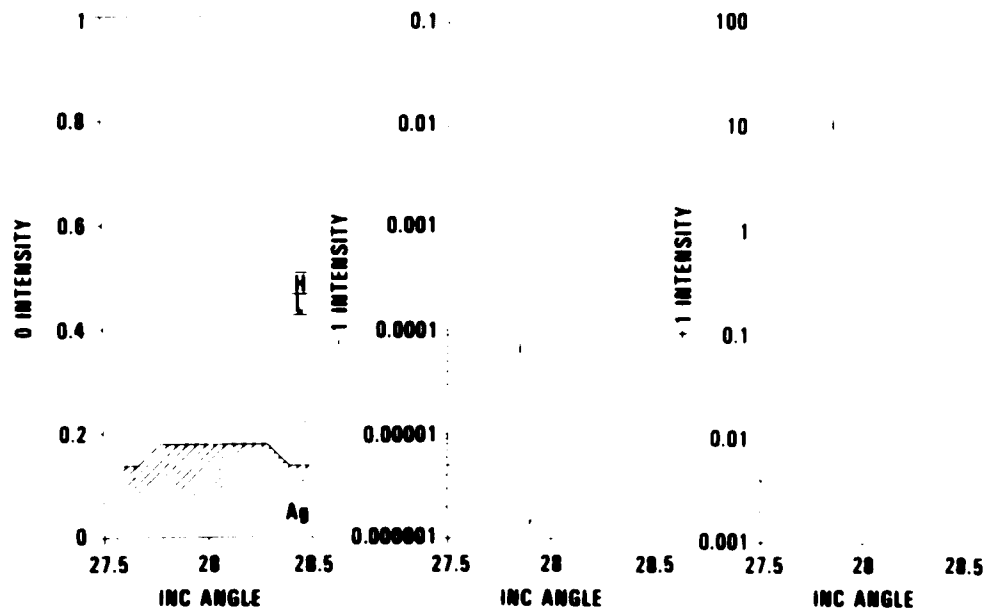


FIGURE 27. Intensity Versus Angle of Incidence for (a) 0 and (b) -1 Order Reflected Beams and (c) +1 Order Coupling to the  $j = 0$  Guided-Wave Mode  $[(HL)^4/Ag$ : Trapezoid on Substrate;  $h = 0.01 \mu\text{m}$ ; s-Polarized].

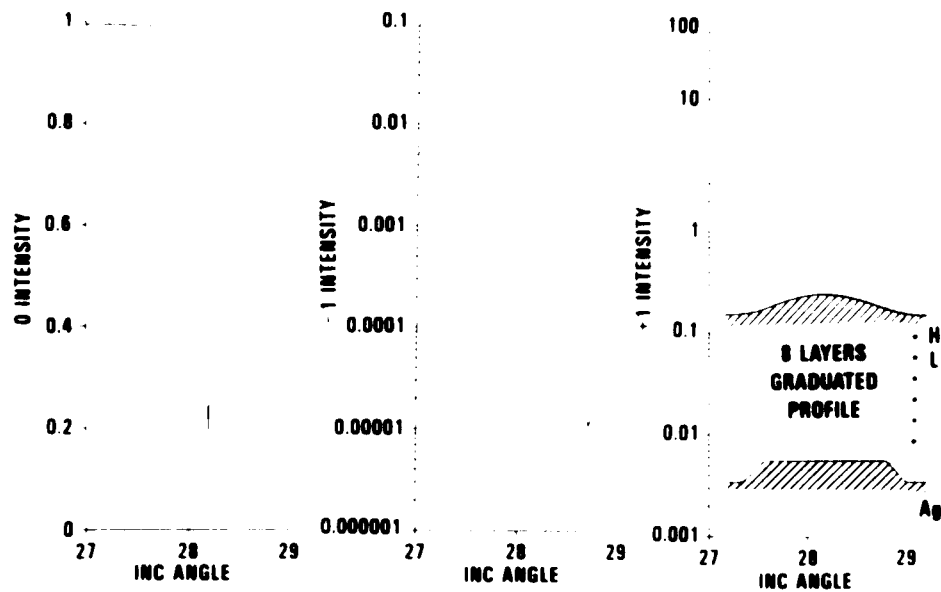


FIGURE 28. Intensity Versus Angle of Incidence for (a) 0 and (b) -1 Order Reflected Beams and (c) +1 Order Coupling to the  $j = 0$  Guided-Wave Mode  $[(HL)^4/Ag$ : Rounded Trapezoid;  $h = 0.01 \mu\text{m}$ ; s-Polarized].

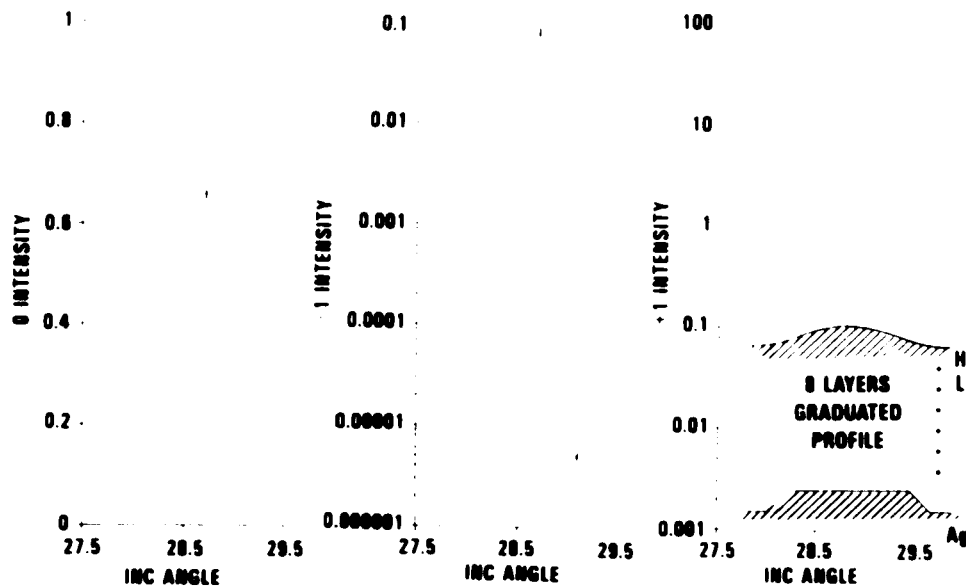


FIGURE 29. Intensity Versus Angle of Incidence for (a) 0 and (b) -1 Order Reflected Beams and (c) +1 Order Coupling to the  $j = 0$  Guided-Wave Mode  $[(HL)^4/Ag$ : Rounded Trapezoid;  $h = 0.01, 0.009, 0.008, 0.007, 0.006, 0.005, 0.004, 0.003, 0.002 \mu\text{m}$ ; s-Polarized].

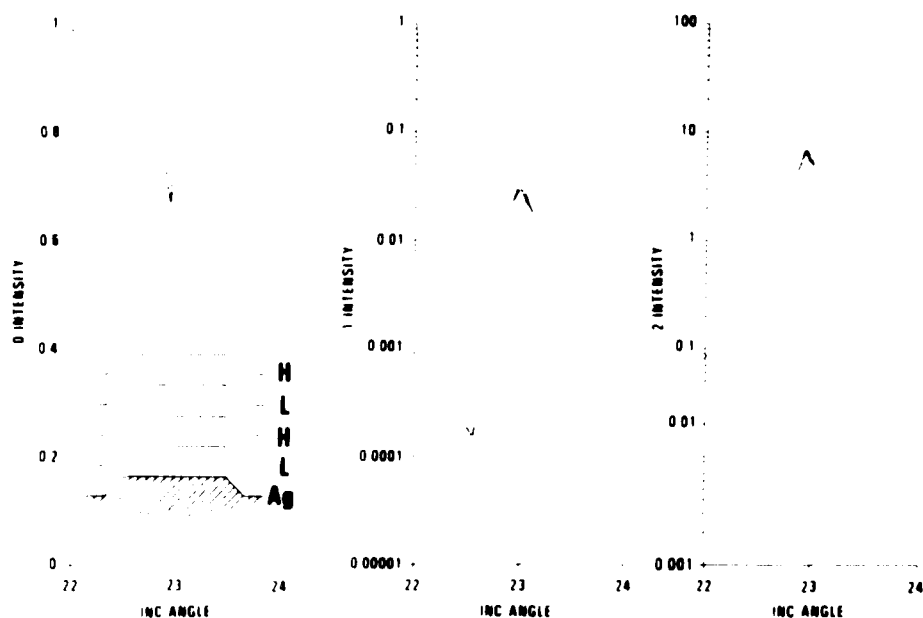


FIGURE 30. Intensity Versus Angle of Incidence for (a) 0 and (b) -1 Order Reflected Beams and (c) +1 Order Coupling to the  $j = 0$  Guided-Wave Mode [ $(HL)^2/Ag$ : Replicated Trapezoid;  $h = 0.01 \mu\text{m}$ ; p-Polarized].

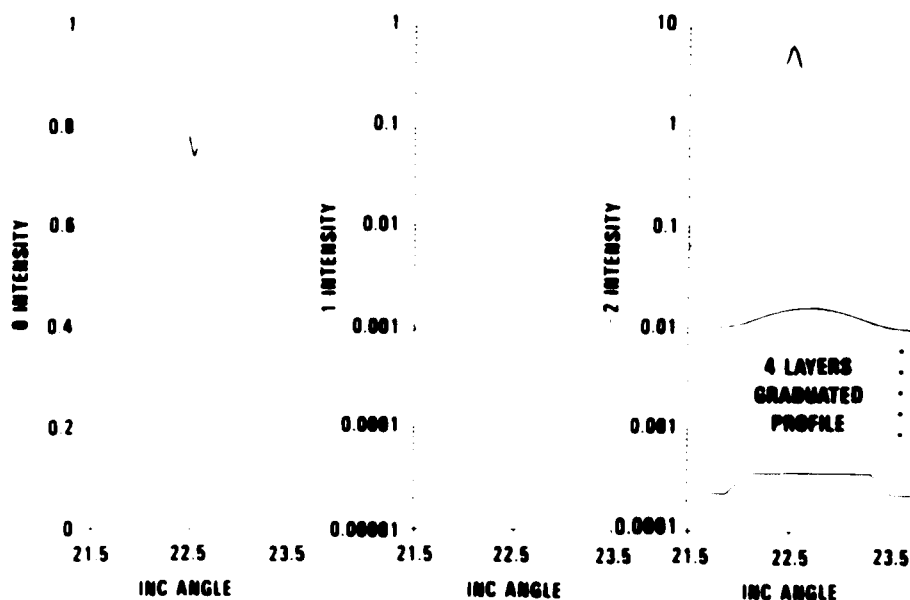


FIGURE 31. Intensity Versus Angle of Incidence for (a) 0 and (b) -1 Order Reflected Beams and (c) +1 Order Coupling to the  $j = 0$  Guided-Wave Mode [ $(HL)^2/Ag$ : Rounded Trapezoid;  $h = 0.006, 0.007, 0.008, 0.009, 0.01 \mu\text{m}$ ; p-Polarized].



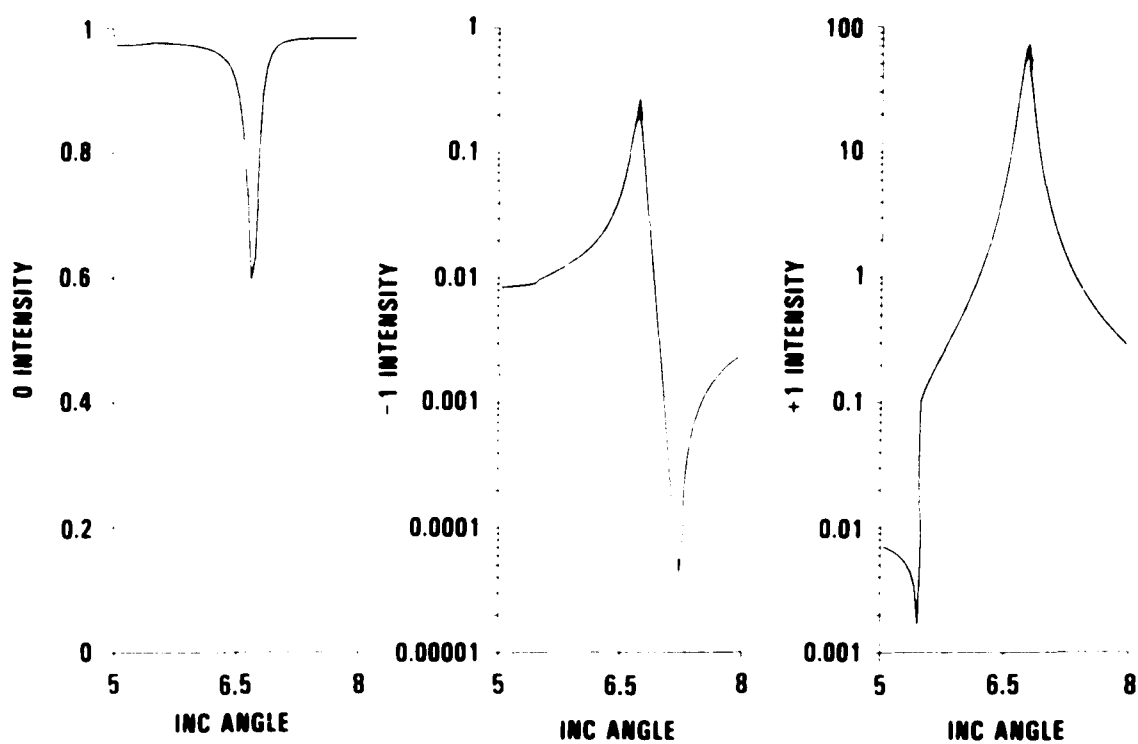


FIGURE 32. Efficiency Calculations in the 0, -1, and +1 Diffracted Order for a Single-Layer Coated Grating. Coating and grating characteristics are given in the text.

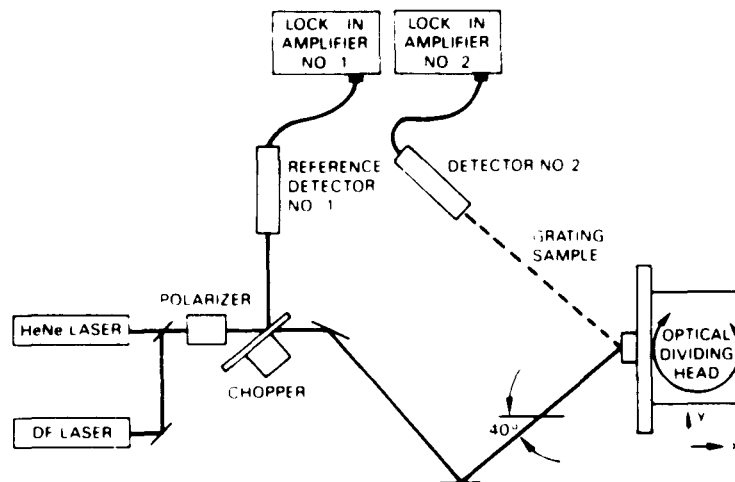


FIGURE 33. Experimental Arrangement Used for Making Coupling Efficiency Measurements. The optical dividing head is rotated to change the angle of incidence. Detector No. 2 is moved by hand and realigned to measure the diffraction efficiency.

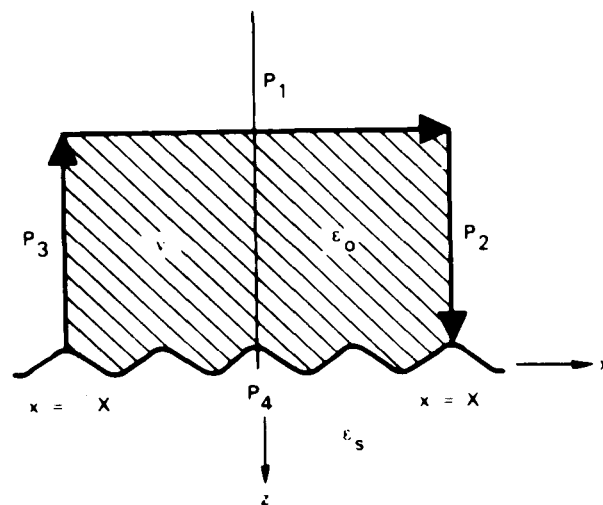
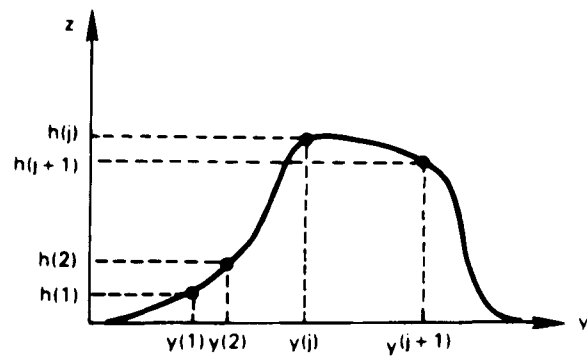


FIGURE 34. Contour of Integration  $C = P_1 + P_2 + P_3 + P_4$  Enclosing Volume  $V$  Used to Evaluate Surface Integral Appearing in Green's Theorem Equation (A-1).



**FIGURE 35. Geometry Considered for Calculation of Matrix Elements: Point-to-Point Integration Method.**

## REFERENCES

1. Lord Rayleigh, "On the Dynamic Theory of Gratings," *Phil. Mag.* *14*, No. 60, 399-416 (1907).
2. F. Toigo, A. Marvin, V. Celli, and N. R. Hill, "Optical Properties of Rough Surfaces: General Theory and the Small Roughness Limit," *Phys. Rev.* *B15*, No. 12, 5618-5626 (1977).
3. J. M. Elson, L. F. DeSandre, and J. L. Stanford, "Analysis of Anomalous Resonance Effects in Multilayer-Overcoated, Low-Efficiency Gratings," *J. Opt. Soc. Am.* *5*, 74-88 (1988).
4. J. M. Elson, L. F. DeSandre, P. C. Archibald, and J. L. Stanford, *Comparison of Theory and Experiment of Anomalous Resonance Effects Associated With a Nine-Layer Overcoated Low-Efficiency Grating* (Naval Weapons Center Technical Publication 6783, 1986).
5. R. W. Wood, "Anomalous Diffraction Gratings," *Phys. Rev.* *48*, 928-936 (1935).
6. A. Hessel and A. A. Oliner, "A New Theory of Wood's Anomalies in Grating Spectrophotometers," *Appl. Opt.* *4*, No. 10, 421-429 (1965).
7. J. E. Stewart and W. S. Gallaway, "Diffraction Anomalies in Grating Spectrophotometers," *Appl. Opt.* *4*, No. 10, 421-429 (1962).
8. M. C. Hutley, "An Experimental Study of the Anomalies of Sinusoidal Diffraction Gratings," *Opt. Acta* *20*, No. 8, 607-624 (1973).
9. R. C. McPhedran and M. D. Waterworth, "A Theoretical Demonstration of Properties of Grating Anomalies (s-Polarization)," *Opt. Acta* *19*, No. 11, 977-892 (1972).
10. V. Twersky, *Inst. Radio Engrs. Trans.*, *AP-43*, 330 (1965).
11. R. Petit, ed., *Electromagnetic Theory of Gratings* (Springer-Verlag, New York, 1980).
12. M. C. Hutley, *Diffraction Gratings* (Academic Press, New York, 1982), p. 178.
13. See for example, J. W. Goodman, *Introduction to Fourier Optics*, Chapter 3 (McGraw-Hill, New York, 1968).
14. R. W. Wood, *Phil. Mag.* *43*, 310 (1912).
15. R. W. Wood, *Phys. Rev.* *48*, 934 (1935).

16. U. Fano, "The Theory of Anomalous Diffraction Gratings and Quasi-Stationary Waves on Metallic Surfaces (Sommerfeld's Waves)." *J. Opt. Soc. Am.* **31**, 213-222 (1941).
17. K. Artmann, *Z. Phys.* **119**, 529 (1942).
18. R. Depine, J. M. Simon, and M. C. Simon, "Diffraction Grating Anomalies: An Experimental Study of Phase Shifts and Resonances," *Opt. Acta* **25**, No. 9, 895-904 (1978).
19. M. C. Hutley and V. M. Bird, "A Detailed Experimental Study of the Anomalies of a Sinusoidal Diffraction Grating," *Opt. Acta* **20**, No. 10, 771-782 (1973).
20. C. Harvey Palmer, "Diffraction Grating Anomalies," *J. Opt. Soc. Am.* **42**, No. 4, 269-276 (1952).
21. C. Harvey Palmer, "Diffraction Gratings Anomalies. II. Coarse Gratings," *J. Opt. Soc. Am.* **46**, No. 1, 50-53 (1956).
22. B. A. Lippmann, *J. Opt. Soc. Am.* **43**, 408 (1953).
23. V. Twersky, "On a Multiple Scattering Theory of the Finite Grating and the Wood Anomalies," *J. Appl. Phys.* **23**, No. 10, 1099-1118 (1952).
24. R. Petit and M. Cadilhac, "M. Sur la Diffraction d'une Onde Plane Par un Réseau Infinit Conducteur," *C. R. Acad. Sci. Paris, Sér. A-B* **262**, 468-471 (1966).
25. R. F. Millar, "On the Rayleigh Assumption in Scattering by a Periodic Surface," *Proc. Comb. Phil. Soc.* **65**, 773-791 (1969).
26. R. F. Millar, "On the Rayleigh Assumption in Scattering by a Periodic Surface," *Proc. Comb. Phil. Soc.* **69**, 217-225 (1971).
27. P. M. van der Berg and J. T. Fokkema, "The Rayleigh Hypothesis in the Theory of Reflection by a Grating," *J. Opt. Soc. Am.* **69**, No. 1, 27-31 (1979).
28. H. Ikuno and K. Yasuura, "Improved Point-Matching Method With Applications to Scattering From a Periodic Surface," *IEEE Trans. Antennas Propag.* **AP-21**, 657-662 (1973).
29. A. Wirgin, *Opt. Acta* **27**, 1671 (1980).
30. A. Wirgin, *Opt. Acta* **28**, 1377 (1980).
31. R. Petit and M. Cadilhac, *C. R. Acad. Sci. Paris* **259**, 2077 (1964).
32. A. Wirgin, *Rev. Opt.* **9**, 449 (1964).
33. J. L. Uretski, *Ann. Phys.* **33**, 400 (1965).

34. J. Pavageau and J. Bousquet, *Opt. Acta* 17, 469 (1970).
35. R. C. McPhedran and D. Maystre, "A Detailed Theoretical Study of the Anomalies of a Sinusoidal Diffraction Grating," *Opt. Acta* 21, No. 5, 413-421 (1974).
36. D. Maystre and R. Petit, *Opt. Commun.* 4, No. 25 (1971).
37. J. Strong, "Effect of Evaporated Films on Energy Distribution in Gratings," *Spectra. Phys. Rev.* 49, 291-296 (1936).
38. J. Hagglund and F. Sellberg, "Reflection, Absorption, and Emission of Light by Opaque Optical Grating," *J. Opt. Soc. Am.* 56, No. 8, 1031-1040 (1966).
39. D. Maystre, *Opt. Commun.* 6, 50 (1972).
40. D. Maystre, *Opt. Commun.* 8, 216 (1973).
41. P. C. Waterman, "Scattering by Periodic Surfaces," *J. Acoust. Soc. Am.* 57, No. 4 (1975).
42. N. E. Glass, M. Weber, and D. L. Mills, "Attenuation and Dispersion of Surface Polaritons on Gratings," *Phys. Rev. B* 29, No. 12, 6548-6559 (15 June 1984).
43. N. E. Glass, R. Loudon, and A. A. Maradudin, "Propagation of Rayleigh Surface Waves Across a Large-Amplitude Grating," *Phys. Rev. B* 24, No. 12, 6843-6861 (1981).
44. B. Laks, D. L. Mills, and A. Maradudin, "Surface Polariton on Large-Amplitude Gratings," *Phys. Rev. B* 23, No. 10, 4965-4976 (1981).
45. R. H. Ritchie, *Phys. Rev.* 166, 874 (1957).
46. R. H. Ritchie, E. T. Arakawa, J. J. Cowan, and R. N. Hamm, "Surface-Plasmon Resonance Effect in Grating Diffraction," *Phys. Rev. Lett.* 21, No. 22, 1530-1533 (1968).
47. E. Kroger and E. Kretschmann, "Surface Plasmon and Polariton Dispersion at Rough Boundaries," *Phys. Status Solidi B* 76, 515-523 (1976).
48. R. Reinisch and M. Neviere, "Surface Polaritons Along a Grating: A Linear Electromagnetic Study," *J. Opt. (Paris)* 13, No. 2, 81-87 (1982).
49. N. E. Glass, M. Weber, and D. L. Mills, "Attenuation and Dispersion of Surface Polaritons on Gratings," *Phys. Rev. B* 29, No. 12, 6548-6558 (1984).
50. I. Pockrand and H. Raether, "Surface Plasma Oscillations at Sinusoidal Silver Surfaces," *Appl. Opt.* 16, No. 7, 1784-1786 (1977).

51. H. Raether, "Dispersion Relation of Surface Plasmons on Gold and Silver Gratings," *Opt. Commun.* 42, No. 4, 217-222 (1977).
52. E. H. Rosengart and I. Pockrand, "Influence of Higher Harmonics of a Grating on the Intensity Profile of the Diffraction Orders Via Surface Plasmons," *Opt. Lett.* 1, No. 6, 194-195 (1977).
53. W. Rothballer, "The Influence of Surface Plasma Oscillations on the Diffraction Orders of Sinusoidal Surface Gratings," *Opt. Commun.* 20, No. 3, 429-433 (1977).
54. T. K. Gaylord and M. G. Mohanan, "Analysis and Applications of Optical Diffraction by Gratings," *Proc. IEEE* 73, No. 5, 894-937 (May 1985).
55. J. J. Cowan and E. T. Arakawa, "Dispersion of Surface Plasmons in Dielectric-Metal Coatings on Concave Diffraction Gratings," *Z. Phys.* 235, 97-109 (1970).
56. M. C. Hutley, J. F. Verrill, and R. C. McPhedran, "The Effect of a Dielectric Layer on the Diffraction Anomalies of an Optical Grating," *Opt. Commun.* 11, No. 2 (1974).
57. M. Neviere, R. Petit, and M. Cadilhac, *Opt. Commun.* 8, 113 (1973).
58. M. Neviere, in *Electromagnetic Theory of Gratings*, R. Petit, ed. (Springer-Verlag, New York, 1980), p. 101.
59. D. Maystre, "A New General Theory for Dielectric Coated Gratings," *J. Opt. Soc. Am.* 68, No. 4, 490-495 (1978).
60. D. Maystre, "A New Theory of Multiprofile, Buried Gratings," *Opt. Commun.* 26, No. 2, 127-132 (1978).
61. D. Maystre, in *Electromagnetic Theory of Gratings*, R. Petit, ed. (Springer-Verlag, New York, 1980), p. 63.
62. L. Mashev and E. Popov, "Diffraction Efficiency Anomalies of Multicoated Dielectric Gratings," *Opt. Commun.* 51, No. 3, 131-136 (1984).
63. L. Mashev and E. Popov, "Zero Order Anomaly of Dielectric Coated Gratings," *Opt. Commun.* 55, No. 6, 377-380 (1985).
64. E. Popov, L. Mashev, and D. Maystre, "Theoretical Study of the Anomalies of Coated Dielectric Gratings," *Opt. Acta* 33, No. 5, 607-619 (1986).
65. L. F. DeSandre, P. C. Archibald, C. M. Rotert, and J. L. Stanford, *Anomalous Resonance Effects in Multilayer-Overcoated Diffraction Gratings and Guided-Wave Mode Computational Techniques* (Naval Weapons Center Technical Publication 6913, 1988).

66. R. Petit, ed., *Electromagnetic Theory of Gratings* (Springer-Verlag, New York, 1980), p. 219.
67. I. Pockrand and H. Raether, *Opt. Commun.* **17**, 353 (1976).
68. C. M. Rotert, L. F. DeSandre, J. L. Stanford, and P. C. Archibald, *Diffraction Resonance Measurements at 2.8 and 0.5 Micrometers on Multilayer-Overcoated Diffraction Gratings* (Naval Weapons Center Technical Publication 6751, 1986).
69. V. N. Malysh, O. I. Ovcharenko, and A. N. Osovitskii, *Opt. Spektrosk. (USSR)* **58**, No. 4, 838-843 (1985).
70. E. G. Loewen, M. Neviere, and D. Maystre, "Grating Efficiency Theory As It Applies to Blazed and Holographic Gratings," *Appl. Opt.* **16**, No. 10, 2711-2721 (1977).
71. D. Marcuse, *Theory of Dielectric Optical Waveguides* (Academic Press, New York, 1974).
72. A. Knoesen, M. G. Mohanan, and T. K. Gaylord, "Electromagnetic Propagation at Interfaces and in Waveguides in Uniaxial Crystals," *Appl. Phys.* **B38**, 171-178 (1985).
73. J. Chilwell and I. Hodgkinson, "Thin-Film Field-Transfer Matrix Theory of Planar Multilayer Waveguides and Reflection From Prism-Loaded Waveguides," *J. Opt. Soc. Am. A* **1**, No. 7, 742-753 (1984).
74. H. A. Macleod, *Thin Film Optical Filters* (American Elsevier Publishing Co., Inc., New York, 1969), pp. 17-19.
75. S. A. Shakir and A. F. Turner, "Method of Poles for Multilayer Thin-Film Waveguides," *Appl. Phys.* **A29**, 151-155 (1982).
76. E. Wolf, *Coherence and Quantum Optics*, L. Mandel and E. Wolf, eds. (Plenum, New York, 1973), pp. 339-357.
77. M. Born and E. Wolf, *Principles of Optics* (Pergamon Press, Oxford, England, 1980), p. 376.
78. A. Banos, *Dipole Radiation in the Presence of a Conducting Half-Space* (Pergamon Press, Oxford, England, 1966), p. 15.
79. *Ibid.*, p. 19.
80. M. Born and E. Wolf, *Principles of Optics* (Pergamon Press, Oxford, England, 1980), p. 1.
81. J. C. Light and R. B. Walker, "An R-Matrix Approach to the Solution of Coupled Equations for Atom-Molecule Reactive Scattering," *J. Chem. Phys.* **65**, 4272 (1976).



82. E. B. Stechel, R. B. Walker, and J. C. Light, "R-Matrix Solution of Coupled Equations for Inelastic Scattering," *J. Chem. Phys.* **69**, 3518 (1976).
83. C. Schwartz, L. F. DeSandre, and J. M. Elson, "New Computational Technique for Multilayer Stacks," *Appl. Opt.* **26**, No. 15, 3140 (1987).
84. J. Chandezon, M. T. Dupuis, and G. Gornet, "Multicoated Gratings: A Differential Formalism Applicable in the Entire Optical Region," *J. Opt. Soc. Am.* **72**, No. 7, 839 (1982).
85. J. Charlton, Air Force Weapons Laboratory, Albuquerque, NM, private communication.
86. M. C. Hutley, "An Experimental Study of the Anomalies of Sinusoidal Diffraction Gratings," *Opt. Acta* **20**, No. 8, 607-624 (1973).
87. N. F. Hartman and T. K. Gaylord, "Antireflection Gold Surface-Relief Gratings: Experimental Characteristics," *Appl. Opt.* **27**, No. 17 (1 September 1988).
88. M. G. Mohanan and T. K. Gaylord, "Rigorous Coupled-Wave Analysis of Metallic Surface-Relief Gratings," *J. Opt. Soc. Am. A* **3**, No. 11, 1780-1787 (November 1986).
89. M. G. Weber, "Highly Accurate Renormalized Mode-Coupling Theory for the Reflectivity of a Diffraction Grating," *Phys. Rev. B* **22**, No. 2, 909-913 (15 January 1986).
90. W. B. Veldkamp and Gary J. Swanson, "Developments in Fabrication of Binary Optical Elements," *SPIE* **437**, 54-59 (1983).
91. M. G. Mohanan and T. K. Gaylord, "Diffraction Analysis of Dielectric Surface-Relief Gratings," *J. Opt. Soc. Am.* **72**, No. 10, 1385-1392 (October 1982).
92. This method was suggested by Prof. J. Burke and Dr. Lee Fong, Optical Science Center, University of Arizona, Tucson, Ariz.
93. Dr. Lee Fong, Optical Sciences Center, University of Arizona, Tucson, AZ, private communication.
94. M. Abramowitz and I. A. Stegun, eds., *Handbook of Mathematical Functions*, Nat. Bur. of Stand., Appl. Math. Series 55, 1964.
95. F. Scheid, *Numerical Analysis, Schaum's Outline Series in Mathematics* (McGraw-Hill, New York, 1968), p. 342.